MICROSTRUCTURE SENSITIVE MULTISCALE MODELING OF FRACTURE IN POLYCRYSTALLINE METALS

A Dissertation
Presented to
The Academic Faculty

by

Ushasi Roy

In Partial Fulfillment
of the Requirements for the Degree
Doctor of Philosophy in the
School of Mechanical Engineering

Georgia Institute of Technology
May, 2020

MICROSTRUCTURE SENSITIVE MULTISCALE MODELING OF FRACTURE IN POLYCRYSTALLINE METALS

Approved by:

Dr. Min Zhou, Advisor
G.W.W. School of Mechanical Engineering
Georgia Institute of Technology

Dr. Ting Zhu
G.W.W. School of Mechanical Engineering
Georgia Institute of Technology

Dr. David L. McDowell
G.W.W. School of Mechanical Engineering
Georgia Institute of Technology

Dr. Antonia Antoniou
G.W.W. School of Mechanical Engineering
Georgia Institute of Technology

Dr. Yavari Arash
School of Civil Engineering
Georgia Institute of Technology

Date Approved: December 13, 2019

If you shut the door to all errors, truth will be shut out.

Rabindranath Tagore

To Dadu (my grandfather)

ACKNOWLEDGEMENTS

First, I would like to express sincere gratitude to my advisor Dr. Min Zhou for his continuous support of my Ph.D study and research. His patience, motivation, enthusiasm, and astuteness have greatly influenced me. I would also like to thank my thesis committee members, Dr. David McDowell, Dr. Yavari Arash, Dr. Ting Zhu, and Dr. Antonia Antoniou, for their encouragement and support. I feel especially privileged to be able to collaborate with Dr. David McDowell during the last couple of months of my PhD. Even in this short period of time he helped me grow by providing me with his insightful comments on my work.

I would like to take this opportunity to sincerely express my gratitude to my wonderful colleagues and friends. Dr. Christopher Miller, Amirezza Keyhani and I have shared the office space for the longest time. They have always stood beside me and helped me overcome all the stumbling blocks. Also, I would like to thank my other fellow colleagues Yaochi Wei, Daniel Olsen, Ju Hwan Shin, and Chris Coffelt for always being there. Among my past lab members, Seokpum Kim needs a special mention. I was very lucky to have him inducting me into this group. He is the most generous and supportive senior one could ever ask for. Also, I am grateful to Krzysztof Stopka and Theodore Zirkle for their invaluable contributions while I started to work on the crystal plasticity model. I would also like to thank Dr. Wayne Whiteman and Glenda Johnson for their unconditional support. I cannot thank Robert Manchurian enough for sharing his stories with us every single day. He has been a constant source of inspiration for the past one year.

I consider myself extremely fortunate to be always surrounded by wonderful friends. I would take this opportunity to thank my best of friends Trisha, Bahar, Somrita, Akshay, Simple, Kyungjin, Jihyeon for always standing up for me. I cannot thank Opu, Renu, Nujhat, Lubaba, Pinki, Monjur, Deb, Rekha, Sazib, Auroni, Sahadat, Munna, Irfan, Nael, Anupam enough who made me feel at home nine thousand miles away from home. They have made my stay in Atlanta all so happy and joyful.

Last but not the least, I am immensely grateful to my parents for their unconditional love and support. I can never fully emphasize the role played by them in bringing me up to whatever I am today. Not only my parents but also my grandparents have always been an immense source of inspiration for me. Also, I have the most wonderful parents in law who have blessed me with their love and support throughout. I cannot possibly express in words how fortunate I am to have my best friend Rahul as my husband. At the end of every mundane day, I lived for a single phone call to share our stories, to discover the little cracks that let the Sun in like a door ajar and find the strength and courage to live another day. His constant, unaltered love and support through thick and thin, through days of vulnerabilities, and moments of happiness keep me going.

TABLE OF CONTENTS

LIST OF TABLES

LIST OF FIGURES

Page

LIST OF SYMBOLS

(Φ_1, Φ, Φ_2)	Euler angle set
g_i	orientation matrix for the i^{th} grain
Δg	misorientation matrix
θ	grain boundary misorientation angle
ρ_{gb}	grain boundary density
L_{gb}	grain boundary length
A_m	area of the microstructure region
ρ_{gb}^{W}	density of the weaker grain boundaries
G	mean intercept grain size
$\langle G \rangle$	average mean intercept grain size
$G_{\max}$	maximum mean intercept grain size
u_y	imposed displacement in Y direction of the specimen
$\boldsymbol{\sigma}$	Cauchy stress tensor
$\boldsymbol{\varepsilon}$	strain tensor
$\mathbf{C}$	stiffness matrix in Voigt notation
σ_h	hydrostatic component of stress
$\mathbf{S}$	deviatoric stress
$\bar{\sigma}$	Mises stress
$\bar{\varepsilon}^p$	effective plastic strain

$\mathbf{I}$	identity matrix
σ_y	uniaxial yield stress
k	isotropic hardening parameter for bilinear elastic-plastic law
$\overline{E}$	effective elastic modulus for the homogenized material
$\overline{v}$	effective Poisson's ratio for the homogenized material
$\overline{G}$	effective shear modulus for the homogenized material
$\overline{B}$	effective bulk modulus for the homogenized material
$\mathbf{t}$	traction on a 2D cohesive interface
$\mathbf{n}, \mathbf{s}$	unit vectors along the normal and tangential directions of 2D cohesive interface
$\boldsymbol{\delta}$	separation in the cohesive interface
$\mathbf{K}$	stiffness matrix for the cohesive interfaces
δ_{nc}, δ_{sc}	critical separation in normal and tangential directions
$T_{\max}$	maximum traction at the interface at which damage sets in
Φ_0	cohesive energy of grains
D	damage parameter
δ_m	resultant separation of the interfaces
δ_m^c	critical resultant separation for fracture
τ	normalized cohesive strength of an interface
λ	normalized cohesive separation
λ_0	inverse of the initial slope in bilinear traction-separation law.
T_{GB}	cohesive strength of the grain boundaries
T_G	cohesive strength of the grains

$T_{GB}^{\min}$	minimum grain boundary cohesive strength
Q	ratio of maximum to minimum grain boundary cohesive strength
d_z	cohesive element size
$\mathbf{F}$	deformation gradient
$\mathbf{F^e}, \mathbf{F^p}$	elastic and plastic part of the deformation gradient
s_0^α, n_0^α	slip direction and slip plane normal for the α^{th} slip system
τ^α	resolved shear stress in the α^{th} slip system
$\dot{\gamma}^\alpha$	slip system shearing rate for the α^{th} slip system
$\mathbf{L^p}$	plastic velocity gradient
χ^α	back stress for the α^{th} slip system
g^α	drag stress for the α^{th} slip system
$k, q^{\alpha\beta}$	coefficients for isotropic hardening and latent hardening
A_{kin}, A_{dyn}	coefficients for kinematic hardening and dynamic recovery
K_{IC}	plane strain fracture toughness
J_{IC}	steady state fracture resistance
γ	interfacial strength ratio
Δa	crack extension
a	projected crack length
W	width of the CT specimen
r_p	plastic zone size at the crack tip
J	J-integral or the fracture resistance measure in EPFM

w	strain energy
Γ	crack tip contour for J-integral calculation
J_i	initiation fracture resistance
K_i	initiation fracture toughness
δ_{crack}	crack opening displacement
J_S	surface energy release rate
J_P	plastic dissipation
H_g, H_{gb}	proportions of transgranular and intergranular cracking
H	fracture mechanism descriptor
L_g, L_{gb}	true crack length through grains and grain boundaries
ξ	crack path tortuosity
P	probability
K_0	fracture toughness value with 63% probability of occurrence
m_f	shape factor for the Weibull distribution of fracture toughness
$\overline{\xi}$	mean crack path tortuosity
$\overline{\Phi}_{gb}$	mean grain boundary energy
$\overline{J}_S^g$	mean surface energy of grains
$\overline{J}_S^{gb}$	mean surface energy of grain boundaries
J_P^g	plastic dissipation of grains
$\overline{J}_{IC}$	mean value of the overall fracture resistance
$\overline{J}_S$	mean value of the surface energy release rate

$\bar{J}_P$	mean value of plastic dissipation
f_g^{PSS}	fraction of grains with favorably oriented primary slip systems
M	microstructure descriptor
M_0	fitting microstructure parameter in mm
$\mathbf{T}$	traction in the 3D traction separation law

SUMMARY

Systematic exploration of the correlation between macroscale properties and microstructure attributes provides decision support to design new material microstructures with tailored properties. Currently no systematic approach exists that correlate overall fracture behavior of ductile polycrystalline materials with their microstructure attributes such as grain size, grain orientation distribution functions, grain boundary misorientation distribution etc. With an aim of establishing correlation between fracture toughness and microstructure attributes of ductile polycrystalline metals, a cohesive finite element method (CFEM) based multiscale computational framework is developed. The framework uses fully resolved 2D and 2.5D microstructures and explicitly models crack propagation through the grains and along the grain boundaries. A misorientation angle dependent interfacial relation is assumed for the grain boundaries to incorporate the effects of grain boundary charcteristics. A crystal plasticity formulation is adopted for the grains to account for their anisotropic deformation. Fracture resistance is measured in terms of J_{IC}, K_{IC}, and crack growth resistance curves. The framework also captures the competitions between (a) intergranular and transgranular mechanisms of fracture, and (b) plastic deformation and crack growth.

The computational framework is then applied to bcc Mo, and the model parameters are calibrated to match the fracture behavior of Mo. The first part of the work focuses on the effects of grain boundary behavior on fracture. The results indicate that the overall fracture resistance decreases as the density of weaker grain boundaries increases and the

skewness in misorientation angle dependent profile of grain boundary strength increases. Intergranular fracture tends to lower the fracture resistance and transgranular fracture acts as an effective toughening mechanism due to the associated plastic dissipation. Fracture toughness increases with increasing mean intercept grain size since coarser grains provide longer mean free path for transgranular fracture.

The second part of the work focuses on the effects of crystallographic texture on fracture. Two of the prime bcc texture components are considered in this study. As the fraction of textured grains increases, the overall fracture toughness increases. Fracture resistance tends to increase with increasing skewness in the grain size distribution, decreasing density of weaker grain boundaries, and increasing density of favorably oriented primary slip systems. The use of multiple statistically equivalent instantiations of microstructure facilitates characterising the stochasticity in fracture toughness evaluation. Further analyses of results led to development of mathematical relations to correlate the fracture toughness with microstructure attributes.

Finally the 2D model is extended to a 2.5D model to understand the effficacy of the assumptions made for the 2D model. Even though the basic trends revealed by the 2D model remain unaffected, the 2.5D model introduced plastic dissipation in intergranular fracture. This led to the conclusion that the transgranular and intergranular proportions of crack propagation is to be optimized for maximum fracture resistance. The overall methodology established in this work has the potential to be used in materials design exercises for developing novel microstructures with tailored properties.

1 INTRODUCTION

1.1 Background and Motivation

The history of mankind is full of tragic incidents that find their roots in material fracture. A shipwreck was commonplace during the world war II. Chains of incidents with the navy brought the engineers' attention to the phenomenon of material fracture. As a result, Griffith [1] and Weighardt's [2] findings on material fracture gained huge impetus and the field of fracture mechanics came into existence with further developments by E. Orowan [3], and G. R. Irwin [4, 5] based on Westergaard [6] and Kies [7, 8] prior efforts. The next few decades saw myriads of new concepts and ways to characterize materials' fracture behavior. G. R. Irwin and the contemporaries laid the basic foundational blocks for linear elastic fracture mechanics (LEFM). LEFM handled brittle fracture satisfactorily. However, further development of elastic plastic fracture mechanics was due to explain and characterize ductile fracture toughness. Based on earlier works of Irwin [9], Dugdale [10] and Barenblatt [11] introduced cohesive zone model to analyze the fracture process zone at the crack tip in ductile materials. Wells [12] further introduced the concept of crack opening displacement as a measure of fracture toughness. Rice, Hutchinson and his colleagues [13-17] developed the concept of path independent *J*-integral that can be used both as an energy release rate and stress intensity parameters under some caveats. However, the catastrophes did not cease to happen. There are series of ship wreckages, failure of aircrafts that continue to happen, even in 2018. Therefore, despite the several developments in the field of fracture mechanics, multitudes of questions still remain to be answered, and hence, the importance of the field never abated. The interest now is particularly in the

multiscale nature of the phenomenon. The fracture toughness measured in terms of K_{IC}, J_{IC}, CTOD etc., manifests the material behavior in the macroscale and does not reflect the microstructural evolutions during the process. Several evidences exist that show that microstructure influences the fracture toughness, however, works to directly correlate the two are still inadequate. Knowledge of the correlation between the microstructural attributes and the macroscale fracture behavior is the key to design novel materials or novel microstructures for customized behavior. In this chapter, the existing computational and experimental works that investigate the effect of microstructure on fracture are reviewed and discussed.

1.2 Review of microstructure sensitive computational modeling of fracture

Systematic exploration of the correlation between macroscale properties and microstructural attributes is the key to design new materials with microstructures for tailored properties. Extensive studies have been carried out on ways to enhance material behavior through microstructure design [18-21] in the last few decades. To understand the role of microstructural attributes like the grain orientation and grain boundary characteristics on fracture, microstructure-sensitive modeling of fracture processes began with the advent of computational micromechanics in mid-1980s. The fracture toughness of brittle materials such as ceramics and composites have been quantitatively correlated with microstructure by accounting micromechanisms of crack propagation [22-27]. For polycrystalline ductile materials, less has been done towards explicitly tracking crack paths and quantitatively capturing their influence on the overall fracture toughness [26, 28-31].

After Asaro and colleagues [32-36] developed early finite element models to analyze deformation in ductile polycrystals, Needleman and colleagues [37-40] adopted finite element method to study ductile fracture by void nucleation and growth at the grain boundaries. They further extended these approach to model interfacial failures using cohesive zone methods and cohesive finite element methods [39, 41-43]. In Liu et al., Srivastava et al., Tvergaard and Needleman [29, 44-46], ductile fracture is modeled via void nucleation and growth associated with inclusions or second phase particles using modified Gurson's models [47, 48]. The polycrystalline grain structure is not explicitly modeled. Polycrystalline grain structures are considered by Guo et al. [49], and Osovski et al. [50], in analyses of intergranular crack propagation in β-Ti alloys. The results show that the intergranular crack propagation acts as a toughening mechanism and the ductile crack growth resistance is dependent on crack paths in a manner similar to brittle crack growth resistance. Osovski et al. [31] analyzed the potential of crack path engineering in polycrystalline ductile materials. Molkeri et al. [51] analyzed the intergranular crack growth resistance as a function of the grain size. Musienko et al. [52] analyzed intergranular fracture in the context of corrosion.

Based on the earlier works of Asaro, Needleman and colleagues, Zikry et al. [53-56] investigated the effects of grain orientation distribution and grain boundary characteristics on micromechanisms of fracture using large scale computational crystal plasticity finite element methods. Sreeramulu et al. [57] analyzed the effect of texture on stationary crack tip fields using crystal plasticity finite element modeling. Kowalski et al. [58] predicted the strain field before and after intergranular cracking in a 3D periodic polycrystalline

aggregate. They considered textured grains and cohesive interfaces along the grain boundaries (GB). However, the model neither attempted to measure the fracture toughness nor delineated the effect of texture systematically. In a recent work by Wilson et al. [59], a microstructure-sensitive driving force for crack growth was evaluated using discrete dislocation plasticity, crystal plasticity and extended finite element method. Even though the model assumed textured polycrystalline microstructure, no direct correlation between texture and fracture was established. Simonovski and Cizelj [60] showed that intergranular cracking in stainless steel wires is heavily influenced by texture of polycrystalline aggregates. However, the influence on fracture toughness or fracture micromechanisms was not quantified. Clayton and Knap [61] employed phase field theory and finite element modeling to simulate the competition between fracture and twinning in both single and polycrystals. Again, the effect of texture has not been characterized systematically. Chen et al. [27] analyzed the effects of grain orientation and grain boundary misorientation on fracture of polycrystals using a non-local lattice particle model. However, they analyzed the microstructural effects only on crack propagation paths. No comments were made on the macro scale fracture toughness values. In a recent work, Bond and Zikry [62] analyzed qualitatively the effects of grain orientation and grain boundary misorientation on competition between transgranular and intergranular crack propagation. They provide important insights in terms of dislocation pile ups and directional slip rate that leads to crack propagation inside the grains or along the GBs. To correlate fracture toughness with microstructural attributes, Li and Zhou [22, 23, 30] developed a cohesive finite element based multiscale model. They extented the model to a 3D polycrystalline microstructure and adopted crystal plasticity formulation to analyze fracture micromechanisms [28].

However, The model assumes uniform GB properties and does not account for the effects of the misorientation angle.

1.3 Review of the experimental studies on influence of microstructural attributes on fracture

Besides the computational efforts, some experimental studies exist [63-69] that attempted to establish the correlation between fracture toughness and grain orientation or GB misorientation using bicrystals with preferred orientations and GB with pre-determined misorientation. Watanabe and colleagues [65, 66, 69] worked extensively on GB engineering and delineated the variation of GB fracture strength as a funcion of the GB characteristics in different materials. Kokawa et al. [70], and Kobayashi et al. [68] used bicrystals of Al to study the effect of grain boundary character distribution (GBCD) on creep behavior. Watanbe and colleagues [63, 64] also worked on Zn bicrystals and polycrystals to delineate the effects of GBCD on fatigue and creep. Watanabe and colleagues worked extensively on Mo and reported fracture stress as a function of the GB misorientation angle [65, 66, 69]. In particular, they reported that the GB fracture strength in pure Mo varies nearly sinusoidally with the GB misorientation angle as shown in Figure 1.1. Bantounas et al. [71, 72] reported cracking in Ti-6Al-4V system as a function of the GB misorientation angle. All these experiments show that the GBs with higher misorientation angle in the renge of 15-65 are fracture prone sites. Arafin and Szpunar [73] analyzed the susceptibility for intergranular cracking in Mo as a function of GB misorientation angle. Bachurin [74] qualitatively correlated crack paths in polycrystalline Pd with the GB misorientation. Bond and Zikry [62] established their model based on the

experimental observations reported by Watanabe and colleagues as did Roy and Zhou 2020. However, none of these above mentioned works systmatically characterized the effect of grain orientation on overall fracture toughness in terms of K_{IC} or J_{IC}.

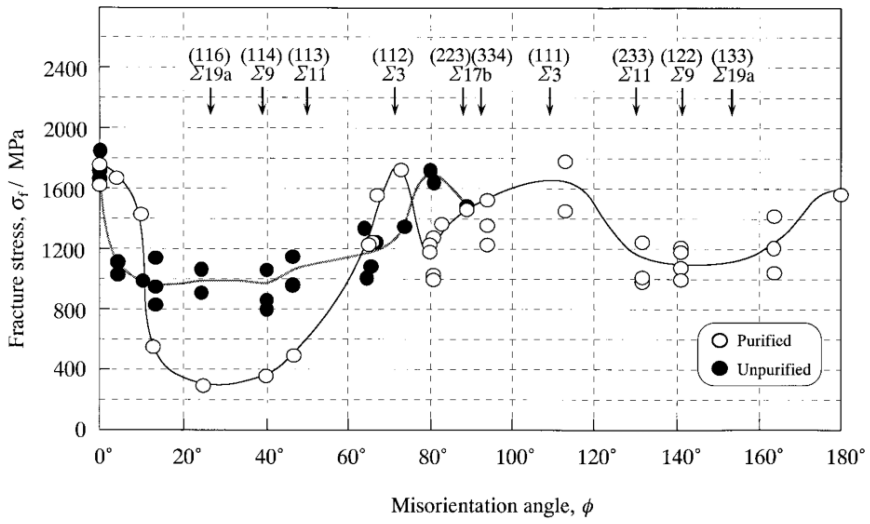

Figure 1.1: Fracture stress as a function of the GB misorientation angle. Reproduced from Watanabe and Tsurekawa [67].

1.4 Scope and Organization of This Thesis

Despite several efforts in both computational and experimental works to relate macroscale fracture behaviour with microstructure attributes in polycrystalline ductile materials, complete understanding of the trends has not been adequately achieved. Currently, no systematic approach exists to explicitly quantify the combined effects of different microstructure attributes on the fracture measures for ductile fracture of polycrystalline materials. Therefore, we aim at developing 2D and 3D computational

frameworks that can systematically establish the trends between fracture measures and microstructure attributes. In order to achieve this, our major objectives are to

1) develop a 2D cohesive finite element based concurrent multiscale model to simulate fracture in polycrystalline ductile materials;
2) develop ways to measure the macroscale fracture toughness in terms of J_{IC}, K_{IC} and validate the model with realistic values;
3) explore the effects of microstructural attributes on magnitudes of fracture toughness and fracture micromechanisms with a focus on the effects of grain boundary characteristics;
4) analyze the stochasticity in fracture and establish mathematical correlation between the fracture toughness, fracture micromechanisms and the microstructure attributes;
5) enhance the capability of the model to take into account the anisotropic deformation of grains and explore the effects of crystallographic orientation on fracture;
6) extend the 2D computational framework into 3D and compare among 2D, 2.5D, and 3D modeling of microstructure-sensitive fracture.

Chapter 2 describes the 2D multiscale computational framework that explicitly tracks the crack path through the polycrystalline microstructure and incorporates the effects of GB characteristics. Chapter 3 discusses the material and microstructure used for the computational framework. Chapter 4 describes the methods to characterize the fracture toughness, fracture micromechanisms and finally validates the model using experimental

observations reported in the literature. It also shows that the model is able to capture (a) the competition between intergranular and transgranular fracture mechanism, and (b) the competition between crack growth and plastic deformation. Chapter 5 explores the effects of microstructure attributes such as the grain size, grain boundary characteristics on fracture toughness and fracture micromechanisms. It also analyzes the stochasticity in fracture and establishes a mathematical correlation between fracture toughness and microstructural attributes with a focus on the grain boundary behavior. Chapter 6 extends the capability of the model to incorporate a crystalline plasticity formulation to simulate the effect of grain anisotropy. This work further analyzes the effects of crystallographic texture and finally establishes a mathematical correlation between macroscale fracture measures and microstructure attributes. In Chapter 7, the 2D model is extended to a 2.5D formulation. Comparisons are made among 2D, and 2.5D modeling of fracture in terms of efficacy of the different frameworks in capturing simultaneously the microstructure effects and the competitions between different fracture mechanisms and plasticity explicitly. Chapter 8 summarizes the contributions and conclusions of this work and outlines the future scope of work in this direction.

2 MATERIAL AND MICROSTRUCTURE

2.1 Introduction

In this chapter, a material is chosen for the entire study and microstructures are generated and characterized. In order to understand the effects of microstructure attributes on fracture behavior in terms of both fracture toughness and fracture micromechanisms, microstructures are generated by systematically varying the grain orientations, grain boundary misorientations, grain size distribution etc. The polycrystalline microstructures were generated using the Voronoi tessellation function, and the orientations were phenomenologically assigned to the grains. The use of computational methods to generate microstructure enables generating statistically equivalent microstructure sample sets (SEMSS). Computations on SEMSS further facilitates characterization of stochasticity in fracture toughness.

Section 2.2 provides the details related to generating microstructures with random orientations and characterization of grain boundaries in terms of the misorientation angle. Section 2.3 provides the details of the microstructures with preferred orientations or crystallographic textures.

2.2 Polycrystalline microstructures with random grain orientations

In order to account for the effects of grain orientations and the GB characteristics on fracture of ductile materials with grain structures, single phase pure molybdenum (Mo) is

chosen due to the existence of significant relevant experimental data ([63]; [64]; [65, 66, 69]). Specifically, the data for unalloyed Mo [69] show that GB fracture strength exhibits a near sinusoidal variation with the grain boundary misorientation angle. GBs with misorientation angles below 15˚ or above 75˚ are nearly as strong as the grains, but GBs with misorientation angles in the range of 15˚ - 75˚ can have strengths as low as half of that of the grains. These low fracture strength GBs are the likely sites for crack initiation and propagation.

The polycrystalline microstructures are generated using the Voronoi tessellation function. Four levels of grain size (measured in terms of the mean grain intercept length) are considered. To quantify the stochasticity in fracture behavior due to variations in microstructure morphology, twenty statistically similar instantiations of microstructure for each grain size are used. Figure 2 shows four representative instantiations from each of the four statistically equivalent microstructure sample sets (SEMSS). In all cases, the grains are randomly orientated. A set of Euler angles (Φ_1, Φ, Φ_2) is used to specify the orientation of each grain with respect to the specimen axes. The grain orientations in Figure 2.1 are denoted by the plane of the grains that is parallel to the specimen plane (X-Y) using the scheme of plane colors in the stereographic projections of the crystallographic plane normals on an inverse pole figure map [75]. Due to the cubic crystalline symmetry, the stereographic triangle contains all possible grain orientation relations, as shown in the figure. Although the color map does not uniquely define the orientation of the grains, it indicates that no particular orientation is preferred in the microstructure, i.e. the grains are indeed randomly oriented. The mean intercept grain size for each of the SEMSS are shown

in Figure 2.2(a). The error bars account for statistical variations among the twenty instantiations in each set.

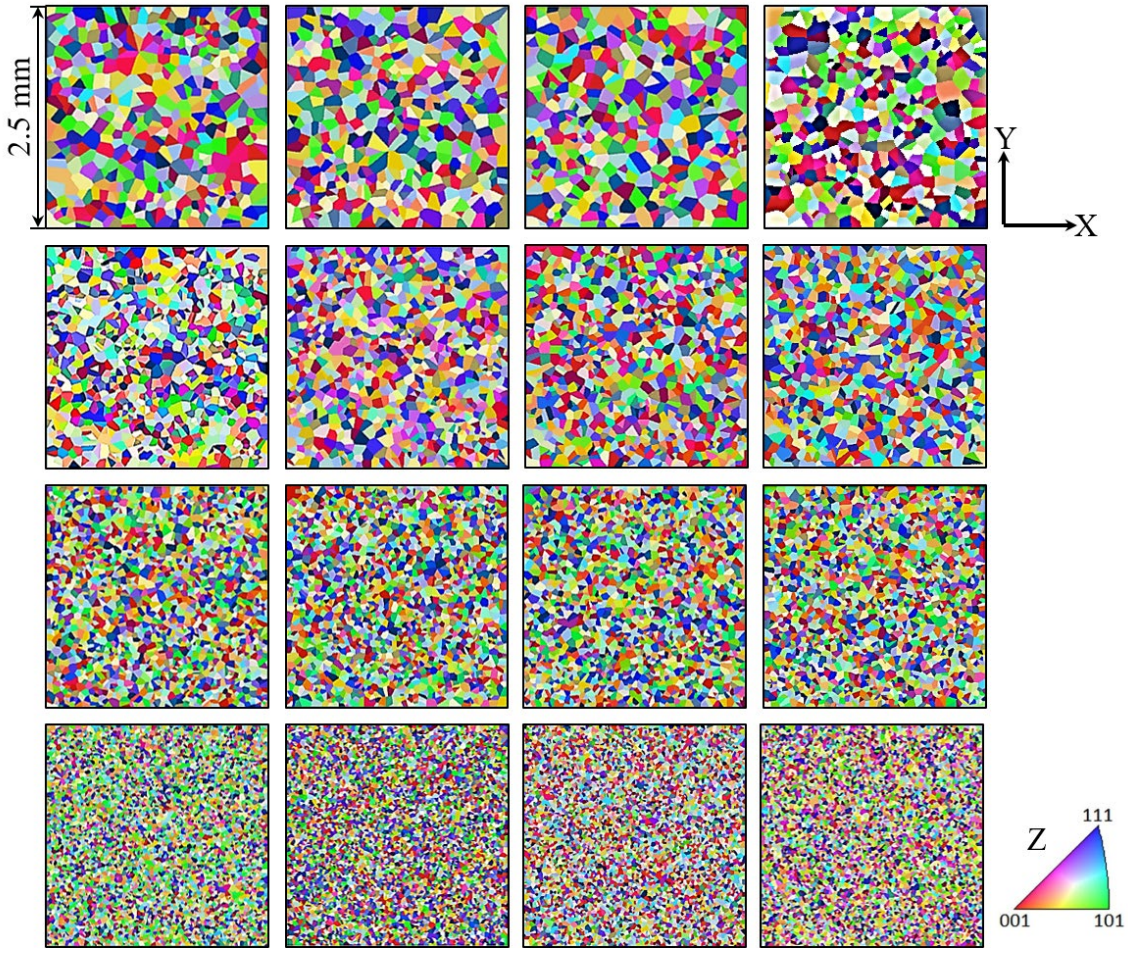

Figure 2.1: Four out of twenty instantiations of microstructure from each of the four statistically equivalent microstructure sample sets (SEMSS). The colors in the stereographic triangle indicate the crystalline plane normals of grains parallel to the Z axis of the specimen

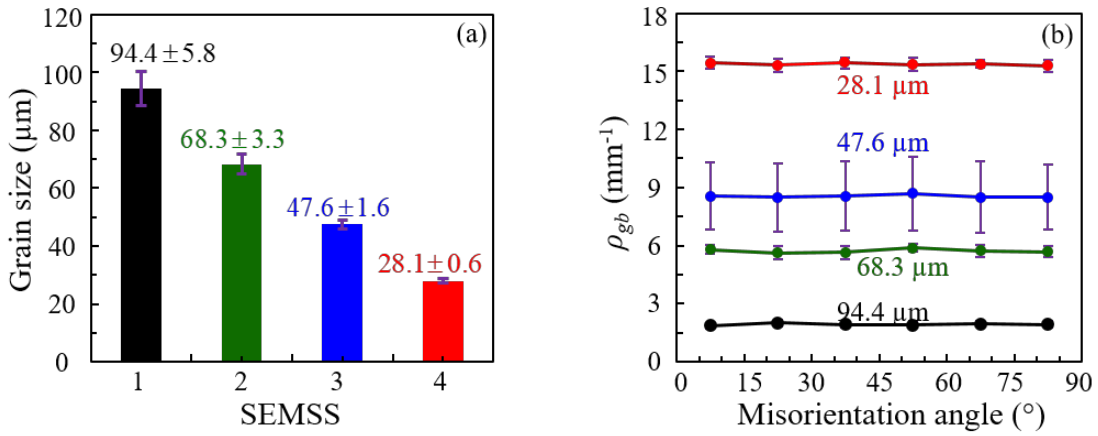

Figure 2.2: (a) mean intercept grain sizes and (b) grain boundary density as functions of misorientation angle for all four sets of statistically equivalent microstructure sample sets (SEMSS).

Due to the random orientations of the grains, GBs are associated with a range of misorientation angles. Since fracture strength is a function of the GB misorientation angle [69], the GB misorientation angle is calculated. This angle is the angle by which one grain is to be rotated about an axis common to the contacting grain pair in order to bring the grains into coincidence. The Euler angle sets are used to calculate the orientation matrix (g) for all grains. This matrix is

$$g = \begin{bmatrix} \cos\Phi_1 \cos\Phi_2 - \sin\Phi_1 \sin\Phi_2 \cos\Phi & \sin\Phi_1 \cos\Phi_2 + \cos\Phi_1 \sin\Phi_2 \cos\Phi & \sin\Phi_2 \sin\Phi \\ -\cos\Phi_1 \sin\Phi_2 - \sin\Phi_1 \cos\Phi_2 \cos\Phi & -\sin\Phi_1 \sin\Phi_2 + \cos\Phi_1 \cos\Phi_2 \cos\Phi & \cos\Phi_2 \sin\Phi \\ \sin\Phi_1 \sin\Phi & -\cos\Phi_1 \sin\Phi & \cos\Phi \end{bmatrix}. \quad (2.1)$$

It facilitates calculation of the misorientation matrix (Δg) at the GBs using

$$\Delta g = g_1^{-1} g_2, \tag{2.2}$$

where g_1 and g_2 are the orientation matrices of two neighboring grains. The misorientation angle (θ) is then calculated using the trace of the misorientation matrix via

$$\cos\theta = \frac{1}{2}\left[trace(\Delta g) - 1\right]. \tag{2.3}$$

The axis of misorientation can be calculated using the off-diagonal terms of the misorientation matrices. Since our focus is on resolving the fracture behavior of GBs as a function of their misorientation angles, the misorientation axes are not shown. Figure 2.2(b) shows the density of GBs at different misorientation angles. The GB density (ρ_{gb}) is defined as

$$\rho_{gb} = \frac{L_{gb}}{A_m}, \tag{2.4}$$

where L_{gb} is the total length of GBs at a given misorientation angle, and A_m denotes the area of the microstructure region. The GBs with misorientation angles in the range of 15°-75° are the fracture prone sites in a polycrystalline material and are hence called the weaker GBs with an associated density of ρ_{gb}^{W}. Figure 2.3 compares a computationally generated microstructure with an experimentally obtained microstructure obtained by Sturm *et al.* who reported the mechanical properties of unalloyed Mo having an average grain size of 97 μm [76]. The grain structure of this Mo is very similar to the computationally generated microstructure with an average grain size of 94.36 $\pm$ 5.76 μm.

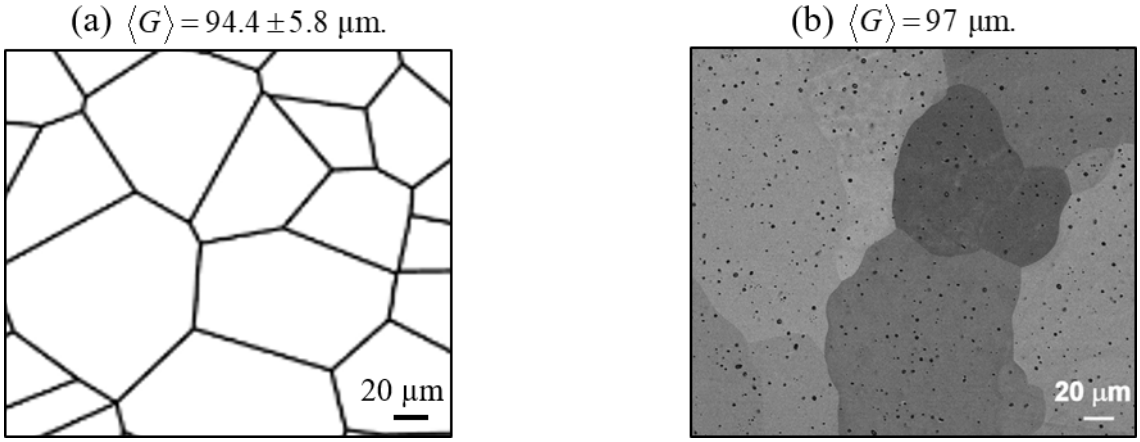

Figure 2.3: (a) computationally generated polycrystalline microstructure, (b) optical micrograph of an unalloyed Mo [76].

2.3 Polycrystalline microstructures with crystallographic texture

Multiple texture components are observed in Mo depending upon different processing routes and deformation modes like hot rolling, cold rolling, shearing etc. Some of these texture components remain in the annealed recrystallized microstructure. The rotated cube component {001}<110> is the most common type [77-82]. To delineate the effect of texture, we design microstructures with controlled proportions of textured grains and randomly oriented grains. First, microstructures are generated with randomly oriented grains with a mean intercept grain size of ~70 μm using the Voronoi tessellation function. A set of Euler angles (Φ_1, Φ, Φ_2) is used to specify the 3D orientation of each grain with respect to the specimen axes. This microstructure is labeled as the one with 0% textured grains (TG). Then, preferred orientation or texture is assigned to 30% of the grains. The

preferred orientations are characterized by two prime texture components, the rotated cube component and the Goss component. The Goss component {011}<100> preferably aligns the primary slip systems with the X-Y plane of the specimen. This facilitates enhanced plasticity in the grains and thus magnifies the competition between plasticity and new surface creation. The fraction of TG is increased to 50%, 70%, and 100% in three other sets of microstructures. The microstructure with 100% TG contains ~25% {001}<110> texture components and remaining ~75% {011}<100> components. The proportion of the two texture components remains the same in all four sets of microstructure with a non-zero fraction of TG. Five statistically equivalent microstructure samples are generated for each case. The microstructure in Figure 2.4(e) exhibits distinct texture components corresponding to {001}<110> and {011}<100> as shown in the corresponding (011) pole figure (Figure 2.5(e)). As the fraction of TG decreases, the intensity of the texture components decreases and the pole figure depicts no preference for a particular orientation type (Figure 2.5(a)). The grains with preferred orientations have the primary slip systems (PSS) favorably aligned for easier activation of slip. Different orientations facilitate favorable alignment of some of the four primary slip systems of Mo. Figure 2.5(f) shows the fraction of the grains with favorably oriented primary slip systems. These slip systems are ranked in terms of their critical resolved shear stress (CRSS). The figure plots these fractions as a function of the CRSS/C_{44}. Lower value of the CRSS/ C_{44} denotes ease in activating slip. As expected, the fraction of grains with favorably oriented PSS increases with increasing fraction of the TG.

Effective mean intercept grain size distributions are shown in Figure 2.6(a) – (e). The effective grain size distribution is nearly symmetric and monomodal in case of the

microstructure with 0% TG. As the fraction of TG increases, the effective grain size distribution changes progressively showing a larger peak at a smaller range of grain size and a small signal at a comparatively higher value of the grain size (Figure 2.6(d)-(e)). The grains with {110}<100> texture behaves almost like a 2nd phase matrix material without a distinct polycrystalline grain structure in Figure 2.6(d)-(e). Figure 2.6(f) shows that the mean intercept grain size $\langle G \rangle$ remains nearly constant with increasing fraction of TG. However, the maximum value of the grain size $G_{\max}$ increases with increasing fraction of TG accounting for the large fraction of grains oriented along {110}<100>.

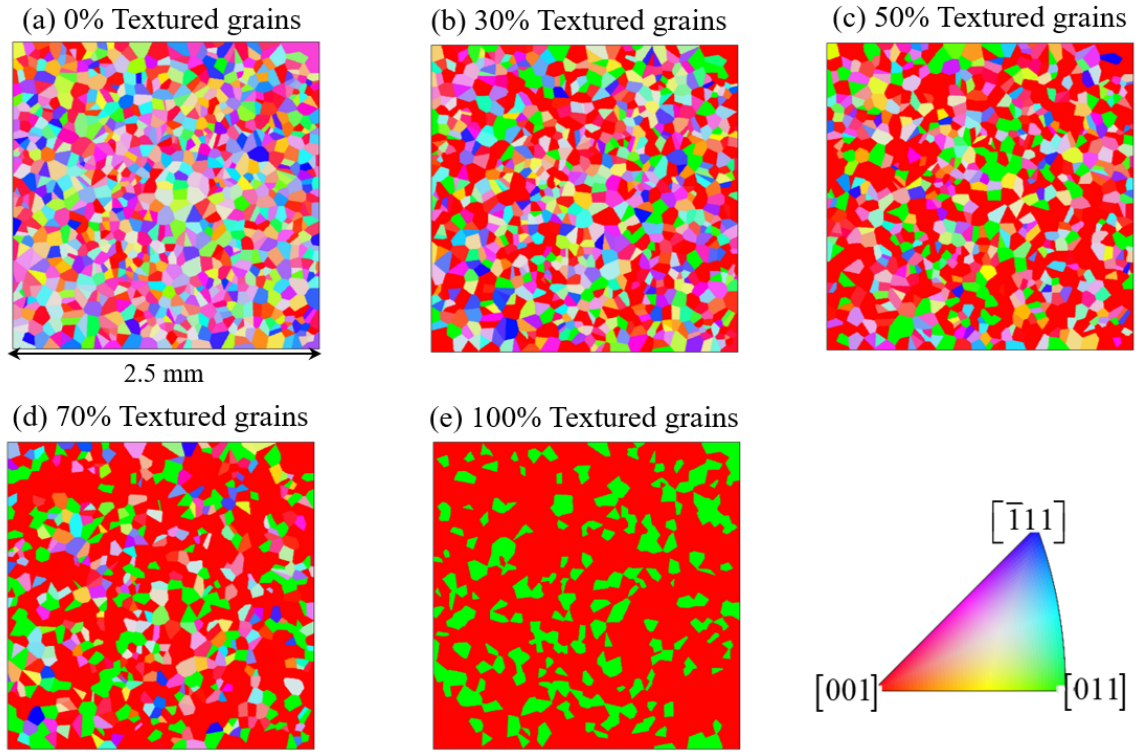

Figure 2.4: One out of five instantiations of microstructure from each of the five statistically equivalent microstructure sample sets (SEMSS). The colors in the stereographic triangle indicate the crystalline plane normals of grains parallel to the Z axis of the specimen.

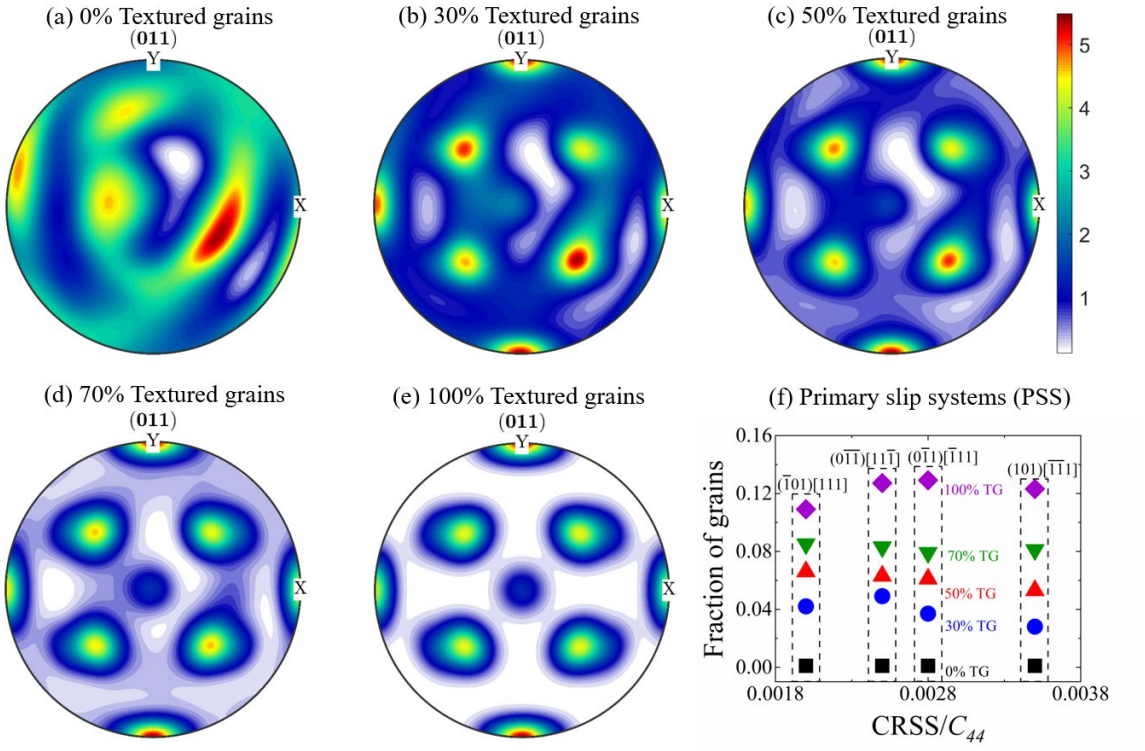

Figure 2.5: (a) – (e) (011) pole figures showing the orientation distribution functions of the five SEMSS. The color represents intensity of a particular orientation measured in arbitrary units. (f) fraction of grains with favorably orientated primary slip systems as a function of the critical resolved shear stress (CRSS) normalized by the C_{44}.

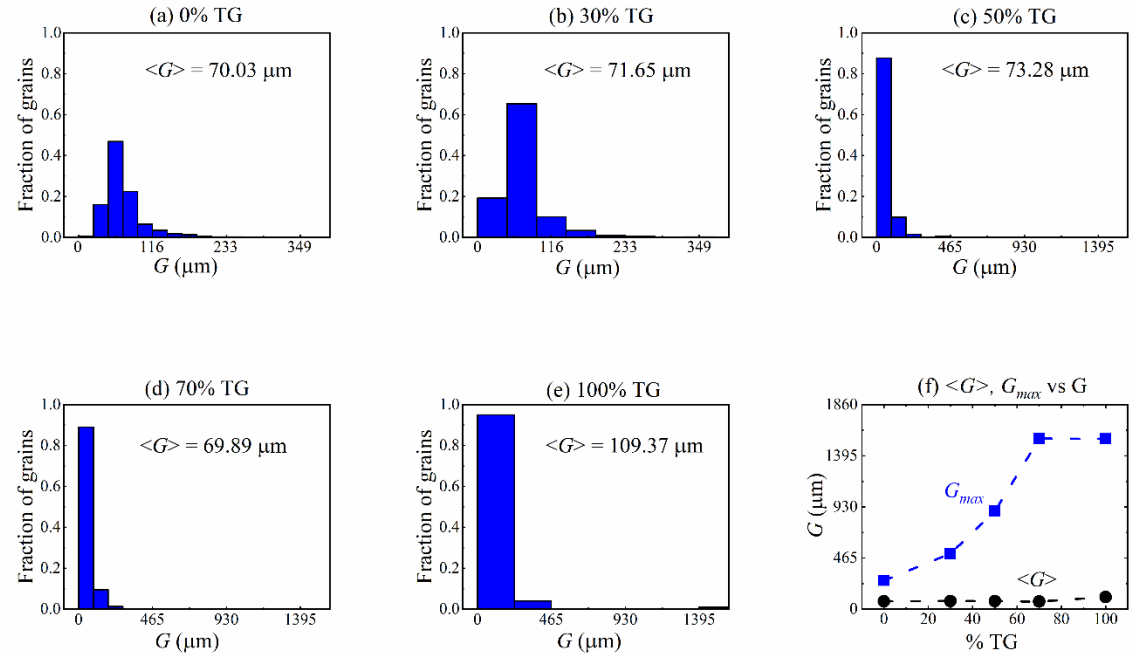

Figure 2.6: (a) – (e) Mean intercept grain size distributions for five SEMSS, and (f) maximum grain size and the mean grain size as function of the fraction of textured grains (TG).

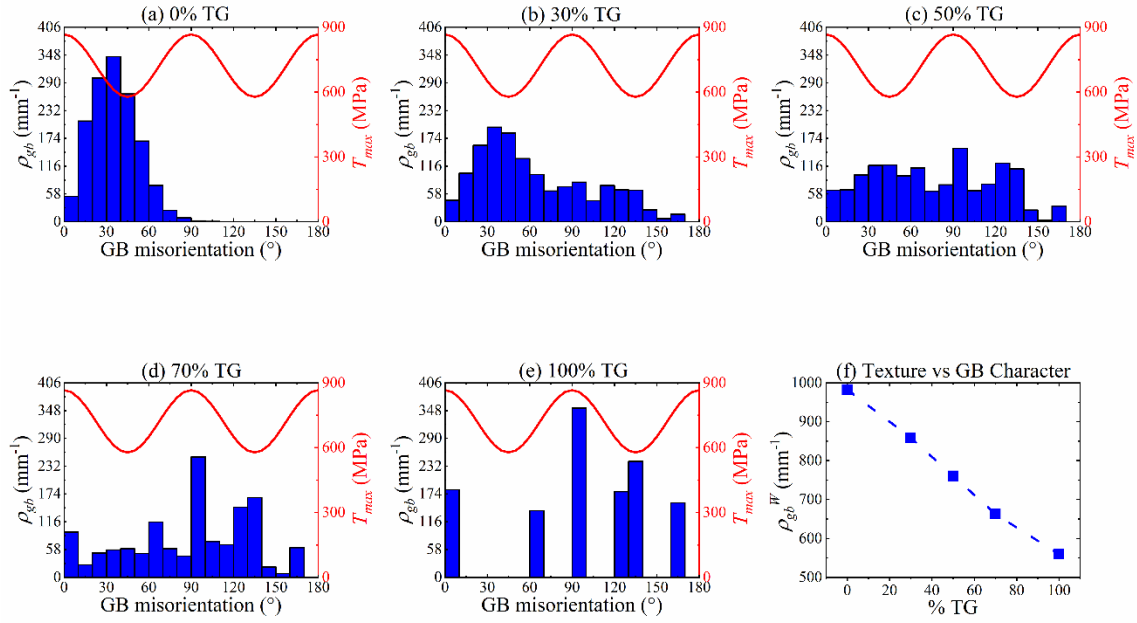

Figure 2.7: (a) – (e) distribution of grain boundary misorientation angles for five SEMSS. (f) weaker GB density as a function of the fraction of textured grains.

2.4 Summary

The Voronoi tessellation function provides a way to efficiently generate multiple statistically equivalent instantiations of polycrystalline microstructure using minimal computational cost. These microstructures resemble the experimentally obtained microstructures reasonably well. The microstructures are characterized in terms of the mean grain intercept length. The grain orientations are characterized using the pole figures. Also, the grain boundary characters are defined in terms of their misorientation angle. The first sets of SEMSS with random grain orientations are used to explore the effects of grain boundary character as discussed in Chapter 5. The second sets of SEMSS with varying fraction of textured grains are used to study the effect of grain orientations as discussed in Chapter 6. These 2D microstructures are also used in the generalized plane strain modeling described in Chapter 7.

3 CFEM-BASED MULTISCALE FRAMEWORK

3.1 Introduction

In this chapter, a Cohesive Finite Element Method (CFEM) based multiscale 2D framework is developed to evaluate material fracture toughness through simulation of fracture processes in polycrystalline microstructures. This framework uses concurrent modeling of crack propagation through grains and grain boundaries and the load-displacement response of the laboratory scale fracture toughness test specimen. Different constitutive relations are assigned to different sections of the model. For microstructures with random orientations, simple bilinear elastic plastic law is used. For the microstructures with texture, a crystalline plasticity model is used to account for the anisotropic deformation of the grains. The homogeneous region always uses the bilinear elastic-plastic response. The constitutive relation for the interfaces takes into account the effects of grain orientation and grain boundary misorientation. This approach uses the *J*-integral to quantify the fracture resistance as a function of microstructural attributes. It also provides a means for calibrating model parameters at the microscale through macroscale responses which can be easily measured in experiments.

Section 3.2 provides the multiscale framework used in this computation. The material models used for different sections of this multiscale 2D framework are discussed in section 3.3.

3.2 Multiscale framework

Since the pioneering work of Xu and Needleman [42], the cohesive finite element method (CFEM) has been extensively used in many applications, including modeling debonding, arbitrary crack propagation through different microstructural constituents, and phase boundaries [22, 23, 83-85]. The primary aim here is to quantitatively relate fracture toughness to microstructural attributes and the competition between different fracture mechanisms. To achieve this, it is necessary to explictly resolve microstructural level fracture processses. Following Li and Zhou [30], we adopt the CFEM to explicitly track transgranular and intergranular crack propagation in fully dense microstructures with grains and grain boundaries. The multiscale CFEM computational configuration is shown in Figure 3.1. A compact tension specimen is used to simulate laboratory-scale fracture toughness tests. The configuration meets all requirements of the ASTM standard [86] for plane strain fracture toughness and *J*-integral measurements. The overall dimensions of the CT specimen are 6.12 mm × 6 mm. The microstructure region is 2.5 mm × 2.5 mm in size and is inserted around the tip of the pre-crack of 2.25 mm in length. The CFEM is implemented in the microstructure region which is stitched to the homogeneous section using a mesh-tie constraint, just as in [22]. The size of the microstructure region is so chosen such that the plastic zone is fully within this region. Overall mode-I loading is effected through an imposed load point displacement, as indicated in Figure 3.1. The edges of the specimen are traction-free and conditions of plane strain prevail.

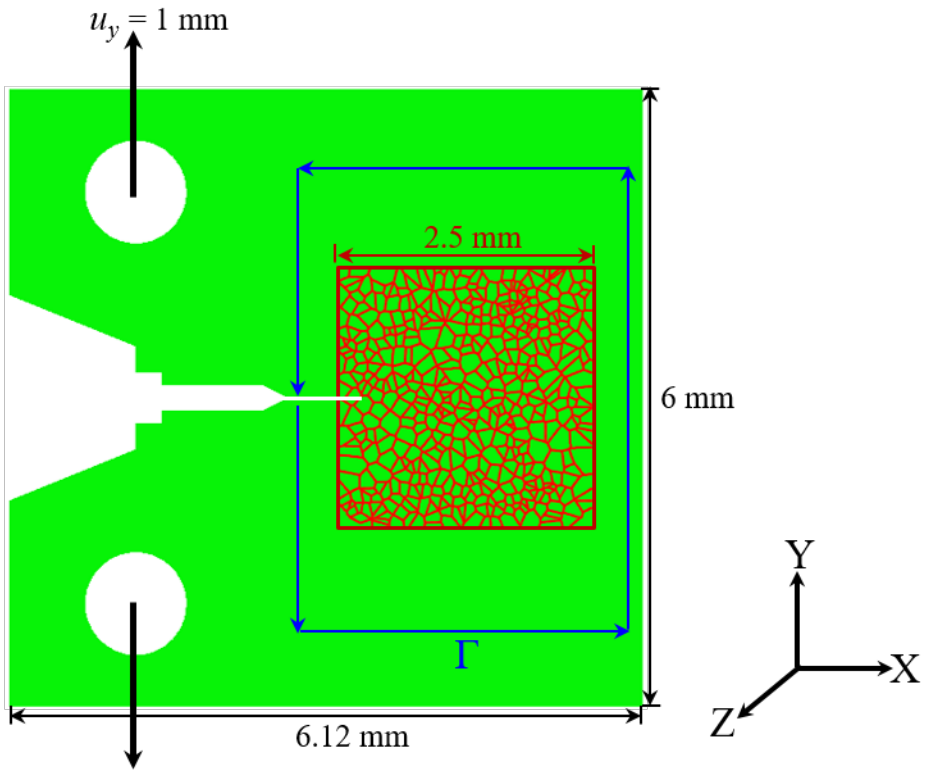

Figure 3.1: Multiscale computational framework for prediction of fracture toughness of ductile metals with microstructures.

3.3 Material models

In this section the constitutive relations used for the materials are discussed. The bulk material follows a simple bilinear elastic-plastic constitutive law. The grains within the microstructure region assumes the same bilinear stress-strain response for the first part of the work in which the focus is on exploring the effects of grain boundary behavior. Later, crystal plasticity theory is used to model anisotropic deformation of grains. Crystal plasticity formulation is introduced in 2D in order to investigate the effects of crystallographic texture on fracture. The interfaces within the grains and along the grain

boundaries follow cohesive traction-separation laws that evolve with the grain boundary misorientation angle.

3.3.1 Bilinear elastic plastic constitutive relation

In order to model a ductile material response, a bilinear elastic-plastic constitutive relation is assumed. The constitutive law follows the following equation.

$$\boldsymbol{\sigma} = \mathbf{C}\left(\boldsymbol{\varepsilon} - \boldsymbol{\varepsilon}_{\mathbf{p}}\right), \tag{3.1}$$

where $\boldsymbol{\sigma}$, $\boldsymbol{\varepsilon}$, $\boldsymbol{\varepsilon}_{\mathbf{p}}$, and $\mathbf{C}$ represent the stress, strain, plastic strain, and the stiffness tensor respectively. The stress tensor could be decomposed in terms of the hydrostatic component (σ_h) and the deviatoric component ($\mathbf{S}$).

$$\left.\begin{aligned} \sigma_{ij} &= \sigma_h \delta_{ij} + S_{ij}, \\ \sigma_h &= \frac{1}{3} tr\left(\boldsymbol{\sigma}\right). \end{aligned}\right\} \tag{3.2}$$

The Mises equivalent stress $(\bar{\sigma})$ and similarly, the effective plastic strain $\left(\bar{\varepsilon}^{p}\right)$ are defined as,

$$\left.\begin{aligned}\bar{\sigma} &= \sqrt{\frac{3}{2}\mathbf{S}:\mathbf{S}}, \\ \bar{\varepsilon}^{p} &= \sqrt{\frac{2}{3}\left(\boldsymbol{\varepsilon}-\frac{1}{3}tr(\boldsymbol{\varepsilon})\mathbf{I}\right):\left(\boldsymbol{\varepsilon}-\frac{1}{3}tr(\boldsymbol{\varepsilon})\mathbf{I}\right)},\end{aligned}\right\} \tag{3.3}$$

where **I** is a 2nd order identity tensor. Beyond yielding, the equivalent stress-strain response follows the linear equation given as,

$$\bar{\sigma} = \sigma_y + k\bar{\varepsilon}^{p}, \tag{3.4}$$

where, σ_y is the Mises yield stress that corresponds to the yield strength estimated from uniaxial tensile test of a material and the k represents the strain hardening in this bilinear equivalent stress-strain curve. The magnitudes of these parameters are taken from [76]. The solid black line in Figure 3.2(a) shows the equivalent stress-strain constitutive law for the Mo. The dotted lines correspond to the other four levels of yield strength considered. The rate of strain hardening remains the same in all five cases. Figure 3.2(b) depicts that the bilinear stress-strain model is in close agreement with the experimentally obtained stress-strain response of unalloyed Mo [76].

For isotropic material response in the homogeneous region,

$$\boldsymbol{\sigma} = \frac{\bar{E}}{1+\bar{\nu}}\boldsymbol{\varepsilon} + \frac{\bar{\nu}\bar{E}}{(1+\bar{\nu})(1-2\bar{\nu})}tr(\boldsymbol{\varepsilon})\mathbf{I}, \tag{3.5}$$

where $\bar{E}$ represents the effective elastic modulus and $\bar{\nu}$ is the effective Poisson's ratio for the homogeneous material. Within the microstructure region, the grains either follow an isotropic elastic plastic constitutive law or an orthotropic elastic plastic constitutive law. For the orthotropic elastic response inside the bulk microstructure region, the stiffness tensor is defined as

$$C = \begin{bmatrix} C_{11} & C_{12} & C_{13} & 0 & 0 & 0 \\ & C_{22} & C_{23} & 0 & 0 & 0 \\ & & C_{33} & 0 & 0 & 0 \\ & & & C_{44} & 0 & 0 \\ & & & & C_{44} & 0 \\ & & & & & C_{66} \end{bmatrix} \tag{3.6}$$

The effective elastic constants for the homogeneous region are calculated using the self-consistent method as [87], i.e.,

$$\left.\begin{aligned} \bar{G} &= \frac{4\left(C_{11}-C_{13}\right)+2\left(C_{33}-C_{12}\right)+6\left(C_{66}+2C_{44}\right)}{60}+ \\ &\quad \frac{15}{4}\left\{\frac{2\left(C_{11}+C_{12}\right)+C_{33}+4C_{13}}{\left(C_{11}+C_{12}\right)C_{33}-2C_{13}^2}+\frac{3}{C_{11}-C_{22}}+\frac{1.5}{C_{66}}+\frac{3}{C_{44}}\right\}^{-1}, \\ \bar{B} &= \frac{1}{18}\left(2C_{11}+C_{33}+2C_{12}+4C_{13}\right)+\frac{C_{33}\left(C_{11}+C_{12}\right)-2C_{13}^2}{2\left(C_{11}+C_{12}+C_{33}+4C_{13}\right)}, \\ \bar{E} &= \frac{9\bar{B}\bar{G}}{3\bar{B}+\bar{G}}, \text{ and } \bar{\nu} = \frac{3\bar{B}-2\bar{G}}{6\bar{B}+2\bar{G}}. \end{aligned}\right\} \tag{3.7}$$

Where $\bar{G}$, and $\bar{B}$ represent the effective shear, and bulk modulus of the polycrystalline aggregate respectively. The magnitudes of all these elastic constants are taken from [88] and are shown in Table 3.1.

Table 3.1: Properties of pure Mo.

C_{11} (MPa)	C_{12} (MPa)	C_{44} (MPa)	v	σ_y (MPa)	k (MPa)
449970	172870	124970	0.38	385	13700

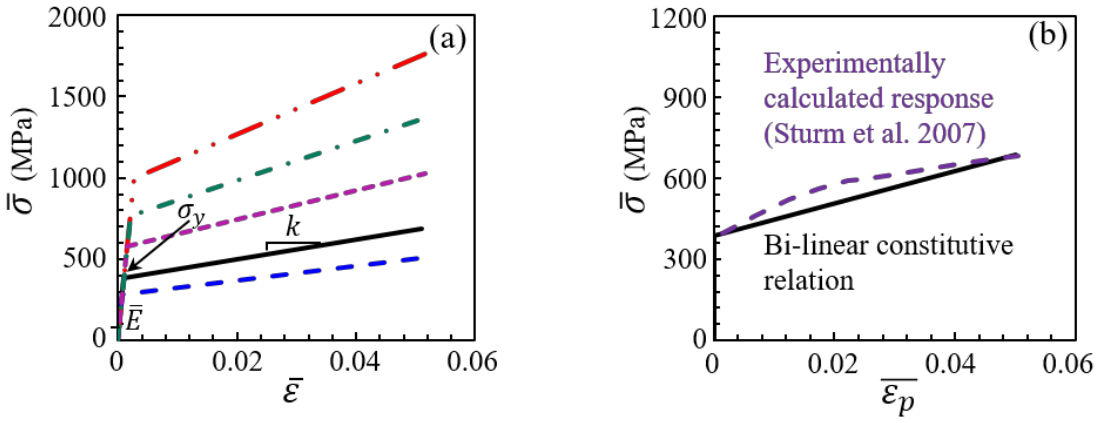

Figure 3.2: (a) Bi-linear elastic-plastic constitutive relations for Mo at different yield stress levels, (b) comparison of the bi-linear material model with experimentally determined stress-strain response of Mo.

3.3.2 Traction-separation laws for the interfaces

In order to model arbitrary crack propagation through the grains and GBs, zero thickness 2D cohesive elements are inserted everywhere within the microstructure region. The cohesive elements follow a bilinear traction separation law implemented in ABAQUS. In this cohesive model, the traction applied on any cohesive surface (**t**) is work conjugate to the interfacial separation $(\boldsymbol{\delta})$. For 2D zero thickness cohesive elements, the uncoupled traction-separation constitutive relation can be written as,

$$\mathbf{t} = \begin{Bmatrix} t_n \\ t_s \end{Bmatrix} = \begin{bmatrix} K_{nn} & 0 \\ 0 & K_{ss} \end{bmatrix} \begin{Bmatrix} \delta_n \\ \delta_s \end{Bmatrix}, \tag{3.8}$$

where $t_n = \mathbf{n} \cdot \mathbf{t}$, $t_s = \mathbf{s} \cdot \mathbf{t}$, $\delta_n = \mathbf{n} \cdot \boldsymbol{\delta}$, and $\delta_s = \mathbf{s} \cdot \boldsymbol{\delta}$ are the normal and tangential components of $\mathbf{t}$ and $\boldsymbol{\delta}$, respectively, and $\mathbf{n}$, $\mathbf{s}$ are the unit vectors normal and tangential to the cohesive surface. $\mathbf{K}$ represents the stiffness tensor connecting $\mathbf{t}$ and $\boldsymbol{\delta}$. δ_{nc} and δ_{sc} are the critical normal and shear separations at which the cohesive strength vanishes and the cohesive element fails. Damage sets in when the following criterion is satisfied.

$$\left\{ \left(\frac{t_n}{t_n^{\max}} \right)^2 + \left(\frac{t_s}{t_s^{\max}} \right)^2 \right\} = 1. \tag{3.9}$$

In our calculations, the maximum cohesive strength is assumed to be the same in both the normal and tangential direction and is denoted as $T_{\max}$.

$$t_n^{\max} = t_s^{\max} = T_{\max}. \tag{3.10}$$

Damage evolves linearly and the material softens until the energy dissipated reaches the critical cohesive energy level denoted as Φ_0. A scalar damage variable D represents the overall damage behavior in the material, and the traction components are affected by the damage according to

$$\left.\begin{aligned} t_n &= (1-D)t_n', \quad t_n' \geq 0 \\ t_s &= (1-D)t_s', \end{aligned}\right\} \tag{3.11}$$

where $\mathbf{t}'$ represents the traction components predicted by eq. (3.8) without considering damage. The limiting values of $D=0$ and $D=1$ correspond to zero separation and complete element degradation, respectively. Complete separation occurs when the resultant separation $\left(\delta_m = \sqrt{\delta_n^2 + \delta_s^2}\right)$ reaches the critical value of separation $\left(\delta_m^c\right)$ such that

$$\frac{1}{2} \cdot T_{\max} \cdot \delta_m^c = \Phi_0. \tag{3.12}$$

The normalized traction τ and the normalized separation λ shown in the Figure 3.3(a) are defined as,

$$\left.\begin{aligned} \tau &= \frac{t}{T_{\max}} = \sqrt{\left(\frac{t_n}{t_n^{\max}}\right)^2 + \left(\frac{t_s}{t_s^{\max}}\right)^2}, \\ \lambda &= \frac{\delta_m}{\delta_m^c} = \sqrt{\left(\frac{\delta_n}{\delta_{nc}}\right)^2 + \left(\frac{\delta_s}{\delta_{sc}}\right)^2}, \\ \delta_{nc} &= \delta_{nc} = \delta_m^c. \end{aligned}\right\} \tag{3.13}$$

The variable $\lambda_0 = \delta_m^0 / \delta_m^c$ denotes the normalized separation at which damage sets in and the traction reaches the maximum value. Hence the reciprocal of λ_0 represents the initial stiffness of the normalized traction-separation cohesive relation.

In order to incorporate the effect of GB characteristics on fracture, we invoke the theory of internal state variables and express the cohesive parameters as function of the GB misorientation angles. Different properties are assigned to the interfaces within the grains and along the GBs. Along the GBs, the cohesive energy of the interfaces vary with the GB misorientation angle (θ).

$$\left.\begin{aligned} \Phi &= \Phi\left(T_{\max}, \delta_m^c\right), \\ T_{\max} &= \hat{T}_{\max}\left(\theta\right). \end{aligned}\right\} \tag{3.14}$$

According to the experimental observations reported in the literature [69], GBs with misorientation between 15˚-75˚ are more prone to fracture than the other boundaries. The

variation of fracture strength with the GB misorientation angle as reported in [69] could be approximated by a sinusoidal function as formulated below.

$$\left.\begin{aligned} T_{GB}(\theta) &= C_1 + C_2\cos(4\theta), \\ C_1 &= \frac{1}{2}\left(T_G + T_{GB}^{\min}\right), \\ C_2 &= \frac{1}{2}\left(T_G - T_{GB}^{\min}\right). \end{aligned}\right\} \tag{3.15}$$

T_G and $T_{GB}^{\min}$ represent the maximum and minimum values of the GB fracture strength (T_{GB}), respectively. The maximum value of the GB fracture strength is the same as the interfacial strength within the grains $\left(T_{GB}^{\max} = T_G\right)$. Figure 3.3(b) shows profiles of the GB fracture strength for different values of $T_{GB}^{\min}$ while T_G is kept constant. These cases can be distinguished by the ratio $Q = T_G / T_{GB}^{\min}$, which represents the degree of variation of $T_{GB}(\theta)$ as the GB misorientation angle changes. The values of the cohesive parameters used are shown in the Table 3.2. The maximum cohesive energy used in this model scales with the fracture toughness of pure Mo. The range of misorientation dependent variation of the GB fracture strength is obtained from the experimental observations reported in the literature [69]. Further calibration of the cohesive parameters is described in the next section. Following the convergence criterion described by [84], the lower bound of the cohesive element size [89] is estimated as,

$$d_z \geq \frac{\lambda_o \delta_{sc}}{T_{\max}} \frac{\bar{E}}{\left(1-\bar{\nu}^2\right)} \frac{\sqrt{2}+1}{1-\bar{\nu}} = 0.006\ \mu\text{m}. \tag{3.16}$$

The upper bound of the cohesive element size is given as,

$$d_z \le \frac{9\pi}{32}\frac{\bar{E}}{\left(1-\bar{\nu}^2\right)}\frac{\Phi_o}{T_{\max}^2} = 360\ \mu\text{m}. \tag{3.17}$$

The element size (5 μm) used in this work falls well within this range and also efficiently models the grain structure.

Table 3.2: Interfacial parameters

Q	K_{nn} (MPa)	$(\Phi_0)_{\max}$ (kJ/mm^2)	T_G (MPa)	$T_{GB}^{\min}$ (MPa)
1.1	500×10^6	1	962.5	875
1.5	500×10^6	1	962.5	641.67
2.0	500×10^6	1	962.5	481.25

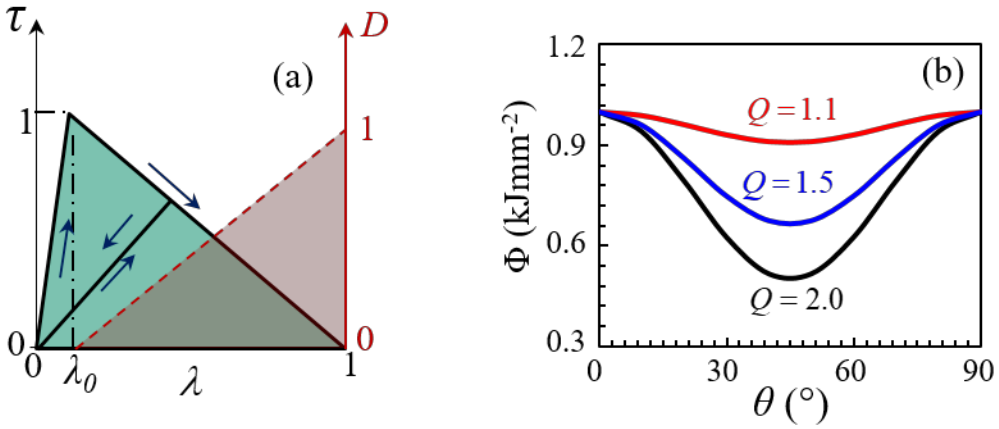

Figure 3.3: (a) Bi-linear traction-separation relation for the cohesive crack faces, (b) variation of the cohesive energy with grain boundary misorientation angle.

3.3.3 Crystalline plasticity formulation for the grains

Plastic deformation in metals is a manifestation of dislocation motion and interaction at the microscopic scale. The details are intimately related to the crystallographic structure of the material as well as the current state of the microstructure. Macroscopic models of plasticity lack the ability to link these fundamental mechanisms to the bulk material response without very substantial experimental characterization. Many formulations of constitutive laws for the elastic-plastic deformation of single and polycrystals have long been proposed [90-94]. The basic premise of these theories is that macroscopic plastic deformation is related to the cumulative process of slip system shearing relative to the lattice. This methodology provides a physical link between the processes at different length scales. The two basic components of crystal plasticity model are the kinematic and kinetic relations.

The multiplicative decomposition of the total deformation gradient is given by

$$\mathbf{F} = \mathbf{F}^e \cdot \mathbf{F}^p, \tag{3.18}$$

where $\mathbf{F}^e$ is the elastic deformation gradient representing the elastic stretch and rotation of lattice, and $\mathbf{F}^p$ is the plastic deformation gradient describing the collective effects of dislocation motion along the active slip planes relative to a fixed lattice in the reference configuration. Unit vectors $\boldsymbol{s}_0^\alpha$ and $\boldsymbol{n}_0^\alpha$ denote the slip direction and the slip plane normal direction, respectively for the α^{th} slip system in the undeformed configuration. The

resolved shear stress on each slip system is related to the Cauchy stress tensor $\boldsymbol{\sigma}$ according to

$$\tau^{\alpha} = \boldsymbol{\sigma}:\left(\boldsymbol{s}^{\alpha} \otimes \boldsymbol{n}^{\alpha}\right), \tag{3.19}$$

where the slip vectors have been rotated into the current configuration. Under the application of the resolved shear stress, the shearing rates $\dot{\gamma}^{\alpha}$ on the slip systems are related to the plastic velocity gradient in the intermediate configuration according to

$$\mathbf{L}^{p} = \sum_{\alpha} \dot{\gamma}^{\alpha} \mathbf{s}_{0}^{\alpha} \otimes \mathbf{n}_{0}^{\alpha}, \tag{3.20}$$

with $\dot{\gamma}^{\alpha}$ ascribed to follow the rate-dependent flow rule as

$$\dot{\gamma}^{\alpha} = \dot{\gamma}_{0} \left\langle \frac{\tau^{\alpha} - \chi^{\alpha}}{g^{\alpha}} \right\rangle^{m} \operatorname{sgn}\left(\tau^{\alpha} - \chi^{\alpha}\right), \tag{3.21}$$

where m is the inverse strain rate sensitivity exponent and g^{α} and χ^{α} are drag stress and back stress, respectively on the α^{th} slip system. These quantities evolve according to

$$\begin{cases} \dot{g}^{\alpha} = H \sum_{\beta=1} q^{\alpha\beta} \left|\dot{\gamma}^{\beta}\right|, \text{ and} \\ \dot{\chi}^{\alpha} = A_{kin} \dot{\gamma}^{\alpha} - A_{dyn} \chi^{\alpha} \left|\dot{\gamma}^{\alpha}\right|. \end{cases} \tag{3.22}$$

Here $q^{\alpha\beta}$ is the latent hardening coefficient, H, A_{kin} and A_{dyn} are the isotropic hardening, kinematic hardening and dynamic recovery coefficients, respectively. These non-linear coupled differential equations are solved using UMAT [95].

For Mo with bcc crystal structure 24 slip systems of {110}<111> type are considered since the prior experimental works suggest that almost under all circumstances, activation of the {110}<112> type slip systems is rather rare [96-99]. Also, for bcc crystals, the dislocation core spreads into multiple planes and that gives rise to twinning-anti-twinning asymmetry in yielding. The criterion for yielding thus considers two shear stresses parallel and two shear stresses perpendicular to the slip direction, both resolved in two different {110} planes of the zone of the slip direction. For the [111] slip direction such a yield criterion is expressed as [97],

$$\sigma^{(\bar{1}01)} + a_1\sigma^{(\bar{1}01)} + a_2\tau^{(\bar{1}01)} + a_3\tau^{(\bar{1}01)} = \tau_{CRSS}, \tag{3.23}$$

where $\sigma^{\{110\}}$ and $\tau^{\{110\}}$ are the shear stresses parallel and perpendicular to the slip direction, respectively, in the corresponding {110} planes. The first term in the above equation is the Schmid stress and this drives the dislocation motion in the glide plane and does work through the glide. The last three terms are the non-Schmid stresses that affect the dislocation core but do not do any work when the dislocation glides. The values of the coefficients a_1, a_2, and a_3 are taken from[97].

The phenomenologically assigned 3D orientations of the grains are first used to identify the orientation of the slip systems with respect to the XY plane of the 2D specimen.

Any slip system that lies out of the plane of the specimen is arbitrarily assigned a CRSS which is one order of magnitude higher than the CRSS values for primary slip systems lying in the XY plane of the specimen. This is to ensure that the slip systems lying out of the plane is never activated. Also, the 2D crystal plasticity model employs a single slip model to represent the macroscopic uniaxial stress-strain behavior of Mo. Cross-slip within a single grain is neglected. Figure 3.4 shows the effective stress-strain curve obtained using this single slip assumption on a 2D microstructure with randomly oriented grains under plane strain conditions does not deviate much from the experimentally obtained stress-strain curves reported in [76]. The single slip assumption results in higher constraints for plastic deformation and as an outcome the grains yield at a relatively higher value of stress than what is experimentally observed. Even though the model overestimates the yield stress, the hardening is very similar to what is observed in experiments. Further 2.5D and 3D models are developed where multiple slip systems get activated simultaneously and thus simulates more realistic plastic deformation behavior of the grains.

Table 3.3: Crystal plasticity model parameters for bcc Mo

$\dot{\gamma}_0$	m	a_0	A_{dyn}	A_{kin}	$q^{\alpha\beta}$
0.1	13	0	8	400	50

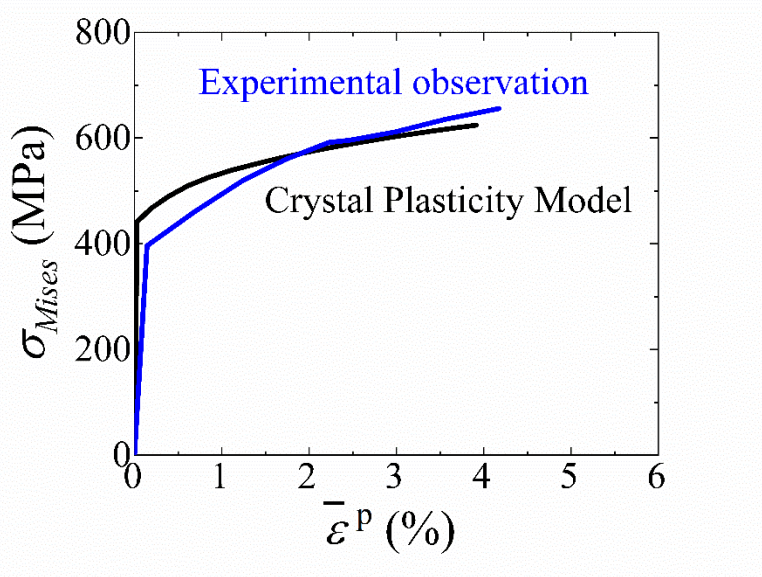

Figure 3.4: Comparison of the Mises stress – effective strain response calculated from the crystal plasticity model with experimental observation as reported in [76].

3.4 Summary

A cohesive finite element method (CFEM) based multiscale computational framework is developed for predicting fracture toughness of materials as function of microstructure. This framework provides a means for evaluating fracture toughness through explicit simulation of fracture processes in microstructures. The approach uses the *J*-integral, allowing fracture toughness to be calculated for microstructures with random heterogeneous phase distributions and fracture processes with arbitrary crack paths or micro-crack patterns. Both 2D and 3D frameworks are developed. Although this dissertation focuses on specific materials, the methodology developed can be applied to any material system in principle.

4 DETERMINATION OF FRACTURE TOUGHNESS AND MODEL CALIBRATION

4.1 Introduction

The multiscale framework described in chapter 3 enables us to calculate the macroscale fracture response in terms of the fracture toughness K_{IC}, J_{IC}. Also, the framework captures the competition between different fracture mechanisms by explicitly tracking the crack path through the polycrystalline microstructure. The framework also facilitates capturing the competition between plastic deformation and crack growth. In this chapter, the methods to determine the overall fracture response and capture the two competitions are described in detail. The model parameters are calibrated to match properties of bcc Mo.

Section 4.2 explains the way to evaluate the fracture toughness and calibrates the model to simulate fracture processes in Mo. Section 4.3 establishes mathematical expressions to characterize the crack path and thus the fracture mechanisms. Section 4.4 discusses the specimen size effect.

4.2 Evaluation of fracture toughness

According to the ASTM standard [86], fracture toughness is calculated from the load (P) vs load line displacement (LLD) curves recorded from the loading event of the CT specimen. The same P vs LLD curves are obtained from the computational experiment and

the plastic zone size at the growing crack tip is calculated. In order to calibrate the model parameters, multiple calculations are performed at different levels of relative strength between the interfaces and the grains γ, defined as the ratio between the interfacial strength and the yield strength of the material, i.e.,

$$\gamma = \frac{T_G}{\sigma_y}. \tag{4.1}$$

For the purpose of calibration, homogenized material properties are considered throughout the design space. *P* vs LLD curves are plotted for all five cases along with the crack extension (Δa) as shown in Figure 4.1. As the figure suggests, the material fails at a higher load level as the normalized interfacial strength (γ) increases. Also, the rate of crack propagation decreases as the γ increases.

Figure 4.2 shows the evolution of the plastic zone size ahead of a growing crack. As the figure suggests the plastic zone size at the crack tip reaches a steady state and remains constant after a finite amount of crack extension. The growing crack attains the steady state earlier for a higher value of γ. The region of constant plastic zone size signifies steady state crack growth. In other words, plastic zone required to extend the crack becomes constant per unit extension of the crack. As shown in the Figure 4.3, the steady state crack growth within the microstructure region is not influenced by the plasticity at the back face of the specimen. Also, the microstructure region is large enough so that there is no edge/boundary effect on the steady state crack growth. Crack growth through or around 10-15 grains is considered for the analyses.

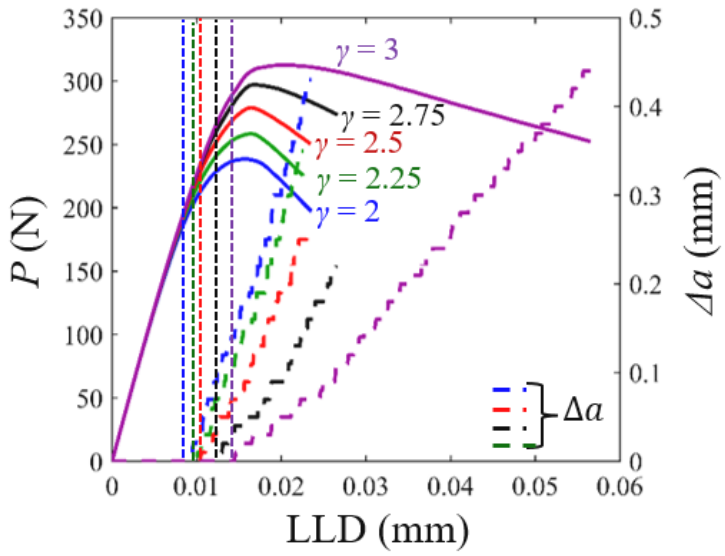

Figure 4.1: Load (P) -Load line displacement (LLD) - crack extension (Δa) relations obtained from numerical simulations for five levels of the ratio (γ) between interfacial strength and grain yield strength for homogeneous Mo without microstructure.

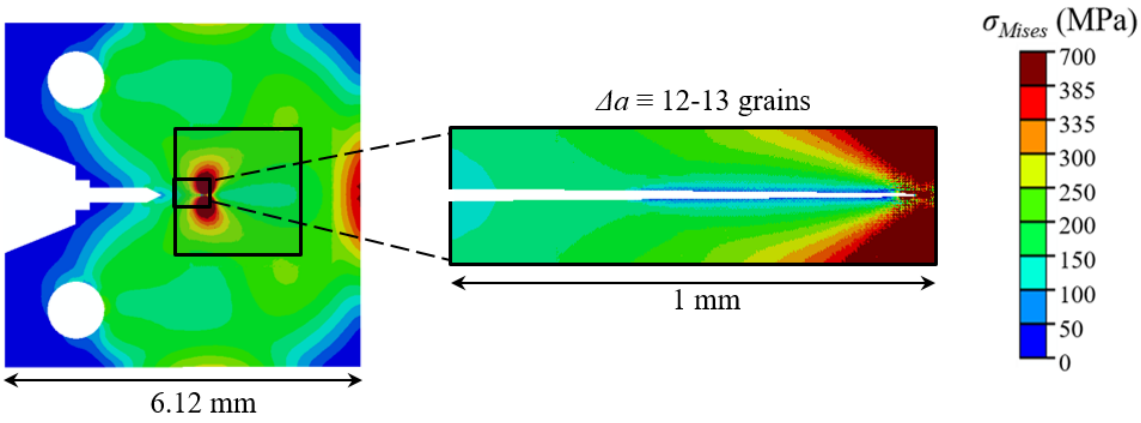

Figure 4.2: Steady state crack propagation in a standard small volume CT specimen.

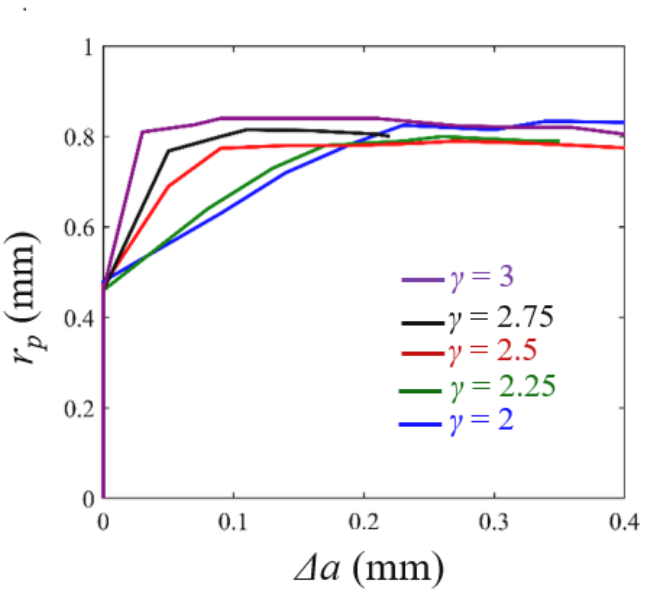

Figure 4.3: Evolution of the plastic zone size (r_p) as crack growth occurs at five levels of the ratio (γ) between interfacial strength and grain yield strength for homogeneous Mo without microstructure.

For plane strain fracture toughness (K_{IC}) measurement to be valid, the specimen dimensions should satisfy the following condition.

$$a, (W - a) \geq 8 r_p, \tag{4.2}$$

where, a and W denote the projected length of the growing crack and the width of the specimen (5 mm in our case) respectively. In all the cases, this condition is not satisfied due to the smaller dimensions of the specimen and higher plasticity of the constituents. Hence, K_{IC} cannot be calculated directly from the P vs LLD plots.

Therefore, we attempt to calculate the *J*-integral using paths through the homogeneous region outside the microstructure, around the crack, away from the crack tip. The *J*-integral is defined as [100],

$$\left.\begin{aligned} J &= \int_{\Gamma}\left(w dy - T_i \frac{\partial u_i}{\partial x} ds \right), \\ w &= \int_0^{\varepsilon_{ij}} \sigma_{ij} d\varepsilon_{ij}, \\ T_i &= \sigma_{ij} n_j . \end{aligned}\right\} \tag{4.3}$$

Γ is the crack tip contour along which the integral is calculated as indicated in Figure 3.1. Figure 4.4 shows the *J*-integral values as a function of crack extension for five different levels of the γ for the homogeneous isotropic elastic plastic material response. The value of *J* integral corresponding to the crack initiation is termed as J_i and the value corresponding to the attainment of steady-state is termed as J_{ss}. For J_{IC} calculations to be valid,

$$a, (W-a), b \geq \frac{25 J_{ss}}{\sigma_y}. \tag{4.4}$$

Our specimen configuration satisfies this condition for valid J_{IC} estimation.

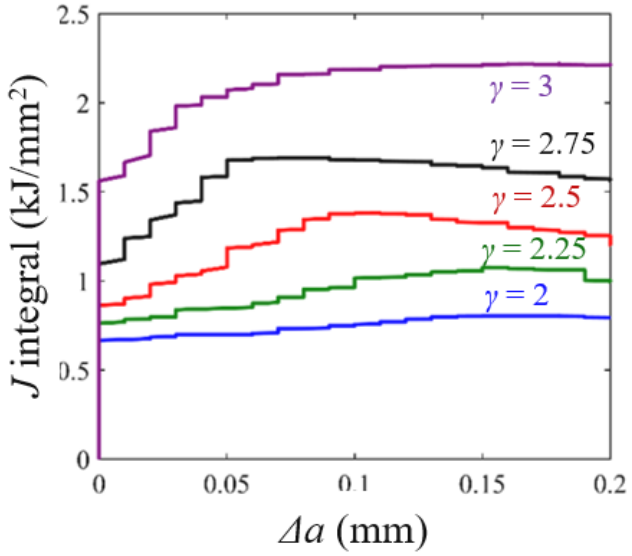

Figure 4.4: Variation of *J*-integral with crack extension (Δa) at five levels of the ratio (γ) between interfacial strength and grain yield strength for homogeneous elastic-plastic Mo without microstructure.

For an elastic-plastic material modeled using incremental theory of plasticity, the *J*-integral takes into account the energy dissipated through both new surface creation and plastic deformation around the crack tip. As suggested by Rice et al., *J*-integral can also be calculated from a single *P* vs LLD curve, using a point of criticality. The equation for calculation of *J*-integral from a CT specimen is given as [101],

$$J = \frac{P\delta_{crack}}{b}\left(1+16\beta D^2\left[\frac{P}{P_{\max}}\right]^2\right), \tag{4.5}$$

where, δ_{crack} is the crack tip opening displacement, and β, D are the geometric constants. The values of these constants are taken from [101]. Figure 4.5 compares the thus calculated J values with the magnitudes of J_i and J_{ss} calculated through integration following eq. (4.3) for all five levels of the normalized interfacial strength. The J values calculated from eq. (4.5) corresponding to the initiation of the crack, match perfectly with the values of J_i. In case of the J values corresponding to the attainment of steady state crack propagation, the integration method tends to underestimate the values. For higher levels of normalized interfacial strength, the difference between the J values calculated through eq. (4.3) and that calculated using eq. (4.5) narrows down and they are in close agreement for the case of $\gamma = 2.5$. For all our calculations, the method of integration is employed to calculate the J as a function of the crack extension since the integration scheme uses the stress-strain field around the crack tip and is not directly dependent upon the geometric factors. Therefore, the area integral is believed to yield more reliable measures of fracture toughness as a function of material properties rather than the geometric factors of the specimen. Hence, we calculate J_i and J_{ss} using the integration method and following the popular convention, the J_{ss} is termed as the J_{IC} and it marks the beginning of steady state crack propagation.

Since, J_{IC} measurement is valid with our specimen configuration, K_{IC} is calculated using the following equation for plane strain condition.

$$K_{IC} = \sqrt{\frac{J_{IC}\bar{E}}{1-\bar{\nu}^2}}. \tag{4.6}$$

Figure 4.6 shows the J_i, J_{IC} values along with the values of K_i, K_{IC} calculated using the abovementioned equation. As the normalized interfacial strength increases, the values of fracture toughness increases. The experimentally determined fracture toughness of pure Mo with a grain size of 97 μm is 24.2 $\pm$ 2.3 MPa$\sqrt{m}$ [76]. The K values fall well within this range for the case of γ = 2.5. Hence we take this value of γ for all our subsequent calculations.

The J-integral accounts for the total energy dissipated through the process of deformation and fracture and thus could be written as a sum of the energy dissipated due to the new surface creation and the plastic deformation. Thus,

$$J = J_S + J_P. \tag{4.7}$$

The J_S exactly equals the interfacial energy required for the crack to grow. Hence,

$$J_S = \Phi\left(T_{\max}\left(\theta\right), \delta_m^c\right). \tag{4.8}$$

Equations (4.7) and (4.8) allow the plastic dissipation rate to be calculated easily. The J_P thus exclusively quantifies the contribution of plasticity towards the fracture resistance.

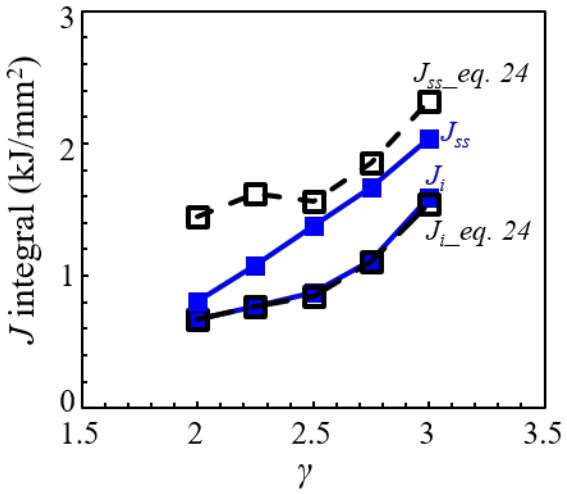

Figure 4.5: Comparison of the fracture resistance in terms of J_i and J_{ss} calculated using the area integral with that calculated using the empirical equation proposed by Rice et al. [101].

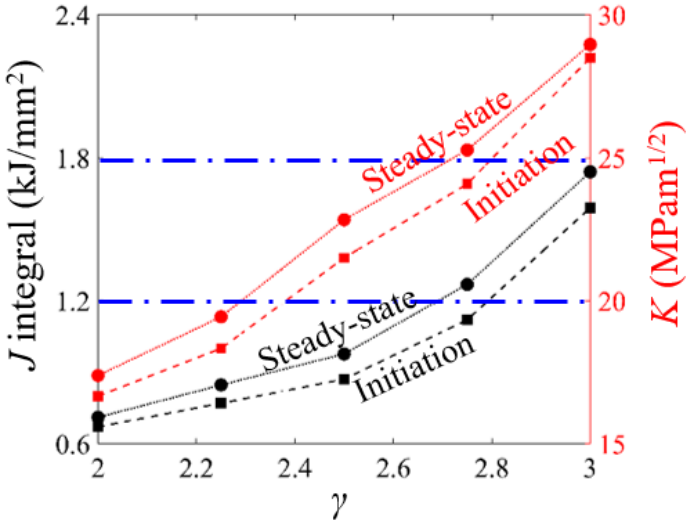

Figure 4.6: Fracture toughness in terms of J and K at crack initiation and at attainment of steady-state crack growth over a range of γ.

4.3 Evaluation of fracture mechanisms

The CFEM based model explicitly tracks the intergranular and transgranular fracture mechanisms. The crack propagation paths are resolved along three directions with respect to the loading direction (0˚, ±45˚, 90˚). The relative contribution of different mechanisms towards the overall crack propagation path is quantified through the following fractions.

$$\left.\begin{aligned} H_g &= \frac{L_g}{L_g + L_{gb}}, \\ H_{gb} &= \frac{L_{gb}}{L_g + L_{gb}}. \end{aligned}\right\} \tag{4.9}$$

H_g and H_{gb} represent the overall proportion of transgranular crack path, and the intergranular crack path respectively. The L measures the true length of the crack. In addition, the crack path tortuosity (ξ) is quantified as,

$$\xi = \frac{L}{a}, \tag{4.10}$$

where a represents the projected crack length. Systematic characterization of the crack paths and the crack path tortuosity enables capturing the competition between the two primary fracture mechanisms.

The quantification of various fracture mechanisms and the crack path tortuosity also helps us quantify the J_S as a function of the crack path descriptors.

$$J_S\left(H_g, H_{gb}, \xi, \Phi\right) = \xi\left(H_g \Phi_g + H_{gb}\Phi_{gb}\left(\theta\right)\right). \tag{4.11}$$

Equations (4.7) and (4.11) allows the contribution of plasticity to be calculated easily. Evaluation of the relative contributions of plasticity and surface energy release rate to the overall fracture resistance facilitates quantifying the competition between plasticity and new surface creation. Multiple instantiations of statistically similar microstructures are used to account for the stochasticity of fracture and different fracture mechanisms. The results from all these simulations performed on Mo with polycrystalline microstructure consisting of randomly oriented grains are discussed in the following sections.

4.4 Specimen size effect

In order to investigate the effect of specimen size on fracture resistance, the same computational framework is adopted on a specimen of 62.5 mm × 60 mm dimensions. Figure 4.7 compares the two specimen sizes. Similar to the previously explained computational framework microstructure is resolved in a region around the crack tip. Same displacement controlled mode I loading is applied to the specimen. Figure 4.8(a) shows the crack extension in these two specimens as the load line displacement increases. Even though the crack begins to extend at different stages of LLD, the crack growth rates are similar in the two cases. *J*-integral is calculated around the crack tip contour that passes through the homogenized region outside the microstructure. The crack growth resistance

curves in Figure 4.8 (b) show that, crack initiates at the same value of J, and also the steady state J values are close to each other. Therefore, the fracture toughness measurement is independent of the specimen size. The specimen-II (small volume specimen) is used for the entire study for saving computational expenses.

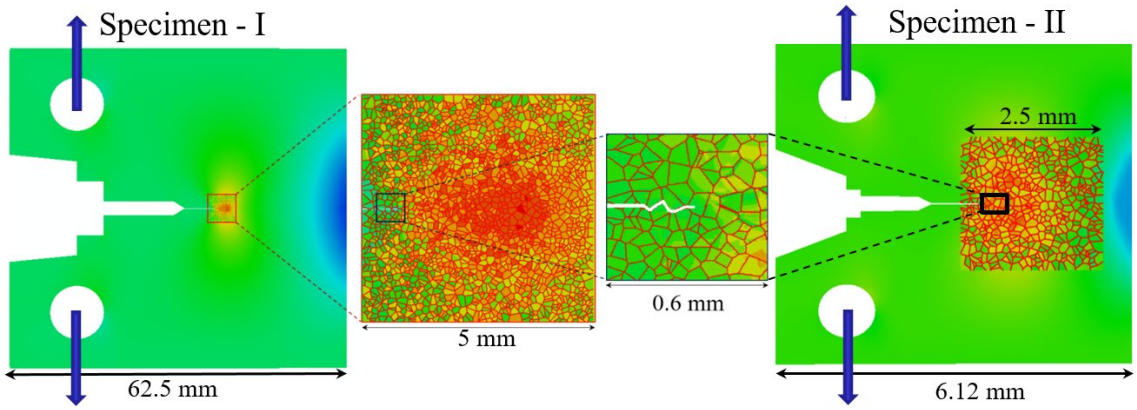

Figure 4.7: Comparison between the computational frameworks with two specimen dimensions.

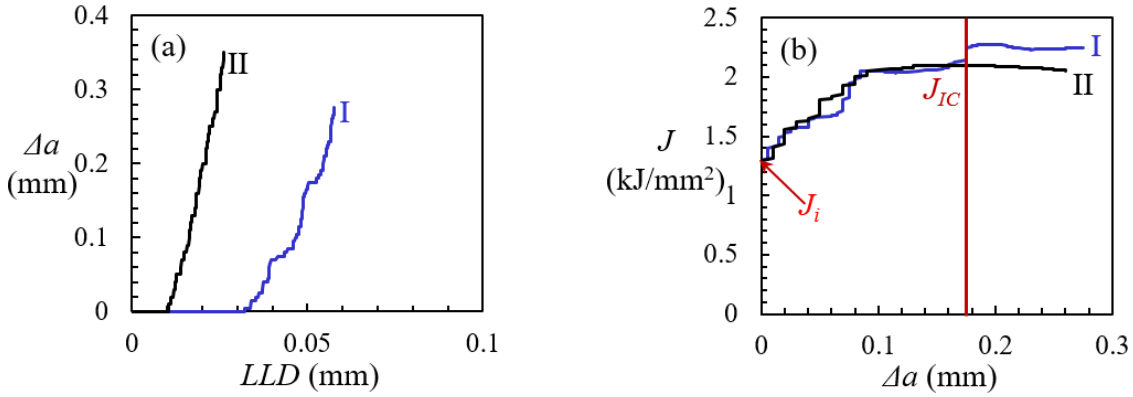

Figure 4.8: (a) crack extension vs LLD curves, (b) crack growth resistance curves obtained from the two specimens with different dimensions subjected to displacement controlled mode-I loading.

4.5 Summary

This chapter completes all the prerequisites to quantitatively establish the structure-property relations across length scales. The methodology establishes valid J_{IC} calculations and estimation of K_{IC} from the J_{IC} values. The model parameters are calibrated to match the fracture toughness of Mo using a homogenized material without any microstructural heterogeneities. The merit of this framework lies in the fact that it simulates real material behavior unlike some other models which analyze the effect of intergranular crack path on overall fracture toughness without paying heed to the real material behavior. Another merit of this computational framework calibrated to real material behavior is explicitly tracking intergranular and transgranular crack propagation. This chapter establishes how the model facilitates capturing the competitions between (a) intergranular and transgranular fracture, and (b) plastic deformation and new surface creation. This framework also has the capability to include all sorts of microstructural heterogeneities and analyze their effects on macroscale fracture toughness values and the fracture mechanisms. Even though the material of focus here is Mo, similar approach could be adopted for any other materials and thus could be used as a design tool that tailors microstructures for desired fracture behavior.

5 EFFECT OF GRAIN BOUNDARY CHARACTERISTICS ON FRACTURE

5.1 Introduction

The computational framework described in the previous chapters is adopted here to investigate fracture behavior in Mo. In this chapter, the focus is on establishing the effects of grain boundary characteristics in terms of the misorientation angle dependent fracture strength. Microstructures analyzed in this section have randomly oriented grains. The effect of grain boundary characteristics on fracture behavior in terms of fracture toughness, fracture micromechanisms, competition between plasticity and crack growth are systematically investigated in the following subsections.

5.2 Numerical Simulations

The simulations are carried out on four SEMSS with different mean intercept grain sizes in the range ~25 – 100 μm. The grains are randomly oriented for all these SEMSS. In order to focus on the misorientation dependent fracture behavior of the grain boundaries (GB), the anisotropy of grains is neglected. A simple bilinear elastic-plastic stress-strain response with isotropic hardening is assumed for the grains and the homogenized region outside the microstructure. A misorientation dependent interfacial law is assumed for the GB interfaces. Any direction in the grain is assumed to be equally likely to crack in terms of the assigned fracture energy. The GB strength profile is varied using three different Q ratios. Also, the yield strength is varied to investigate the influence of constituent plasticity

on the competition between transgranular and intergranular fracture, and the competition between plasticity and crack growth. The results of the microstructure based CFEM calculations, the subsequent fracture toughness measurement and analyses are discussed in this section. The fracture characteristics of all the specimens subjected to the same sets of loading conditions are compared in order to understand the effects of GB characteristics and plasticity on fracture behavior. In particular, systematic comparisons are made in terms of K_{IC}, J_{IC}, and H, ξ values.

.

5.2.1 Effect of grain boundary fracture strength

To explore the effect of GB fracture strength, three sets of simulations are performed using three different GB strength profiles characterized by three different Q values (Figure 3.3 (b)). The grain yield strength is the same (385 MPa) for the three cases. Figures 5.1 – 5.3 show the results obtained using the SEMSS with a mean grain size of ~95 μm.

Figure 5.1 shows the stress distributions and crack profiles of one sample in the SEMSS at the three different cases of GB fracture strength. As Q (the ratio between the maximum and minimum GB strengths) increases, the crack path becomes more tortuous and tends to meander through weaker GB sites. The intergranular fracture is predominant at the higher Q values (Figure 5.1(b) and (c)), as indicated by the H and ξ values. Figure 5.2(a) shows the load vs load line displacement curves along with the crack extension for the cases. As the GBs weaken, the crack initiation occurs earlier and the rate of crack propagation increases. The J vs crack extension profiles or crack growth resistance curve

Figure 5.2(b) corroborate the trend. The crack growth resistance increases as the GBs strengthen. The K_i and K_{IC} values obtained from the J_i and J_{IC} values are shown in Figure 5.3(a). For the material with the strongest GBs (Q=1.1), the K_{IC} lies in the range of 29.4 – 29.6 MPa√m. For the material with GBs having intermediate strength (Q=1.5), K_{IC} lies in the range of 24.8 – 26.8 MPa√m. For the material having the weakest GBs (Q=2.0), K_{IC} ranges from 20.7 – 23.3 MPa√m. The experimentally obtained value of K_{IC} for unalloyed Mo with a grain size of ~97 μm is 21.9-26.5 MPa√m [76]. Therefore, the K_{IC} values calculated using the weaker GBs $\left(Q \in [1.5,2]\right)$ are in agreement with the experimental values. Figure 5.3(b) can be used to analyze the different fracture mechanisms operative at different GB strength levels. Pure mode-I straight transgranular crack propagation dominates when the GBs are nearly as strong as the grains (Q=1.1, Figure 5.1(a)). As the GBs become weaker (Q increases), intergranular crack propagation starts to dominate. Also, the transgranular cracks preferentially propagate through interfaces perpendicular to the loading direction in a mode I fashion. The same trends are observed in all samples in the statistically equivalent microstructure sample set (SEMSS), with the fluctuations among the samples in the set indicated by the error bars. In the process, the crack path tortuosity ξ increases and approaches a plateau as Q increases beyond 1.5. The experimentally obtained fractographs for pure Mo with randomly oriented grains indicate that both intergranular and transgranular fracture mechanisms are operative (Figure 5.4). Sturm et al. report that the addition of Si renders the GBs more brittle, resulting in dominance of intergranular fracture as shown in Figure 5.4(c). This observation matches with the case of the weakest GB strength profile $\left(Q = 2\right)$. Thus, the simulations with

weaker GBs are in agreement with the experimental observations in terms of both the fracture toughness value and the fracture micromechanisms.

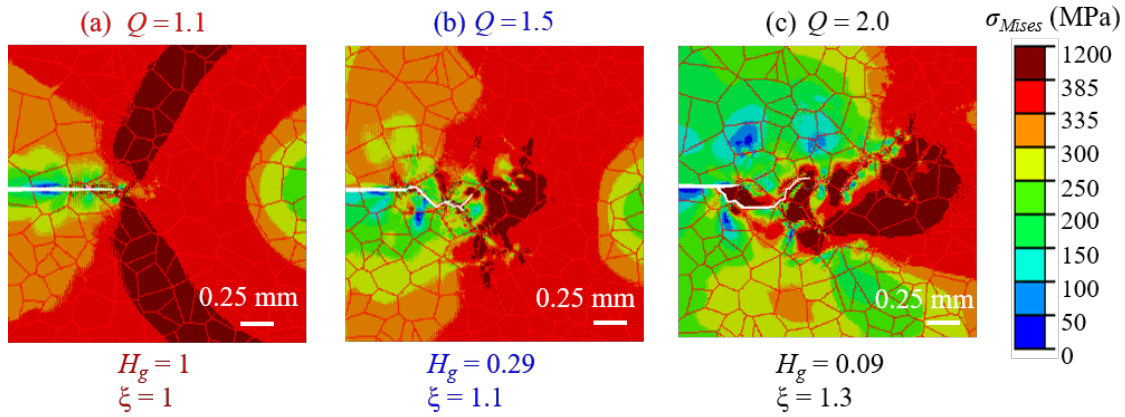

Figure 5.1: Crack propagation in a representative microstructure from the SEMSS with ~ 95 µm grain size for different levels of the ratio between maximum and minimum GB strength. The grain yield strength is 385 MPa in all cases.

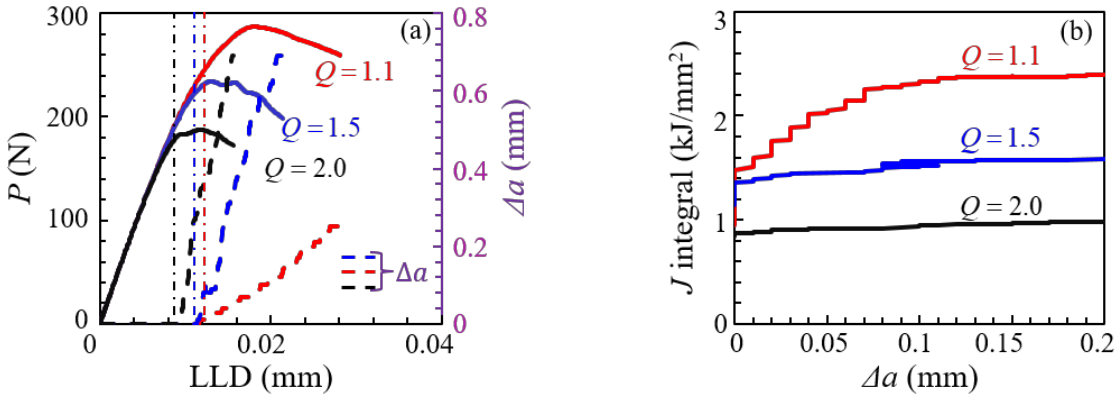

Figure 5.2: (a) Variation of load (P) and crack extension (Δa) with load line displacement (LLD), and (b) crack growth resistance curve in terms of J-integral vs crack extension (Δa) for different levels of the ratio between maximum and minimum GB strength. The grain yield strength is 385 MPa in all cases. The SEMSS with ~ 95 µm grain size is used.

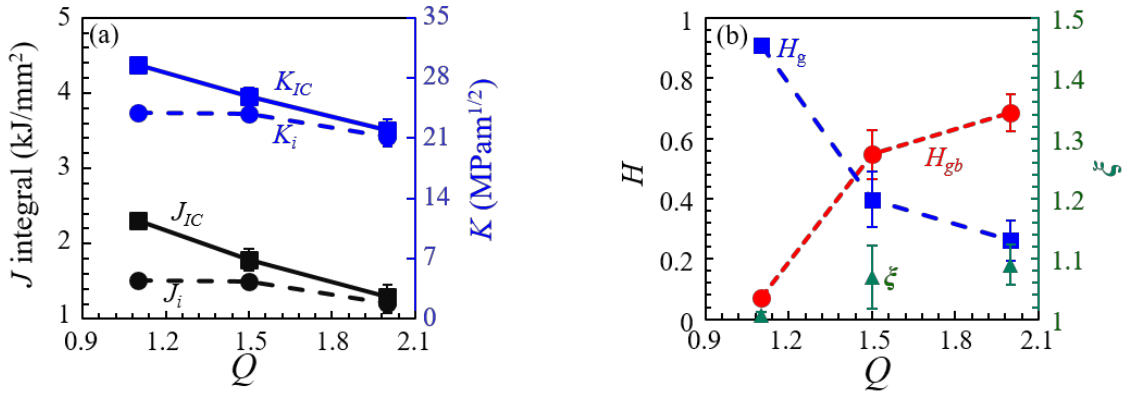

Figure 5.3: (a) Fracture resistance in terms of J_i, J_{IC}, K_i, and K_{IC} over a range of Q (ratio between maximum GB strength and minimum GB strength), and (b) fractions of crack lengths inside grains and along grain boundaries, and the crack path tortuosity (ξ) over a range of Q. The grain yield strength is 385 MPa in all cases, and the SEMSS with ~ 95 μm grain size is used.

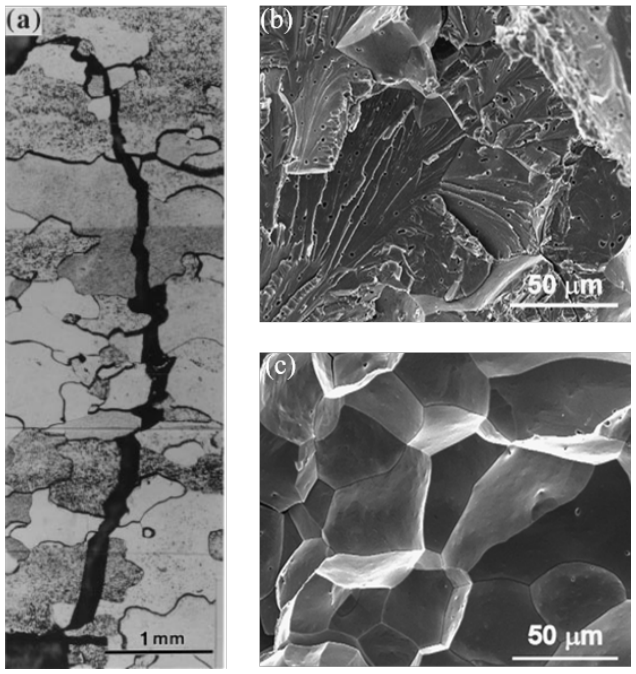

Figure 5.4: (a) Crack path in polycrystalline Mo [69], (b) transgranular crack propagation in unalloyed Mo, and (c) intergranular crack propagation in a Mo-0.5%Si alloy [76].

5.2.2 Competition between plasticity and crack formation

In order to analyze the effect of constituent plasticity on the fracture mechanisms, four other levels of grain yield strength $\left(\sigma_y = 285,\ 578,\ 770,\ 1000\ \text{MPa}\right)$ are considered. Three sets of calculations with different GB strength profiles are performed using the SEMSS for the ~95 μm grain size at all levels of the grain yield strength mentioned above. Figure 5.5 shows the overall fracture toughness in terms of both K_i and K_{IC} as a function of the yield strength normalized with the yield strength of the base material case $\left(\sigma_{y0} = 385\ \text{MPa}\right)$. The error bars indicate stochastic variation among samples in the SEMSS. The toughening effect of plasticity on fracture toughness values is more pronounced when the GBs are nearly as strong as the grain fracture strength. The amount of increase in crack growth resistance from initiation to steady state propagation decreases as the GB strength ratio increases. For $Q = 1.1$, Figure 5.5 (d) shows that the transgranular crack propagation prevails at all levels of grain plasticity. At the highest level of grain plasticity, crack initiates along the planes of maximum shear and as a result the crack path tortuosity is higher. Both crack path tortuosity and plasticity contribute to the enhancement of the overall fracture toughness. The effect is more clearly seen in the steady state fracture toughness (K_{IC}) than in the initiation fracture toughness (K_i). For $Q = 1.5$, Figure 5.5 (e) shows that both intergranular and transgranular fracture are operative. At the highest level of grain plasticity, the higher value of crack path tortuosity is a consequence of both intergranular fracture and transgranular fracture through interfaces of maximum shear. The co-operative interplay of crack path tortuosity and plasticity promoted by the transgranular crack propagation results in the highest fracture toughness values. As the grain plasticity

level decreases, intergranular fracture dominates over transgranular fracture. Even though intergranular fracture results in a tortuous crack path, the overall fracture toughness decreases due to the suppression of plastic dissipation caused by a lower fraction of transgranular crack propagation. At the lowest value of grain plasticity, again, intergranular and transgranular fracture contribute nearly equally to the overall crack path. However, the crack primarily propagates in a mode-I fashion, resulting in the toughening effect of crack path tortuosity and plasticity both negligible. In the absence of both toughening mechanisms, the fracture toughness is the lowest. For $Q = 2$, Figure 5.5(f) shows that intergranular crack propagation prevails at all levels of grain plasticity. Even at the highest level of plasticity, plastic dissipation is extremely low because the crack tends to propagate through weaker GBs. High crack path tortuosity results are seen in cases in which intergranular fracture dominates. This is partly due to the fact that a homogeneous grain constitutive model is used. This again leads to the highest fracture toughness. As grain plasticity decreases below a certain point $\left(\sigma_y/\sigma_{y0} \geq 1.4\right)$, plastic dissipation becomes essentially negligible, and crack path tortuosity is the only remaining toughening mechanism. As a result, the fracture toughness values remain almost the same, independent of grain plasticity.

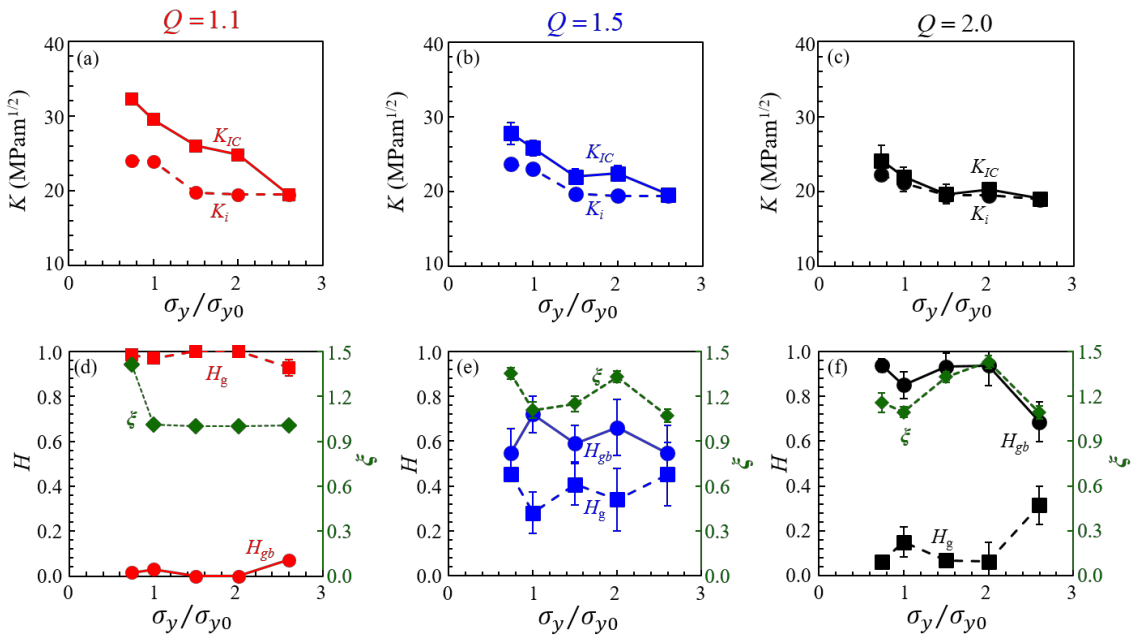

Figure 5.5: (a)-(c) variations of K_i and K_{IC} and (d)-(f) variations of the crack length fractions and crack path tortuosity with normalized grain yield strength at different levels of the ratio between maximum and minimum GB strengths. The SEMSS with ~95 μm grain size is used.

5.2.3 Competition between surface energy release and plastic dissipation

The same sets of simulations carried out using different grain yield strength levels and different GB strength profiles are considered here to delineate the competition between plastic dissipation and surface energy release rate. Again, the SEMSS has a grain size of with ~95 μm. Figure 5.6 shows the relative contributions of plastic dissipation and surface energy release rate to J_i and J_{IC}. The error bars denote statistical variations among samples in the SEMSS. At the onset of crack propagation, surface energy release accounts more for the initiation fracture resistance than plasticity at all levels of GB strength. For $Q = 1.1$,

plasticity contributes more than the surface creation to the steady state fracture resistance for $\sigma_y/\sigma_{y0} \leq 1.35$. As the grain plasticity decreases, surface energy tends to dominate the fracture behavior, resulting in lower overall fracture toughness. For $Q = 1.5$, surface energy always contributes more than plasticity to the overall fracture toughness. The fracture toughness is the highest when the contributions from surface creation and plasticity are balanced. For $Q = 2$, plastic dissipation has a significant effect only at low yield stress levels, as for $\sigma_y/\sigma_{y0} \geq 1.5$ the fracture toughness is completely determined by surface energy dissipation. For the toughening effect of plasticity to be more pronounced, the mismatch between grain and GB fracture strengths should be low. As the surface energy along the GBs decreases, the crack preferentially goes through the GBs, suppressing plastic dissipation even when the grain yield stress is low. At lower levels of plasticity (higher grain yield stress), the surface energy term dominates and the fracture toughness ceases to depend on the grain yield strength.

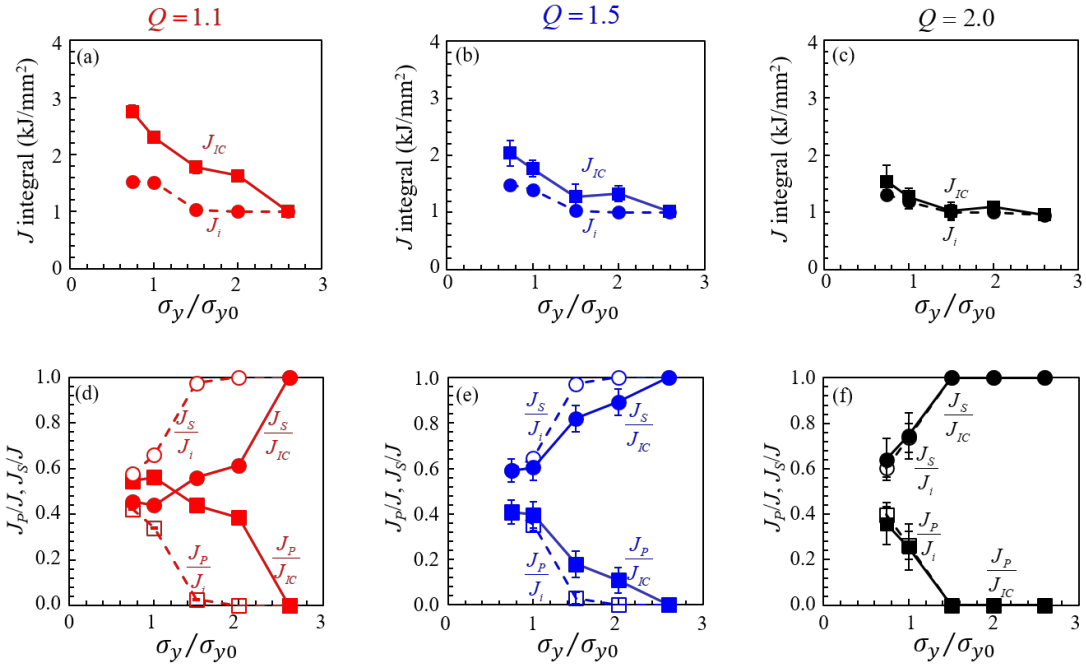

Figure 5.6: (a) – (c) J_i and J_{IC}, and (d) – (f) relative contributions of plasticity and surface energy release rate to the fracture resistance for different levels of normalized grain yield strength. The SEMSS of ~95 μm grain size is used.

5.2.4 Effect of microstructural attributes on fracture

To establish relations between the macroscale fracture behavior and microstructure, four SEMSS with different levels of mean intercept grain size are considered. For each SEMSS, three GB strength profiles are used. The grain yield strength is kept the same at 385 MPa for all cases. Figure 5.7(a)-(d) show the crack paths in one representative microstructure from each of the four SEMSS. Figure 5.8 shows K_i, K_{IC}, J_i, J_{IC}, relative contributions of plastic dissipation and surface energy release in terms of J_s/J_{IC}, J_p/J_{IC}, and the crack path descriptors H and ξ, all as functions of the grain size. Over the range

analyzed, grain size and GB density do not have a significant influence on the fracture initiation resistance J_i and K_i. However, these attributes indeed have a significant influence on the steady state fracture toughness measures K_{IC} and J_{IC}. The fracture toughness is the highest when the grain size is 50-70 μm. At the finest grain size (~25 μm), intergranular crack propagation dominates, resulting in the highest crack path tortuosity. Consequently, plastic dissipation is suppressed and crack meandering is the only toughening mechanism. The corresponding fracture toughness is approximately 20% below the highest level seen for a grain size of ~70 μm. As the grain size increases to ~50-70 μm, transgranular fracture occurs in higher proportions. As a result, both plastic dissipation and crack path tortuosity act as toughening mechanism. A tortuous crack path arises not only due to the intergranular fracture, but also due to transgranular fracture along directions of maximum shear. Therefore, the material shows higher fracture toughness values. The contributions of surface energy and plasticity are nearly the same towards the overall energy dissipation for these intermediate levels of grain size. As the grains become even coarser (~ 100 μm), transgranular crack propagation begins to dominate and intergranular fracture is almost negligible. Transgranular fracture occurs primarily through mode-I direction and hence the crack path tortuosity is also insignificant. In this extreme case, plasticity is the only toughening mechanism and therefore, the material exhibits a slightly reduced fracture toughness value.

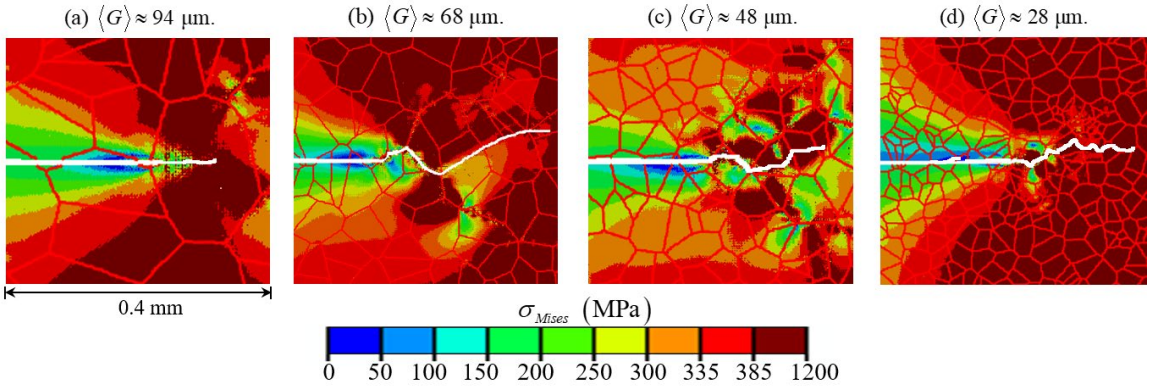

Figure 5.7: Crack propagation at different grain sizes. One sample from each of the four SEMSS with different grain sizes is used. The grain yield strength is 385 MPa, and the GB strength profile correspond to $Q = 1.5$.

The grain size dependence of ductile fracture toughness varies from one material to the other. Some studies exist that attempt to capture a specific trend between the grain size and the fracture toughness [51, 102, 103]. Experimental studies on different material systems show that three types of trend could be found. (1) K_{IC} increases with decreasing grain size as is observed in Ti, Al based alloys, (2) K_{IC} is barely dependent on grain size like in α-Fe, and (3) K_{IC} decreases with decreasing grain size as exhibited by Cu-Zn, Cu-Ni, and NiTi alloys. Molkeri et al. [51] showed that fracture resistance of ductile material decreases with decreasing mean grain size. In our case K_{IC} first increases slightly with decreasing grain size and then decreases with decreasing grain size. The trend depends upon the relative contributions of plasticity and new surface creation to the overall fracture resistance. In this case, the contribution of plasticity associated with transgranular crack propagation in the coarse grained microstructure wins over the contribution of crack path

tortuosity associated primarily with intergranular crack propagation in the fine grained microstructure.

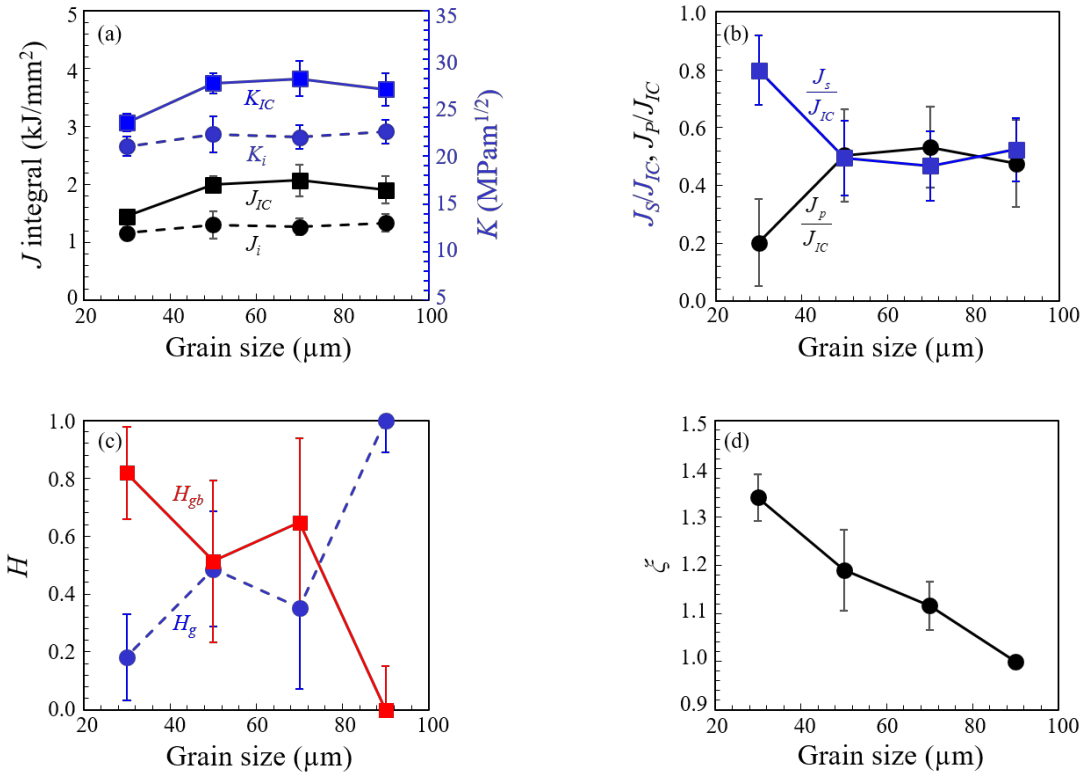

Figure 5.8: (a) The fracture toughness measures, (b) relative contribution of plasticity and surface energy to fracture resistance, (c) the crack propagation mechanisms in terms of the crack path fractions, and (d) the crack path tortuosity, as function of the mean intercept grain sizes. The grain yield strength is 385 MPa, and the GB strength profile correspond to $Q = 1.5$ in all cases.

The interplay between transgranular and intergranular crack growth with constituent plasticity via crack path tortuosity explains the observation that fracture toughness is the highest at coarser grain sizes in the 50-70 μm range. As the grain size decreases, the mean free path for transgranular crack propagation decreases and the

probability of intergranular crack propagation increases. Therefore, for a microstructure with fine grains (~30 μm), intergranular crack propagation dominates, causing an overall reduction in fracture resistance. For microstructures with 70-90 μm grains, comparable amounts of transgranular and intergranular crack propagation takes place. The higher mean free paths for transgranular crack propagation also contribute to maintaining constituent plastic dissipation.

5.2.5 Stochasticity in fracture

Variations at the microstructure level result in considerable scatter in fracture toughness values and is a primary source of material behavior stochasticity at the macroscopic scale. An analysis is carried out using the results for $\sigma_y = 385$ MPa, $Q = 1.5$, and the four SEMSS. Each set consists of 20 statistically similar samples. The two-parameter Weibull distribution function is used to quantify the probability of observing a particular fracture toughness value

$$P\left(K = K_{IC}\right) = 1 - \exp\left[-\left(\frac{K_{IC}}{K_0}\right)^{m_f}\right], \tag{5.1}$$

where, K_0 and m_f represent the normalization factor and the shape factor, respectively. The normalization factor (K_0) can also be interpreted as the value of fracture toughness with a 63% probability. It can be used as a characteristic fracture toughness value. Figure 5.9 shows the probability distribution for three grain sizes. The result for the 48 μm grain size is not shown for graphical clarity since it is very close to the results for the 95 and 68 μm

grain sizes. The distribution is the widest for the smallest grain size which has the highest density of weaker GBs. Since all bulk and interfacial properties are taken as deterministic here, the stochastic variations are fully attributable to the microstructural variations.

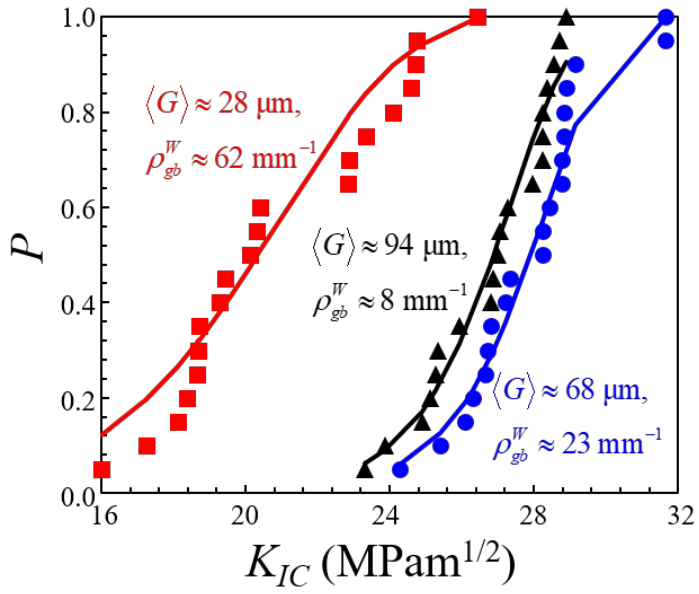

Figure 5.9: Cumulative probability of fracture as function of fracture toughness. The symbols represent calculated results and the lines represent fits to the Weibull distribution. The grain yield strength is 385 MPa and GB strength profile corresponds to $Q = 1.5$.

To relate the stochasticity in fracture toughness to GB behavior, the probability distribution of fracture toughness at three values of Q are shown in Figure 5.10. The lines are fits to eq.(5.1). The SEMSS with the ~95 μm grain size is used along with a yield strength of 385 MPa. Scatter is lowest at $Q = 1.1$ and increases as Q increases, suggesting that GB strength variations is a significant source of the stochasticity in fracture behavior.

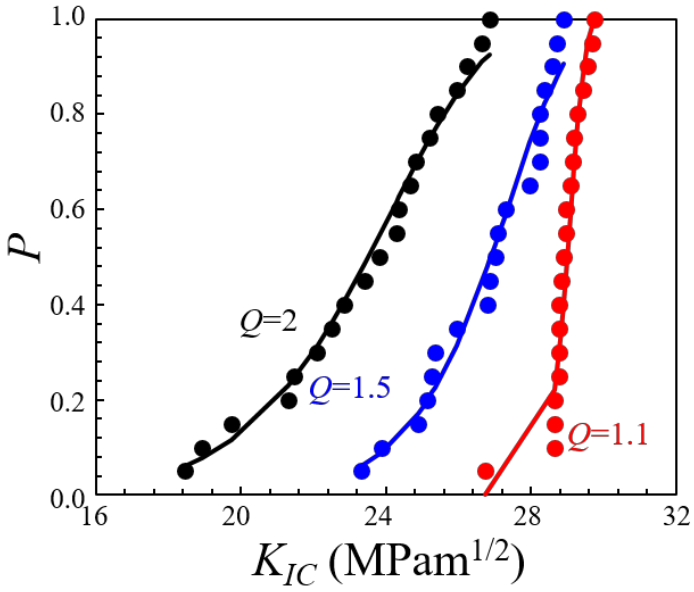

Figure 5.10: Cumulative probability of fracture as function of fracture toughness for three different GB strength profiles. The symbols represent calculated results and the lines represent fits to the Weibull distribution. The grain yield strength is 385 MPa and the SEMSS with ~95 μm grain size is used.

5.2.6 Characterization of fracture toughness

To delineate the trend of fracture toughness variation with microstructural attributes and GB behavior, contributions of grain boundary energy and plasticity are assessed as functions of the grain size and the GB strength profiles. To this end, the grain size and the grain boundary strength profiles are varied while the grain yield strength is kept at 385 MPa. The grain size and the GB strength profiles directly influence the fracture mechanisms. H_{gb} increases as Q increases (i.e., as overall GB strength decreases) and as the mean intercept grain size decreases. The combined effects of Q and $\langle G \rangle$ can be characterized by

$$H_{gb} = 1 - \exp\left[-\frac{D(Q-1)}{\sqrt{\langle G \rangle}}\right], \tag{5.2}$$

where, $\langle G \rangle$ is in μm, and D is a fitting parameter in μm. D = 18.34 μm when the grain yield strength is at 385 MPa. It is to be noted that the lowest value possible for Q is 1 which corresponds to uniform boundary strength. Figure 5.11 shows the trend revealed by calculations. The form of the equation satisfies the limiting conditions, i.e., (a) when Q = 1, the material is homogeneous without microstructure (as the highest GB strength is the same as the fracture strength inside the grains), and hence H_{gb} = 0; (b) when $\langle G \rangle$ tends to 0, the microstructure has extremely fine grains with negligible mean free path for transgranular fracture, and hence H_{gb} = 1.

The surface part of the energy release rate J_S can be evaluated using eqs. (5.2) and (4.11) for each crack path (each sample) as a function of grain size and GB strength profile. For each material case (each SEMSS), the mean value of J_S can be expressed as a function of the mean crack path tortuosity $\left(\bar{\xi}\right)$ and the mean GB energy $\left(\bar{\Phi}_{gb}\right)$, i.e.,

$$\bar{J}_S = \bar{\xi}\left[\bar{\Phi}_{gb} + \left(\Phi_g - \bar{\Phi}_{gb}\right)\exp\left\{-\frac{D(Q-1)}{\sqrt{\langle G \rangle}}\right\}\right], \tag{5.3}$$

where, Φ_g, Φ_{gb}, and J_S are in kJ/mm^2. As expected, when Q = 1, $\bar{J}_S = \bar{\xi}\Phi_g = \bar{J}_S^g$, which is the surface part of the energy release rate for a uniform material without microstructure. On

the other hand, when $\langle G \rangle \to 0,\ H_{gb} \to 1,$ and $\bar{J}_S \to \bar{\xi}\bar{\Phi}_{gb} \to \bar{J}_S^{gb},$ which is the average surface energy release rate due to GBs only.

To assess the plastic part of the energy release rate, J_P is plotted as a function of the transgranular crack path ratio in Figure 5.12. The relation can be described by

$$J_P = J_P^g \sqrt{H_g} = J_P^g \sqrt{1 - H_{gb}}, \tag{5.4}$$

where, J_P^g is the plastic part of the energy release rate for a homogeneous material without GB and is measured in kJ/mm^2. When $H_g = 1$, the material is homogeneous, $H_{gb} = 0$, and $J_P = J_P^g$. $J_P^g = 1.34$ kJ/mm^2 at the grain yield strength of 385 MPa. For each material case (SEMSS), eqs (5.2) and (5.4) allow the mean value of J_P to be obtained as a function of grain size and GB strength profile as

$$\bar{J}_P = J_P^g \exp\left\{-\frac{D(Q-1)}{2\sqrt{\langle G \rangle}}\right\}. \tag{5.5}$$

Finally, the mean value for J_{IC} can be obtained as a function of the mean grain size and the GB strength profile by combining eqs. (5.3) and (5.5). The relation is given by

$$\bar{J}_{IC} = \bar{J}_S^{gb} + \left(\bar{J}_S^g - \bar{J}_S^{gb}\right)\exp\left[-\frac{D(Q-1)}{\sqrt{\langle G \rangle}}\right] + J_P^g \exp\left[-\frac{D(Q-1)}{2\sqrt{\langle G \rangle}}\right]. \tag{5.6}$$

Again as expected, when $Q = 1$, $\bar{J}_{IC} = \bar{J}_S^g + J_P^g$; and when $\langle G \rangle \to 0$, $\bar{J}_{IC} \to \bar{J}_S^{gb}$, the contribution from plasticity becomes negligible. Figure 5.13 compares the mean J_{IC} value calculated from eq. (5.6) (dash line), with numerical results over a range of values of the characteristic microstructure parameter $D(Q-1)/\sqrt{\langle G \rangle}$. The trend and values are in good overall agreement with each other. This equation captures the overall trend of J_{IC} decreasing with increasing Q and decreasing <G>. The relation also shows that the influence of microstructural heterogeneities is more on the surface part of the energy release rate than on the plastic part. Surface energy dominates at higher values of Q (weaker and more inhomogeneous GBs), as well as finer grain sizes.

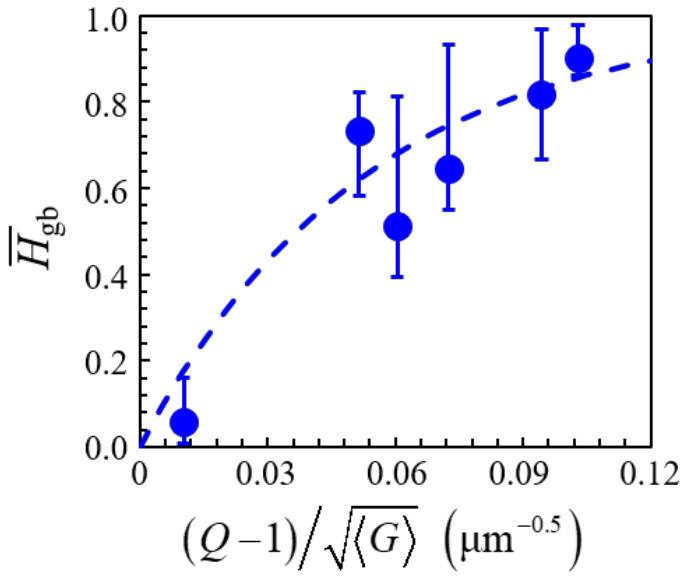

Figure 5.11: Fraction of intergranular crack length as a function of the microstructure characterized by the parameter $(Q-1)/\sqrt{\langle G \rangle}$ in $\mu m^{-0.5}$. The dash line represents fit to eq. (5.2). The grain yield strength is 385 MPa in all cases.

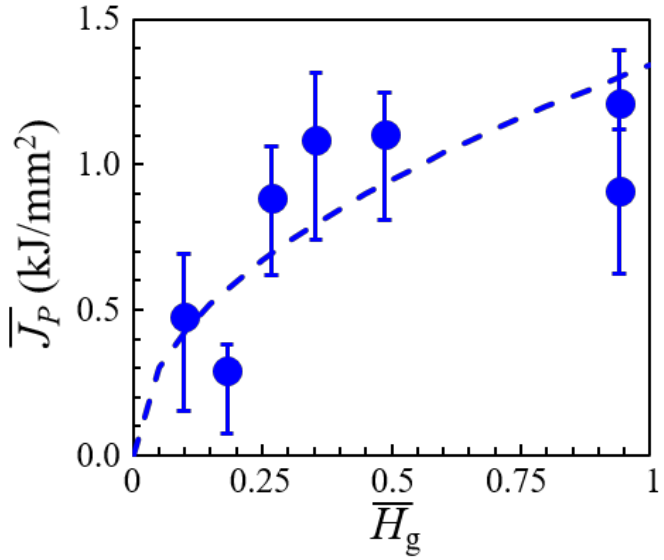

Figure 5.12: Mean plastic part of the energy release rate as a function of the transgranular crack path ratio. The dash line represents fit to eq. (5.4). The grain yield strength is 385 MPa.

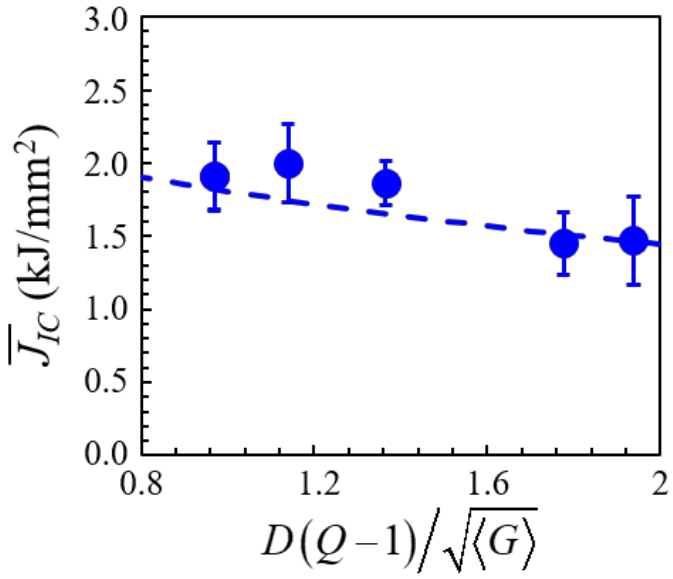

Figure 5.13: $\overline{J}_{IC}$ as a function of microstructure as characterized by the dimensionless parameter $D(Q-1)/\sqrt{\langle G \rangle}$. The dash line represents the mean relation in eq. (5.6). The grain yield strength is 385 MPa.

5.3 Summary

Thus, analyzing the effect of GB characters provides important insights. The transgranular fracture is identified to be one primary toughening mechanism in ductile materials. Unlike the brittle materials, intergranular fracture acts as a less effective toughening mechanism and almost always leads to embrittlement in a ductile microstructure. The overall fracture resistance increases with increasing grain size which can be attributed to the increasing mean free path for transgranular crack propagation and an enhanced contribution of associated plasticity. The overall fracture resistance becomes independent of the constituent plasticity if the microstructure contains a well-connected network of weak GBs. In that case, even the lowest level of yield stress would not have an effect since the crack propagates almost entirely through the brittle GBs. The results obtained from the numerical simulations are in good agreement with the experimentally obtained fracture toughness values. Also, the fracture mechanisms match with that observed from fractographic analyses. Moreover, the trend in variation of fracture toughness with grain size are in good agreement with the experimentally and computationally observed trends reported earlier. Therefore, our computational framework not only provides important insights regarding structure-property relations at different length scales, it also produces reliable results close to real material behavior.

6 EFFECT OF GRAIN ORIENTATION ON FRACTURE

6.1 Introduction

In this chapter, the capability of the previously reported computational framework is extended to model the anisotropic deformation of grains using a crystalline plasticity formulation. The model explicitly tracks crack propagation through the polycrystalline microstructure with random and preferred grain orientations and accounts for GB misorientation. The effects of grain orientation on competition between transgranular and intergranular ductile fracture is systematically studied. The analyses carried out focus on characterizing the overall fracture resistance in terms of K_{IC}, J_{IC} as function of microstructural attributes that include grain size, grain orientation, GB misorientation, GB density etc. Multiple statistically equivalent microstructure sample sets (SEMSS) are used to assess the stochasticity in the macroscopic fracture toughness due to microstructural heterogeneity variations. Further analyses of the results from this computational framework facilitate developing empirical models that establish fracture toughness as function of microstructural attributes. Although the material of focus here is Mo, the framework and the model can be used for other materials as well.

Section 6.2 mentions the computational settings used for this analysis. Section 6.3 describes the effect of texture on overall fracture resistance. Section 6.4 analyzes the influence of texture in terms of grain size distribution, misorientation angle dependent GB density, and the primary slip system density. Section 6.5 finally establishes the structure-property relation in terms of mathematical equations.

6.2 Numerical simulations

In order to understand the effects of grain orientation, simulations are performed on five SEMSS with different fractions of textured grains (TG) in the range 0% - 100%. Crystalline plasticity formulation is used to account for the anisotropy of the grains. Misorientation dependent GB interfacial law is assumed like all other previous cases. The homogenized region beyond the microstructure assumes a simple bi-linear elastic-plastic law as described in chapter 3. The results of the microstructure based CFEM calculations, the subsequent fracture toughness characterization, and analyses are discussed in this section. All samples in the SEMSS are subjected to the same loading. Systematic comparisons of the fracture trends and the mechanisms are made in terms of K_{IC}, J_{IC}, H, and ξ.

6.3 Effect of texture on overall fracture resistance

To delineate the effect of grain orientation, five sets of simulations are performed using microstructures with five different fractions of textured grains (TG). Figure 6.1 shows the crack growth resistance curves for five representative microstructures from each SEMSS with different fractions of TG. The fracture resistance at the initiation of crack growth is defined as the initiation fracture resistance J_i. The crack initiation resistance is significantly higher in the SEMSS with 100% TG compared to all other cases. The fracture resistance when crack growth attains a steady state is defined as the J_{IC}. The rise of the crack growth resistance curve before it reaches steady state increases with increasing fraction of the TG. In particular, the rise of the crack growth resistance curve is

significantly high for the SEMSS with 30-70% TG. The crack growth resistance reaches the steady state at a higher level of crack extension compared to the two extreme cases of 100% and 0% TG.

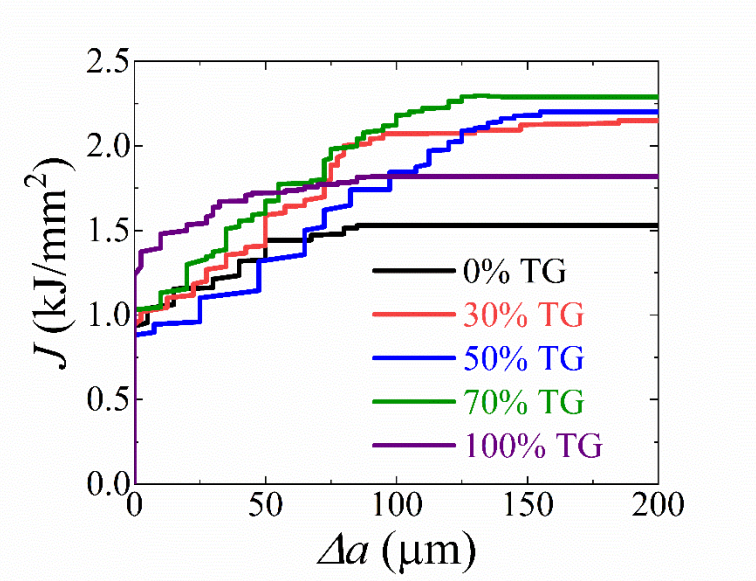

Figure 6.1: The crack growth resistance curves for five proportions of textured grains in the microstructure.

Figure 6.2 exhibits the initiation and steady state fracture resistance in terms of J_i, K_i, J_{IC}, and K_{IC} as a function of the fraction of TG. The error bars denote statistical variations among samples in the SEMSS. The initiation fracture toughness does not vary much with increasing fraction of the TG, however, the K_i is considerably high for the SEMSS with 100% TG. On the other hand, there is an overall increase in the K_{IC} with increasing fraction of the TG.

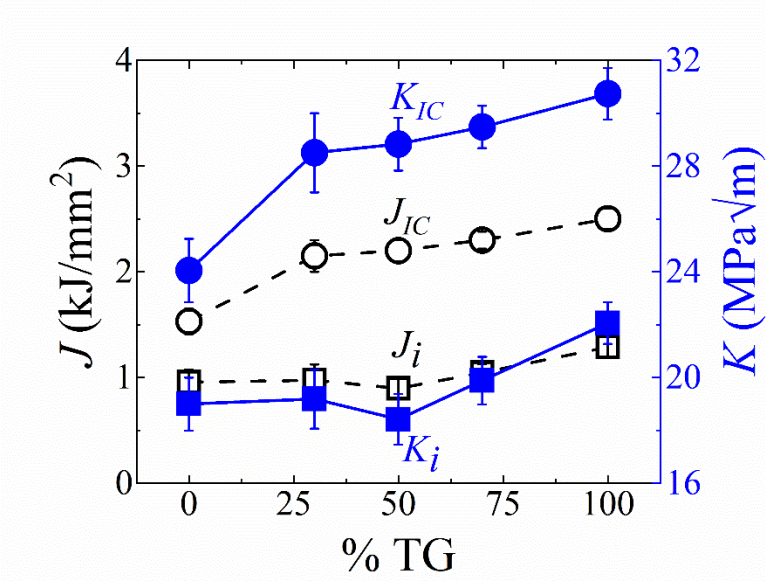

Figure 6.2: Fracture resistance in terms of J_i, J_{IC}, K_i, and K_{IC} as a function of the proportion of textured grains in the microstructure.

Figure 6.3 depicts crack propagation in representative microstructures from each of the five SEMSS. In the SEMSS with 0% TG, crack almost always prefers to propagate through the GBs. In case of the SEMSS with 30% TG, intergranular crack growth changes its course to transgranular as the crack encounters a considerably long mean free path for fracture through the grains of {011}<100> texture. As the fraction of TG further increases (50% - 70%) in the microstructure the crack cuts through the grains of both random texture and {011}<100> texture. In the SEMSS with 100% TG, the crack cuts through the grains with {011}<100> texture. However, it does not penetrate through the grains of {001}<110> texture. It passes through the boundaries between these two differently textured grains. Overall, the preference for transgranular cracking increases with increasing

fraction of the TG. The fracture mechanisms in terms of the crack path ratio and crack path tortuosity are quantified in Figure 6.4. The fraction of intergranular crack path decreases with increasing fraction of the TG. The crack path tortuosity follows the same trend as that of the intergranular crack path ratio. The tortuosity caused by the intergranular fracture decreases with increasing fraction of the TG. This observation is consistent with the trend shown by the overall fracture toughness values. Figure 6.5 delineates the competition between plastic deformation and crack face generation in terms of their relative contributions to the overall fracture resistance. The relative contribution of new surface creation to the overall energy release rate decreases with increasing fraction of the TG. As expected, the relative contribution of plasticity increases with increasing fraction of the TG. The same trend holds both at crack initiation and at steady state crack propagation regime.

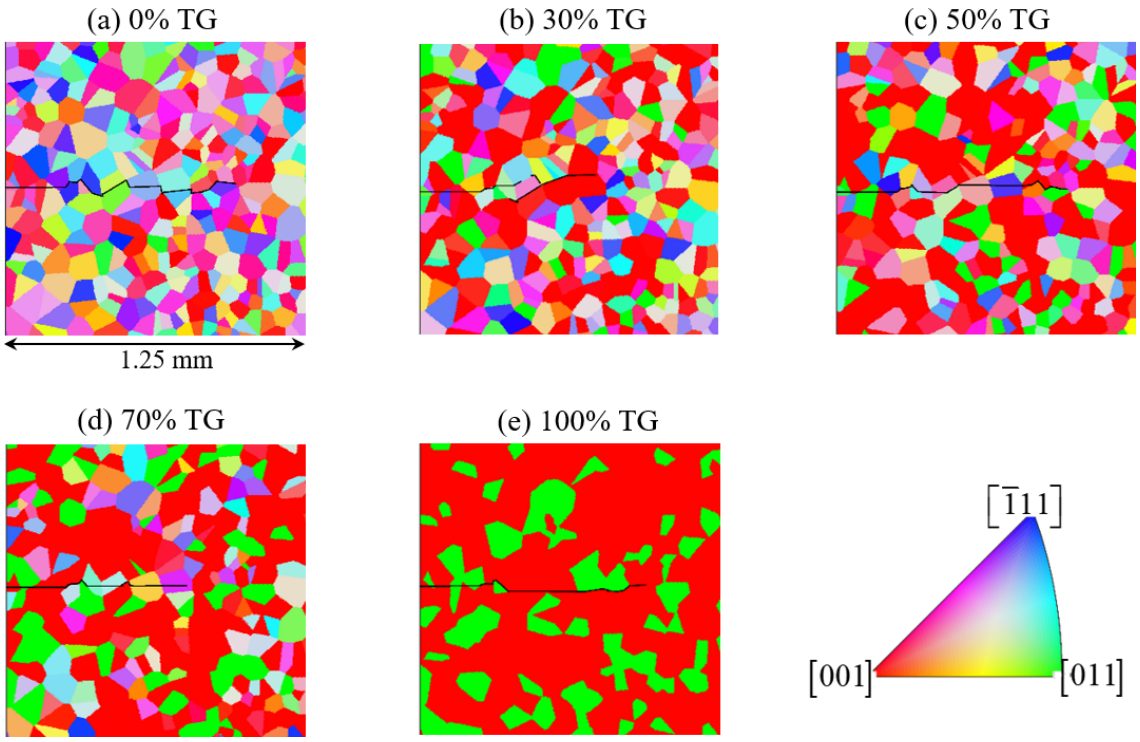

Figure 6.3: Crack propagation in representative microstructures from five SEMSS.

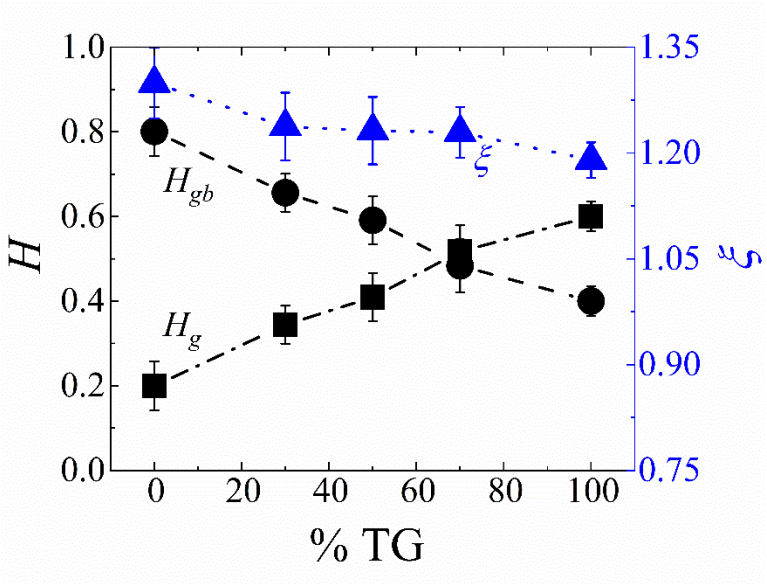

Figure 6.4: fractions of crack lengths inside grains and along grain boundaries, and the crack path tortuosity (ξ) over a range of proportions of textured grains.

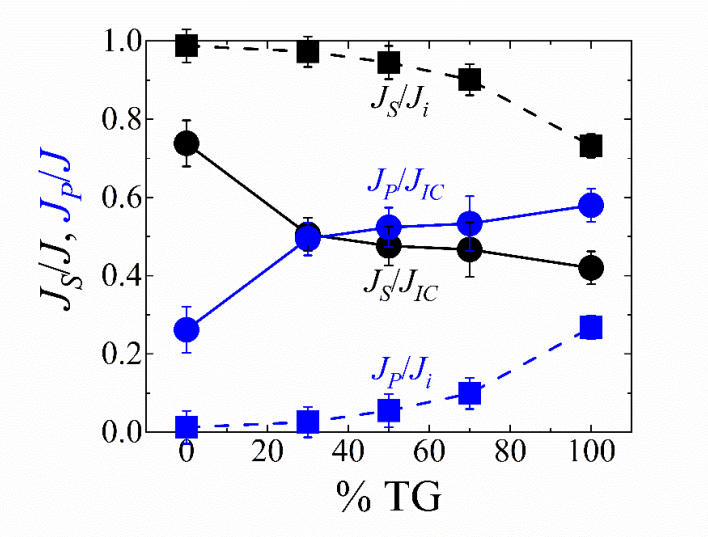

Figure 6.5: relative contributions of plasticity and surface energy release rate to the initiation and steady state fracture resistance for different proportions of textured grains.

6.4 Characterizing the influence of microstructural attributes

Texture influences microstructure in multiple ways. Variation in the fraction of TG leads to variation in (1) the effective grain size distribution, (2) the fraction of grains with favorably oriented primary slip systems (PSS), and (3) the GB characteristics. To understand the overall effect of texture on fracture in terms of the fracture toughness, competition between fracture mechanisms, and between plasticity and crack face creation, the effects of these three microstructural attributes are discussed separately.

6.4.1 Effect of grain size

The grain size controls the mean free path available for transgranular fracture and thus influences primarily the plasticity part of the overall fracture resistance as is evident from our prior work. As the fraction of TG increases, the maximum effective grain size increases although the mean grain size remains nearly the same. The SEMSS with 0% TG exhibits symmetric grain size distribution centered at ~70 µm. The SEMSS with 50-70% textured grains depicts randomly distributed islands of grains with ~70 µm mean intercept grain size embedded in relatively coarse matrix of TG. The mean intercept grain size of the coarser grains increases with increasing fraction of the TG. Figure 6.6 shows that the K_{IC} increases with increasing maximum value of the mean intercept grain size. This is attributed to the increasing contribution of plastic dissipation associated with increasing transgranular crack path ratio as shown in the figure.

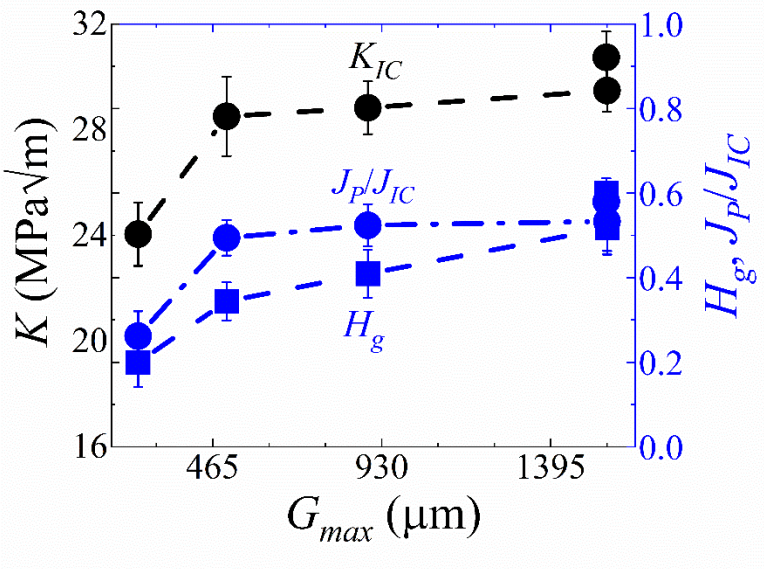

Figure 6.6: Fracture toughness in terms of K_{IC}, relative contribution of plasticity to J_{IC}, and the transgranular crack path ratio for different levels of maximum grain size.

6.4.2 Effect of favorably oriented primary slip systems

Favorably oriented PSS facilitates plastic deformation in grains. As the fraction of TG increases, the fraction of grains with favorably oriented PSS also increases. As reported in the literature [97] the critical resolved shear stress for slip is the lowest for $(\bar{1}01)[111]$ slip system followed by $(0\bar{1}\bar{1})[11\bar{1}]$, $(0\bar{1}1)[\bar{1}11]$, and $(101)[\bar{1}\bar{1}1]$. As the fraction of grains with these four PSS aligned with the specimen plane increases the plastic deformation resulting in an overall increase in the fracture resistance. As plastic deformation sets in at the crack tip very early in the loading process, crack initiation becomes more and more difficult with a higher fraction of PSS. In the SEMSS with 0% TG, the matrix phase has favorably oriented $(\bar{1}01)[111]$ slip system due to its Goss texture. The contribution of plasticity to crack initiation resistance becomes considerably high due to easier onset of plastic deformation through activation of slip. Once the crack initiates it tends to propagate through the matrix until it encounters a grain with a rotated copper component of texture. Activation of slip is rather difficult in grains with favorably oriented $(0\bar{1}1)[\bar{1}11]$ slip system compared to the grains with favorably oriented $(\bar{1}01)[111]$ slip system. Transgranular fracture prefers the latter type of grains and changes its course to intergranular when it encounters the first type. The grains with rotated cube type texture has favorably oriented $(0\bar{1}1)[\bar{1}11]$ slip systems and behave as harder grains in a softer matrix with Goss component of texture. This could be seen in Figure 6.3(e). Since the transgranular crack propagation through the grains of Goss texture results in significant plastic dissipation around the growing crack, the relative contribution of plasticity to steady state fracture resistance also increases with increasing fraction of the TG as shown in the Figure 6.7.

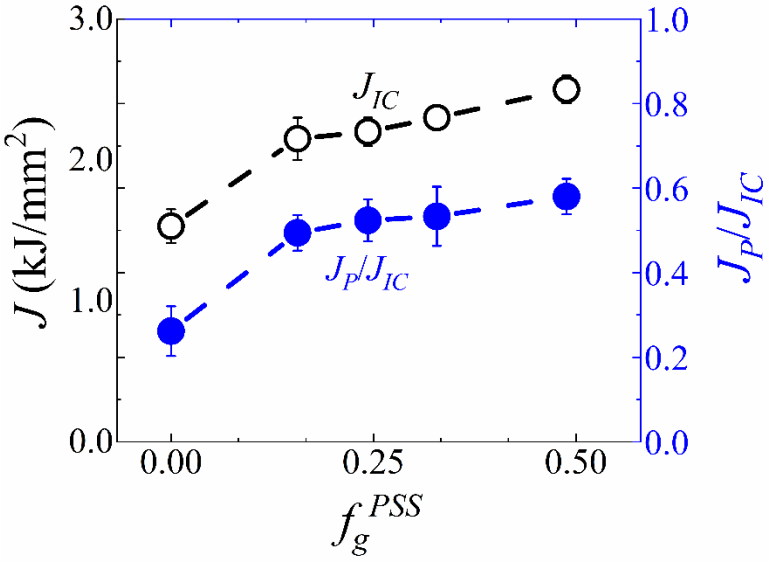

Figure 6.7: Fracture resistance in terms of J_{IC}, relative contribution of plasticity to J_{IC}, as a function of the fraction of grains with favorably oriented primary slip systems (PSS).

The assumption of single slip artificially renders the grains harder. A fully developed 3D model or assumption of multiple planar slip in a 2D framework is required to completely understand the correlation of cracking with different slip systems. However, this simplified model does a reasonable job in capturing the trend between fracture and primary slip.

6.4.3 Effect of GB characteristics

Again, for the sake of simplicity, GBs are characterized based on only their misorientation angle. No symmetry operation is performed and hence the misorientation angle ranges between 0˚ and 180˚. Our previous work shows that the overall fracture resistance increases with decreasing weaker GB density. In this case, the weaker GB

density decreases almost linearly with increasing fraction of the TG. As the weaker GB density increases, the crack tends to propagate more through the GBs resulting in an overall increase in the intergranular crack path ratio (Figure 6.8). That means the relative contribution of crack face generation to the overall fracture resistance is higher for the SEMSS with higher fraction of the randomly orientated grains. The crack path tortuosity also follows the same trend as that of the intergranular crack path ratio. The crack initiation almost entirely depends upon the energy contribution of the new surface creation for the SEMSS with 0% TG. On the other hand, contribution from plasticity wins over the contribution of new surface creation in case of the SEMSS with 100% TG.

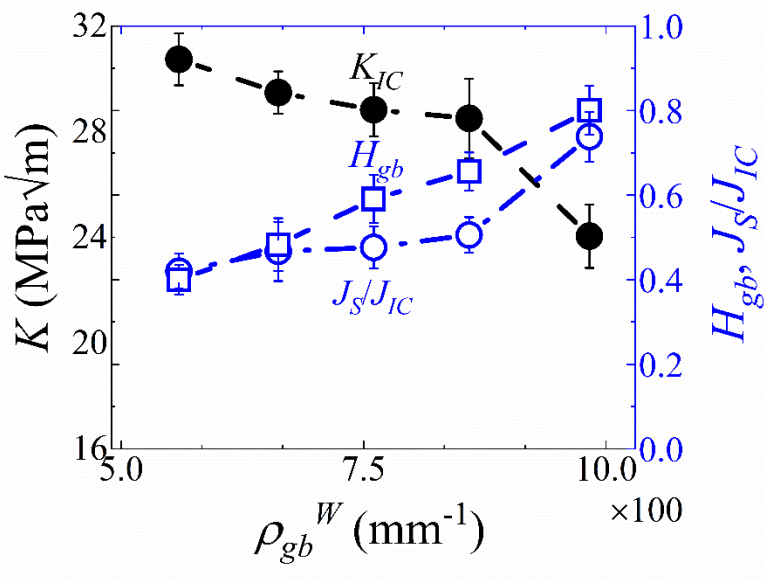

Figure 6.8: Fracture toughness in terms of K_{IC}, relative contribution of surface energy to J_{IC}, and the intergranular crack path ratio for different levels of weaker GB density.

6.5 Quantification of the correlation between fracture and microstructure attributes

To delineate the trend of fracture toughness variation with microstructural attributes, contributions of surface energy and plasticity are assessed as functions of the grain size, fraction of grains with favorably oriented PSS, and misorientation dependent weaker GB density. To quantify the microstructural attributes together, we define a microstructure descriptor *M* that takes into account the effective grain size distribution, fraction of PSS, grain boundary strength profile, and the misorientation dependent weaker grain boundary density. The microstructure descriptor *M* in mm^{-1} is defined as,

$$M = (Q-1)\,\rho_{gb}^{W}\left(\frac{1}{f_g^{PSS}}\right)\sqrt{\frac{\langle G\rangle}{G_{\max}}}, \tag{6.1}$$

where, ρ_{gb}^{W} is in mm^{-1}. The grain size distribution is characterized by the ratio of mean intercept grain size $(\langle G\rangle)$ to the maximum grain size $(G_{\max})$. This ratio signifies the skewness in the grain size distribution. The Q is kept constant at 1.5 for all calculations. Figure 6.9 depicts the *M* as a function of the grain size distribution descriptor and the ratio of weaker GB density to fraction of grains with favorably oriented PSS. The weaker GB density and the fraction of PSS has opposite effects on the overall fracture toughness. The $M = 0$ signifies a homogeneous material with no microstructural heterogeneities and $M \to \infty$ when the microstructure is full of weaker GBs and no significant fraction of grains with favorably oriented PSS exist.

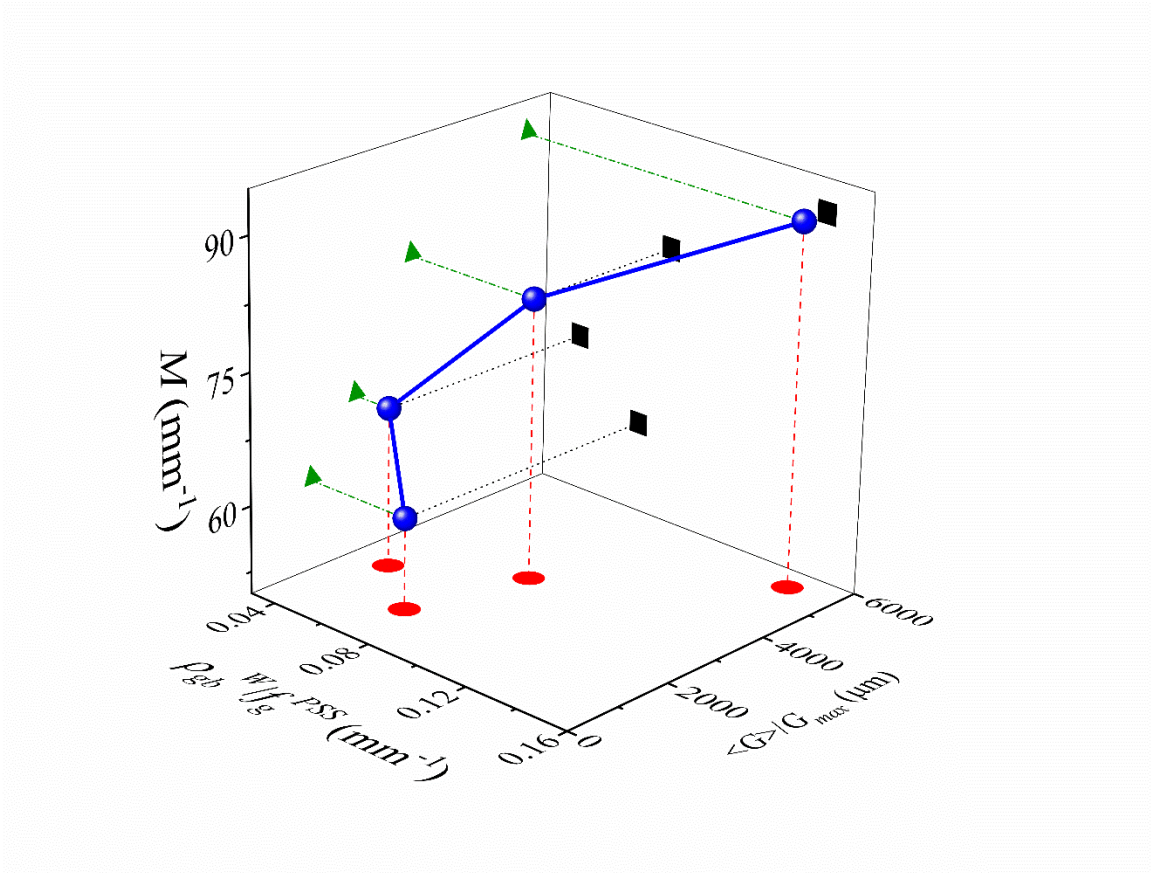

Figure 6.9: The microstructure descriptor (M) as a function of the grain size distribution descriptor and the ratio of weaker GB density to the fraction of grains with favorably oriented primary slip systems.

The M is defined in such a way that for each SEMSS the intergranular crack path ratio can be expressed as

$$H_{gb} = 1 - \exp\left[-\left(\frac{M}{M_0}\right)^m\right], \tag{6.2}$$

where M_0 is in mm^{-1}. The form of the equation satisfies the limiting conditions. As $\rho_{gb}^{W} \to \infty$, i.e., the microstructure is composed of only the weaker GBs, and/or $f_g^{PSS} \to 0$, i.e., none of the grains have favorably oriented PSS and hence fracture is completely governed by relative surface energy, $M \to \infty$, and the cracks always tend to propagate through the GBs, and thus $H_{gb} \to 1$. Also, as $G_{\max} \gg \langle G \rangle$, i.e., the grain size distribution is highly skewed, and/or $\rho_{gb}^{W} \to 0$, i.e., the material no longer contain microstructural heterogeneities $M \to 0$, the crack always tend to propagate through the grains and hence $H_{gb} \to 0$. The results from the five SEMSS are used to obtain the values of M_0 and *m*. For our material $M_0 = 753.47$ mm^{-1}, and $m = 0.3714$. Figure 6.10 compares the results from computational model and the fit to eq.(6.2).

The surface part of the energy release rate J_S can be evaluated using eqs. (4.11) and (6.2) as a function of the microstructure descriptor. For each material case (each SEMSS), the mean value of J_S can be expressed as a function of the mean crack path tortuosity $(\bar{\xi})$ and the mean GB energy $(\bar{\Phi}_{gb})$, i.e.,

$$\bar{J}_S = \bar{\xi}\left[\bar{\Phi}_{gb} + \left(\Phi_g - \bar{\Phi}_{gb}\right)\exp\left\{-\left(\frac{M}{M_0}\right)^m\right\}\right], \tag{6.3}$$

where, $\Phi_g, \bar{\Phi}_{gb}, \bar{J}_S$ are in kJ/mm^2. As expected, when $M = 0$, $\bar{J}_S = \bar{\xi}\Phi_g = \bar{J}_S^g$, which is the surface part of the energy release rate for a uniform material without microstructure. On

the other hand, when $M \to \infty,\ H_{gb} \to 1,$ and $\overline{J}_S \to \overline{\xi}\overline{\Phi}_{gb} \to \overline{J}_S^{gb},$ which is the average surface energy release rate due to GBs only.

To assess the plastic part of the energy release rate, J_P is plotted as a function of the transgranular path ratio in Figure 6.11. The relation can be described by

$$J_P = J_P^g \left(H_g\right)^n = J_P^g \left(1 - H_{gb}\right)^n, \tag{6.4}$$

where, J_P^g is the plastic part of the energy release rate for a homogeneous material without GB and is measured in kJ/mm^2. When $H_g = 1,$ the material is homogeneous, $H_{gb} = 0,$ and $J_P^g = 2.85$ kJ/mm^2 and $n = 1.13$ for this particular material. For each SEMSS, eqs. (6.2) and (6.4) allow the mean value of J_P to be obtained as a function of the microstructure descriptor as

$$\overline{J}_P = J_P^g \exp\left\{-\left(\frac{M}{M_0}\right)^{mn}\right\}. \tag{6.5}$$

Finally, the mean value for J_{IC} can be obtained as a function of the microstructure descriptor by combining eqs. (6.3) and (6.5). The relation is given by

$$\overline{J}_{IC} = \overline{J}_S^{gb} + \left(\overline{J}_S^g - \overline{J}_S^{gb}\right)\exp\left\{-\left(\frac{M}{M_0}\right)^{m}\right\} + J_P^g \exp\left\{-\left(\frac{M}{M_0}\right)^{mn}\right\}. \tag{6.6}$$

Again as expected, when $M = 0,\ \bar{J}_{IC} = \bar{J}_S^g + J_P^g;$ and when $M \to \infty, \bar{J}_{IC} \to \bar{J}_S^{gb},$ the contribution from plasticity becomes negligible. Figure 6.12 compares the semi-empirical model with the computationally obtained results. They match pretty well with each other. The trend and values are in good overall agreement with each other.

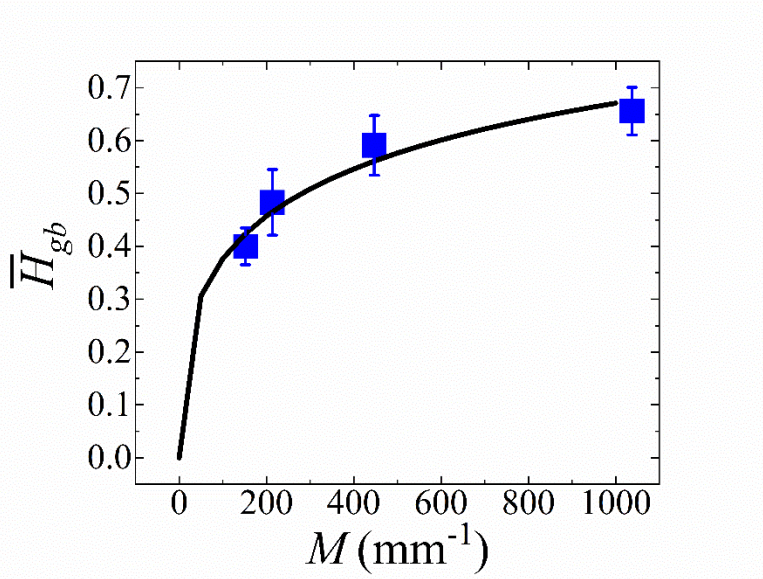

Figure 6.10: Mean intergranular crack path ratio as a function of the microstructure descriptor *M*. The black solid line shows eq. (6.2).

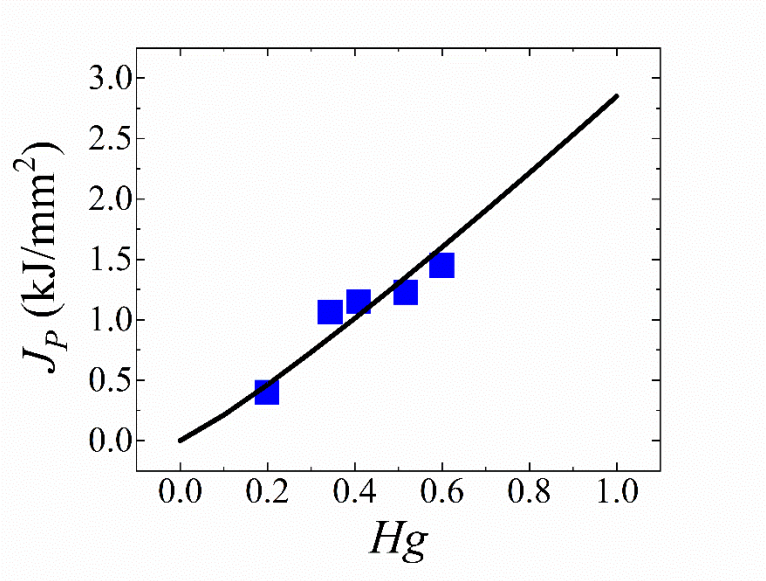

Figure 6.11: The contribution of plasticity as a function of the transgranular crack path ratio. The black solid line depicts the eq. (6.4).

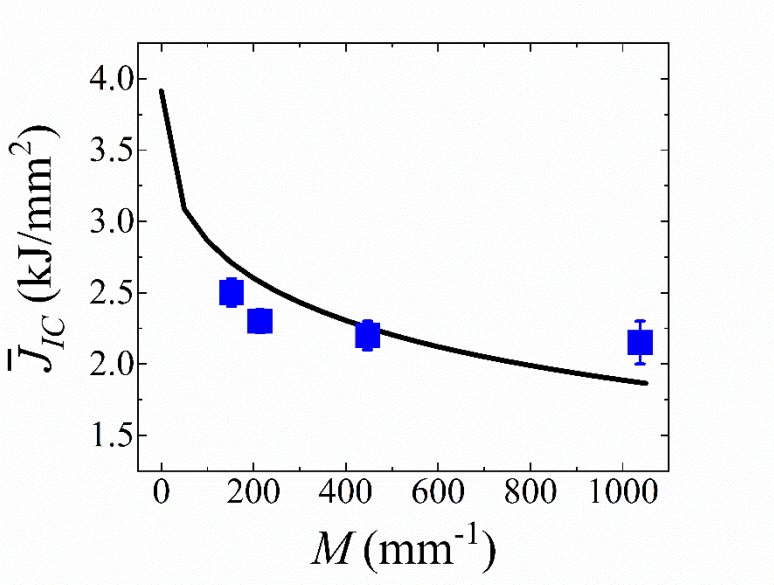

Figure 6.12: Mean fracture resistance as a function of the microstructure descriptor. The discrete data points are obtained from the computational model, and the solid line represents eq. (6.6).

6.6 Summary

The previously developed framework for capturing the interplay between grain boundary structure and constituent plasticity in ductile metals is extended to incorporate the effects of grain orientation. The framework is used to explore the fracture processes in microstructured metals and relate their fracture toughness to microstructure. The focus is on the effects of grain orientation, grain size, and misorientation dependent GB characteristics as microstructural attributes of interest.

The framework and analysis have yielded significant insights. The contributions include the development of a *J*-integral based method for predicting the fracture toughness, capturing the competition between transgranular and intergranular fracture, and quantification of the tradeoff between microstructure-induced crack tortuosity and constituent plasticity as a function of grain orientation. The overall fracture toughness increases with increasing fraction of textured grains in the microstructure. This is attributed to the three microstructural attributes that are primarily influenced by the proportion of textured grains and texture types. Increase in the fraction of the textured grains increases the skewness in the effective grain size distribution resulting in an increase in the mean free path for transgranular crack propagation. The type of texture controls the fraction of grains with favorably oriented primary slip systems and thus governs the plastic dissipation associated with the transgranular crack propagation. The type of texture and the fraction of textured grains also control the GB misorientation angle distribution and thus the weaker GB density.

7 COMPARISON BETWEEN 2D AND 2.5D MICROSTRUCTURE-SENSITIVE MODELING OF FRACTURE

7.1 Introduction

The microstructure sensitive modeling of fracture discussed so far was implemented in 2D. 2D approximations of microstructure-sensitive fracture works adequately well in terms of establishing the basic trends between fracture toughness and microstructure attributes, capturing the competition between transgranular and intergranular fracture in a polycrystalline microstructure. Even though 2D computations have certain advantages in terms of expenses it uses multiple assumptions for the sake of simplification. Because of these assumptions, the interactions between different mechanisms becomes more comprehensible. However, the 2D formulation cannot completely model the physics of plastic deformation and associated fracture mechanisms. As we tend to develop mathematical expressions to model fracture toughness as functions of microstructure attributes, the basic model should be able to consider the underlying physics of fracture in 3D. This chapter develops a 2.5D model and compares with the 2D model developed earlier.

In this chapter, section 7.2 describes development of a 2.5D computational framework. Section 7.3 compares 2D, and 2.5D models in terms of fracture toughness, fracture mechanisms as functions of microstructure attributes.

7.2 Microstructure sensitive 2.5D modeling of fracture

In order to capture the physics of plastic deformation and fracture in 3D, first a 2.5D formulation is developed. This formulation uses the 2D slices of 2.5D microstructures with the assumption of generalized plane strain. The details are described in the following subsections.

7.2.1 Computational configuration

In order to extend the current 2D model to 3D, first a generalized plane strain framework is developed. Again, a compact tension [104] type specimen is used to simulate the laboratory scale fracture toughness tests. The polycrystalline microstructure enters the design space at the crack tip of the pre-cracked CT specimen. Sub-sized specimens that follow all the specifications of ASTM standard [86] for the plane strain fracture toughness and *J*-integral measurement are considered. The overall dimensions of the 3D CT specimen are on the order of 6.12 mm × 6 mm × 2.5 mm as shown in the Figure 7.1. The microstructure region is 2.5 mm × 2.5 mm × 2.5 mm in dimensions and is inserted around the tip of the pre-crack of length 2.25 mm. CFEM and crystal plasticity are implemented only in the microstructure region. The microstructure region is stitched to the homogeneous part of the specimen using a mesh-tie constraint following Li and Zhou [23]. The size of the microstructure region is so chosen that the plastic zone is contained within the region. Mode-I loading is effected through an imposed displacement of 1 mm as indicated in the Figure 7.1. The edges of the specimen are traction-free and conditions of generalized plane strain are assumed to prevail. Because of the generalized plane strain formulation, the 3D

computational configuration effectively reduces to a 2.5D configuration as in Figure 7.2. The model uses 2D microstructures under generalized plane strain with 3D material models. Therefore, the overall computational configuration can be termed as 2.5D.

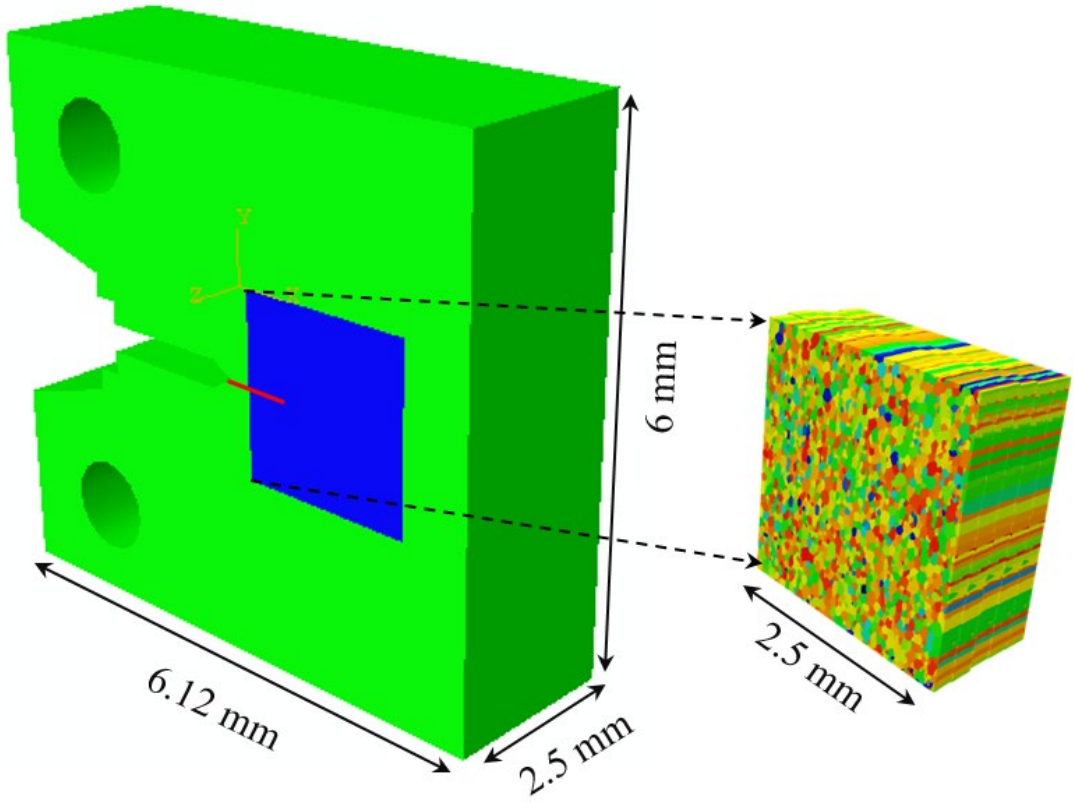

Figure 7.1: 3D CT specimen with a 3D microstructure region containing columnar grains around the crack tip.

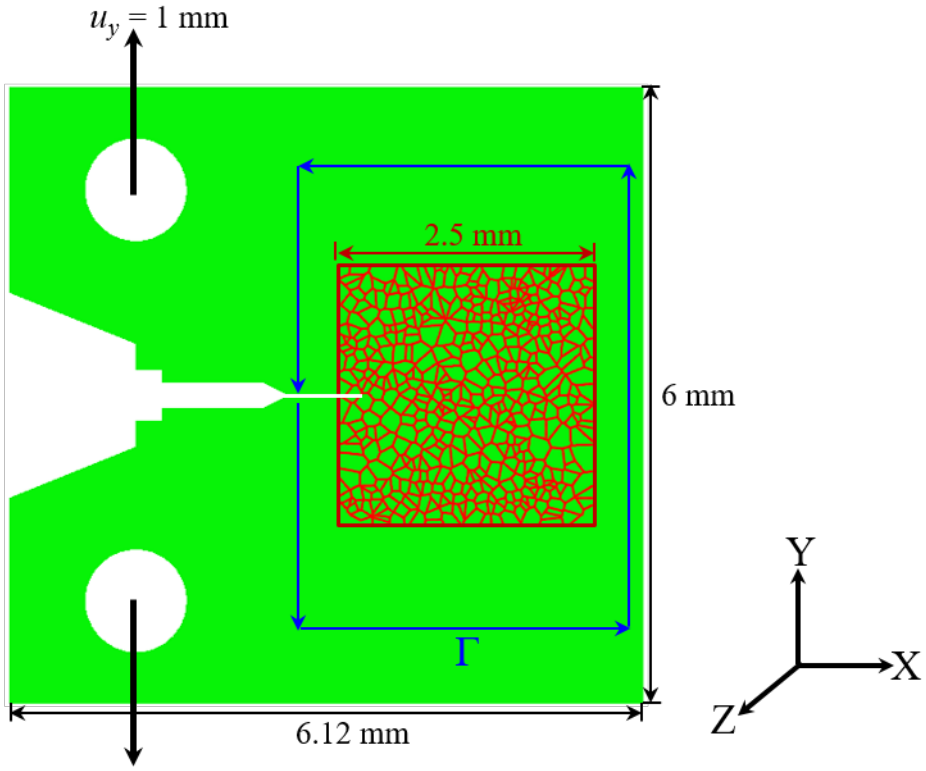

Figure 7.2: The 3D computational model reduced to 2.5D.

7.2.2 Material models

For the 2.5D model, a 3D crystalline plasticity formulation is adopted for the grains. The traction-separation law for the interfaces are also formulated in 3D. The homogeneous section outside the microstructure region still follows a simple bi-linear elastic-plastic constitutive law.

7.2.2.1 Crystal plasticity formulation for the grains

A full 3D crystal plasticity formulation is adopted for bcc Mo. A linear orthotropic elasticity is used for the grains. The multiplicative decomposition of the total deformation gradient is given by

$$\mathbf{F} = \mathbf{F}^e \cdot \mathbf{F}^p, \tag{7.1}$$

where $\mathbf{F}^e$ is the elastic deformation gradient representing the elastic stretch and rotation of lattice, and $\mathbf{F}^p$ is the plastic deformation gradient describing the collective effects of dislocation motion along the active slip planes relative to a fixed lattice in the reference configuration. Unit vectors $\boldsymbol{s}_0^\alpha$ and $\boldsymbol{n}_0^\alpha$ denote the slip direction and the slip plane normal direction, respectively for the α^{th} slip system in the undeformed configuration. The resolved shear stress on each slip system is related to the Cauchy stress tensor $\boldsymbol{\sigma}$ according to

$$\tau^\alpha = \boldsymbol{\sigma}:\left(\boldsymbol{s}^\alpha \otimes \boldsymbol{n}^\alpha\right), \tag{7.2}$$

where the slip vectors have been rotated into the current configuration. Under the application of the resolved shear stress, the shearing rates $\dot{\gamma}^\alpha$ on the slip systems are related to the plastic velocity gradient in the intermediate configuration according to

$$\mathbf{L}^p = \sum_{\alpha} \dot{\gamma}^{\alpha} \mathbf{s}_0^{\alpha} \otimes \mathbf{n}_0^{\alpha}, \tag{7.3}$$

with $\dot{\gamma}^{\alpha}$ ascribed to follow the rate-dependent flow rule as

$$\dot{\gamma}^{\alpha} = \dot{\gamma}_0 \left\langle \frac{\tau^{\alpha} - \chi^{\alpha}}{g^{\alpha}} \right\rangle^{m} \operatorname{sgn}\left(\tau^{\alpha} - \chi^{\alpha}\right), \tag{7.4}$$

where m is the inverse strain rate sensitivity exponent and g^{α} and χ^{α} are drag stress and back stress, respectively on the α^{th} slip system. These quantities evolve according to

$$\begin{cases} \dot{g}^{\alpha} = H \sum_{\beta=1} q^{\alpha\beta} \left|\dot{\gamma}^{\beta}\right|, \text{ and} \\ \dot{\chi}^{\alpha} = A_{kin} \dot{\gamma}^{\alpha} - A_{dyn} \chi^{\alpha} \left|\dot{\gamma}^{\alpha}\right|. \end{cases} \tag{7.5}$$

Here $q^{\alpha\beta}$ is the latent hardening coefficient, H, A_{kin} and A_{dyn} are the isotropic hardening, kinematic hardening and dynamic recovery coefficients, respectively. These non-linear coupled differential equations are solved using UMAT [95]. The parameters are given in Table 7.1.

For Mo with bcc crystal structure 24 slip systems of {110}<111> type are considered since the prior experimental works suggest that almost under all circumstances, activation of the {110}<112> type slip systems is rather rare [96-99]. Also, for bcc crystals, the dislocation core is distributed into multiple planes and that gives rise to twinning-anti-

twinning asymmetry in yielding. The criterion for yielding thus considers two shear stresses parallel and two shear stresses perpendicular to the slip direction, both resolved in two different {110} planes of the zone of the slip direction. For the [111] slip direction such a yield criterion is expressed as [97],

$$\sigma^{(\bar{1}01)} + a_1\sigma^{(\bar{1}01)} + a_2\tau^{(\bar{1}01)} + a_3\tau^{(\bar{1}01)} = \tau_{CRSS}, \tag{7.6}$$

where $\sigma^{\{110\}}$ and $\tau^{\{110\}}$ are the shear stresses parallel and perpendicular to the slip direction, respectively, in the corresponding {110} planes. The first term in the above equation is the Schmid stress and this drives the dislocation motion in the glide plane and does work through the glide. The last three terms are the non-Schmid stresses that affect the dislocation core but do not do any work when the dislocation glides. The values of the coefficients a_1, a_2, and a_3 are taken from[97].

The uniaxial effective stress strain response obtained from 3D crystal plasticity formulation matches very well with the experimentally obtained stress-strain curves. The 2D crystal plasticity model made the grains harder. Figure **7.3** compares the 2D vs 3D plasticity models and experimentally observed stress-strain curve.

Table 7.1: 3D crystal plasticity model parameters for bcc Mo

$\dot{\gamma}_0$	m	χ_0^{α}	A_{dyn}	A_{kin}	$q^{\alpha\beta}$
0.1	13	0	8	400	500

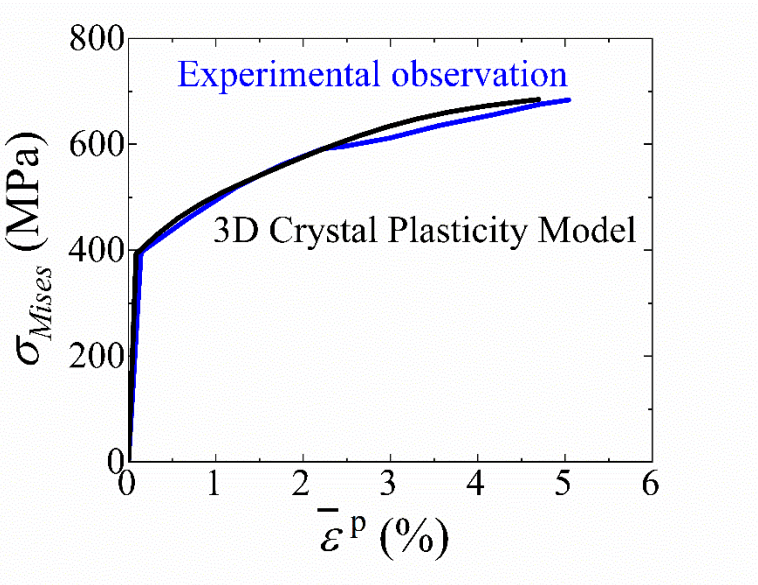

Figure 7.3: Stress-strain response using 3D crystal plasticity model compared with the experimental observation.

7.2.2.2 Traction-separation law for interfaces

In order to model arbitrary crack propagation through the grains and GBs, cohesive elements are inserted everywhere within the microstructure region. The cohesive elements follow a bilinear traction separation law implemented in ABAQUS. In this cohesive model, the traction applied on any cohesive surface (**T**) is work conjugate to the interfacial separation $(\boldsymbol{\delta})$. For zero thickness cohesive elements, the 3D uncoupled traction-separation constitutive relation can be written as,

$$\mathbf{T} = \begin{Bmatrix} T_n \\ T_s \\ T_t \end{Bmatrix} = \begin{bmatrix} K_{nn} & 0 & 0 \\ 0 & K_{ss} & 0 \\ 0 & 0 & K_{tt} \end{bmatrix} \begin{Bmatrix} \delta_n \\ \delta_s \\ \delta_t \end{Bmatrix}, \tag{7.7}$$

where $T_n = \mathbf{n} \cdot \mathbf{T}$, $T_s = \mathbf{s} \cdot \mathbf{T}$, $T_t = \mathrm{t} \cdot \mathbf{T}$, $\delta_n = \mathbf{n} \cdot \boldsymbol{\delta}$, $\delta_t = \mathbf{t} \cdot \boldsymbol{\delta}$, and $\delta_s = \mathbf{s} \cdot \boldsymbol{\delta}$ are the normal and two tangential components of $\mathbf{T}$ and $\boldsymbol{\delta}$, respectively, and $\mathbf{n}$, is the unit vector normal to the cohesive surface; $\mathbf{t}$ and $\mathbf{s}$ are the unit vectors tangential to the cohesive surface. $\boldsymbol{\kappa}$ represents the stiffness tensor connecting $\mathbf{T}$ and $\boldsymbol{\delta}$. δ_{nc}, δ_{tc}, and δ_{sc} are the critical normal and shear separations at which the cohesive strength vanishes and the cohesive element fails. Damage sets in when the following criterion is satisfied.

$$\left.\begin{aligned} &\left\{\left(\frac{T_n}{T_n^{\max}}\right)^2 + \left(\frac{T_s}{T_s^{\max}}\right)^2 + \left(\frac{T_t}{T_t^{\max}}\right)^2\right\} = 1, \\ &T_n^{\max} = T_s^{\max} = T_t^{\max} = T_{\max}. \end{aligned}\right\} \tag{7.8}$$

In our calculations, the maximum cohesive strength remains the same in all three directions and is denoted as $T_{\max}$. Damage evolves linearly and the material softens until the energy dissipated reaches the critical cohesive energy level denoted as Φ_0. A scalar damage variable D represents the overall damage behavior in the material, and the traction components are affected by the damage according to

$$\left.\begin{aligned} T_n &= (1-D)T_n', \quad T_n' \geq 0 \\ T_s &= (1-D)T_s', \\ T_t &= (1-D)T_t', \end{aligned}\right\} \tag{7.9}$$

where $\mathbf{T}'$ represents the traction components predicted by eq. (7.7) without considering damage. The limiting values of $D=0$ and $D=1$ correspond to zero separation and complete element degradation, respectively. Complete separation occurs when the resultant separation $\left(\delta_m=\sqrt{\delta_n^2+\delta_s^2+\delta_t^2}\right)$ reaches the critical value of separation $\left(\delta_m^c\right)$ such that

$$\frac{1}{2}\cdot T_{\max}\cdot\delta_m^c=\Phi_0. \tag{7.10}$$

The normalized traction τ and the normalized separation λ shown in the Figure 7.4(a) are defined as,

$$\left.\begin{aligned}\tau&=\frac{T}{T_{\max}}=\sqrt{\left(\frac{T_n}{T_n^{\max}}\right)^2+\left(\frac{T_s}{T_s^{\max}}\right)^2+\left(\frac{T_t}{T_t^{\max}}\right)^2},\\ \lambda&=\frac{\delta_m}{\delta_m^c}=\sqrt{\left(\frac{\delta_n}{\delta_{nc}}\right)^2+\left(\frac{\delta_s}{\delta_{sc}}\right)^2+\left(\frac{\delta_t}{\delta_{tc}}\right)^2},\\ \delta_{nc}&=\delta_{sc}=\delta_{tc}=\delta_m^c.\end{aligned}\right\} \tag{7.11}$$

The variable $\lambda_0=\delta_m^0/\delta_m^c$ denotes the normalized separation at which damage sets in and the traction reaches the maximum value. Hence the reciprocal of λ_0 represents the initial stiffness of the normalized traction-separation cohesive relation.

In order to incorporate the effect of GB characteristics on fracture, we invoke the theory of internal state variables and express the cohesive parameters as function of the GB misorientation angles. Different properties are assigned to the interfaces within the grains and along the GBs. Along the GBs, the cohesive energy of the interfaces vary with the GB misorientation angle (θ).

$$\left.\begin{aligned} \Phi &= \Phi\left(T_{\max}, \delta_m^c\right), \\ T_{\max} &= T_{\max}\left(\theta\right). \end{aligned}\right\} \tag{7.12}$$

According to the experimental observations reported in the literature [69], GBs with misorientation between 15˚-75˚ are more prone to fracture than the other boundaries. The variation of fracture strength with the GB misorientation angle as reported in [69] could be approximated by a sinusoidal function as formulated below.

$$\left.\begin{aligned} T_{GB}\left(\theta\right) &= C_1 + C_2 \cos\left(4\theta\right), \\ C_1 &= \frac{1}{2}\left(T_G + T_{GB}^{\min}\right), \\ C_2 &= \frac{1}{2}\left(T_G - T_{GB}^{\min}\right). \end{aligned}\right\} \tag{7.13}$$

T_G and $T_{GB}^{\min}$ represent the maximum and minimum values of the GB fracture strength $\left(T_{GB}\right)$, respectively. The maximum value of the GB fracture strength is the same as the interfacial strength within the grains $\left(T_{GB}^{\max} = T_G\right)$. Figure 7.4(b) shows profiles of the GB fracture strength for different values of $T_{GB}^{\min}$ while T_G is kept constant. These cases can be

distinguished by the ratio $Q = T_G / T_{GB}^{\min}$, which represents the degree of variation of $T_{GB}(\theta)$ as the GB misorientation angle changes. The values of the cohesive parameters used are shown in the Table 7.2. The maximum cohesive energy used in this model scales with the fracture toughness of pure Mo. The range of misorientation dependent variation of the GB fracture strength is obtained from the experimental observations reported in the literature [69].

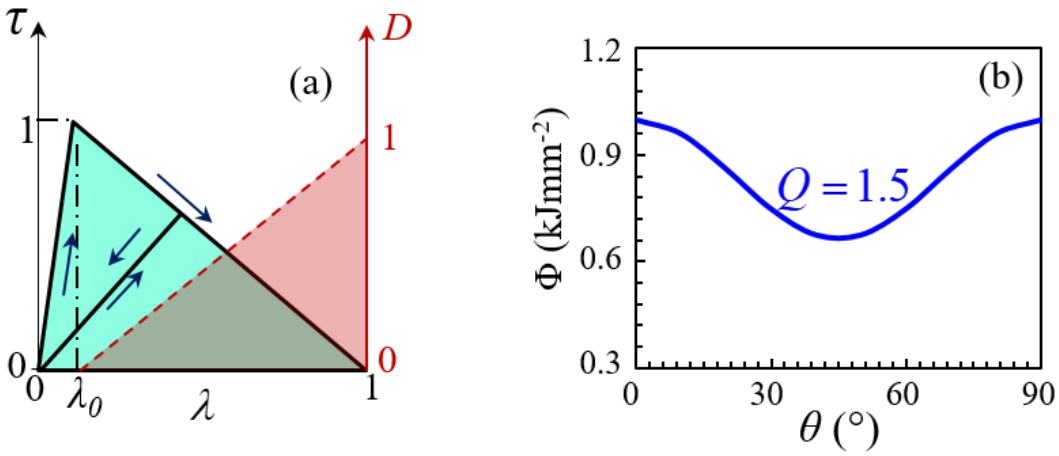

Figure 7.4: (a) normalized traction vs normalized separation for crack faces, (b) grain boundary fracture energy as a function of misorientation angles.

Table 7.2: Interfacial parameters for the 3D traction separation law

Q	K_{nn} (MPa)	K_{ss} (MPa)	K_{tt} (MPa)	$(\Phi_0)_{\max}$ (kJ/mm^2)	T_G (MPa)	$T_{GB}^{\min}$ (MPa)
1.5	500×10^6	500×10^6	500×10^6	1	962.5	641.67

7.2.3 Microstructure

Since we assume a generalized plane strain condition, the grain structure and their orientation distribution function are invariant in the Z direction and so is the misorientation distribution for the grain boundaries. Figure 7.5 shows two representative 2.5D microstructures with columnar grains. The microstructure in Figure 7.5(a) consists of randomly oriented grains, and the microstructure in Figure 7.5(b) constitutes of textured grains with two preferred texture components. As the thickness directions show, the microstructure and its orientation distribution does not change in that direction. Therefore, 2D slices of this columnar 3D microstructure represent the whole structure under the generalized plane strain assumption as shown in Figure 7.6. The 2D slices of these 3D columnar grain structures with 0%, 30%, 50%, 70%, and 100% textured grains (TG) are shown in Figure 7.7. In order to compare the results of 2.5D modeling with that of the previously described 2D, the orientation distribution functions and the grain structures are kept the same. The difference is that the slip is now not restricted to a single slip system and also we adopt a full 3D traction separation law for the interfaces.

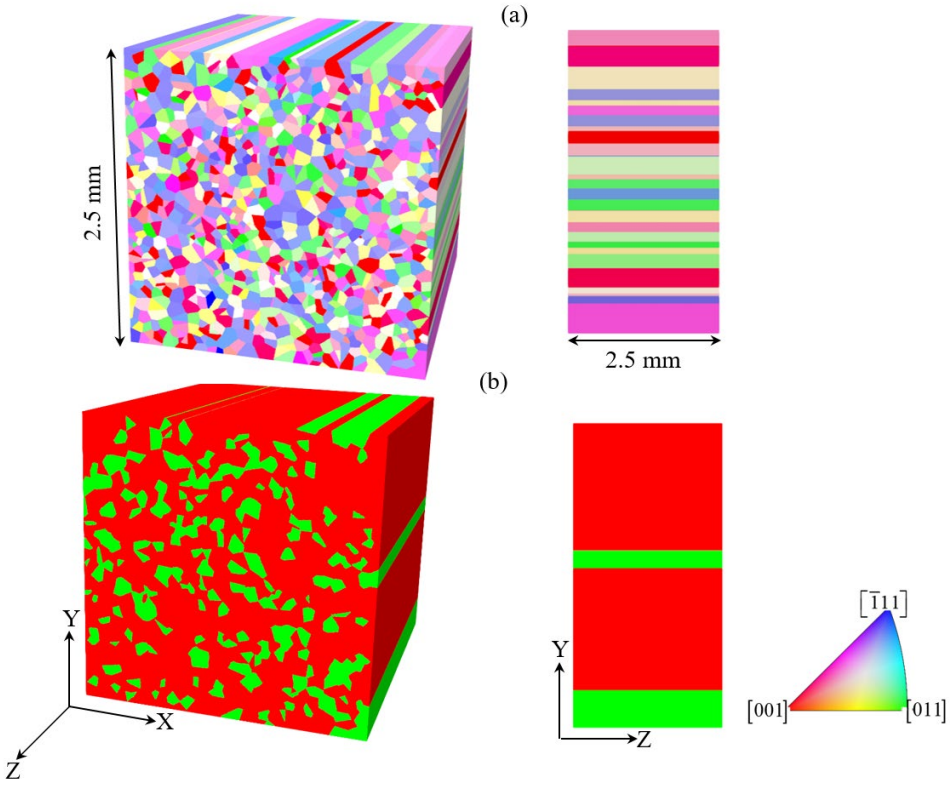

Figure 7.5: Instances of 2.5D microstructure with (a) 100% random grain orientations, (b) 100% textured grains.

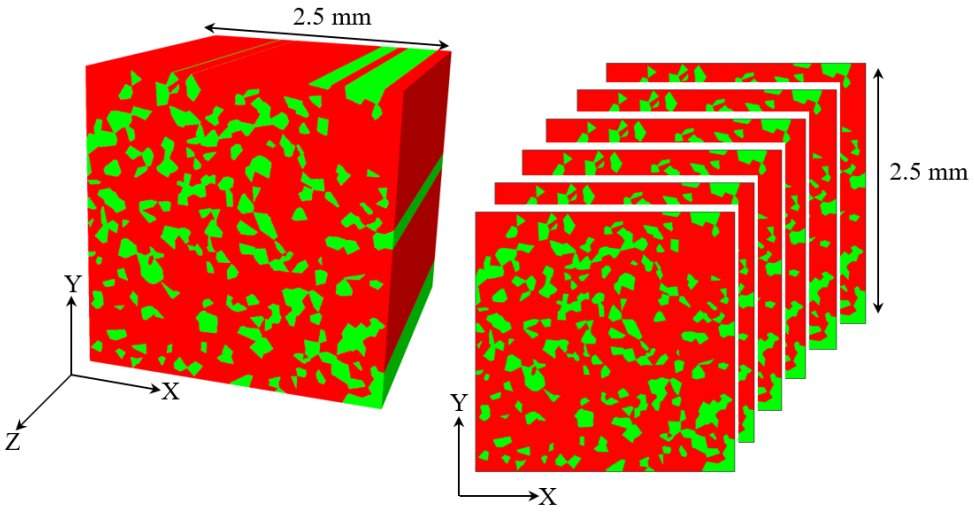

Figure 7.6: 2D slices obtained from a 2.5D microstructure.

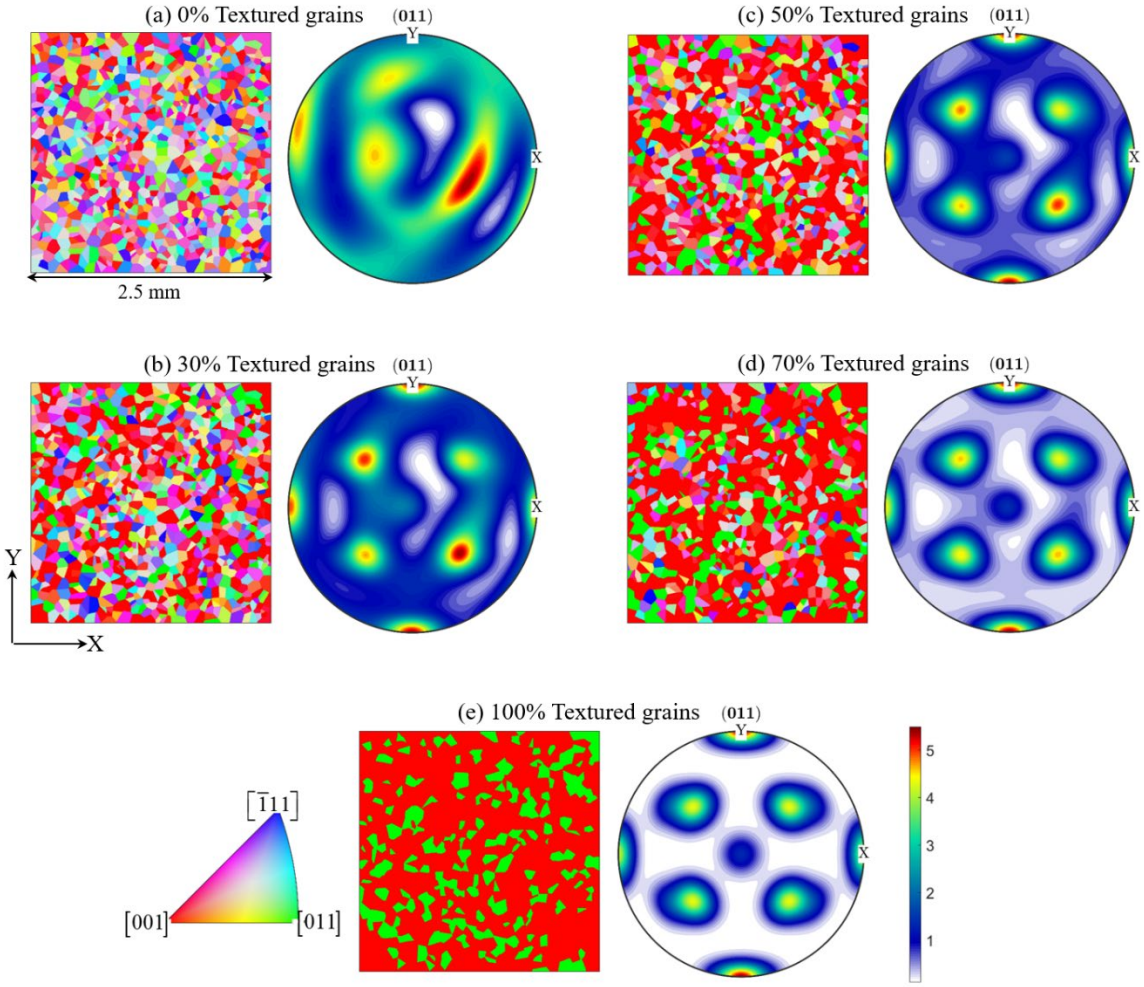

Figure 7.7: 2D slices from each of the five 2.5D microstructure sample with different proportions of textured grains and their corresponding (011) pole figures.

7.3 Comparison between 2D and 2.5D models

In this section results from the 2.5D simulations are compared with the 2D results in terms of the fracture toughness, crack growth resistance curves and fracture mechanisms.

7.3.1 Crack growth resistance curves

The same method of calculating *J*-integral along a crack tip contour through the homogenized region of the specimen is employed here to determine the crack growth resistance curves. Figure 7.6 compares the crack growth resistance curves obtained from this 2.5D formulation and the 2D formulation obtained before for three microstructures with 0%, 50%, and 100% textured grains (TG). For the case of the microstructure with randomly oriented grains, or 0% TG, the crack growth resistance curves obtained from 2.5D model and the 2D model fall close to each other. The 2D model underestimates the crack growth resistance both at crack initiation and when crack growth reaches the steady state. In case of the microstructure with 50% TG, the crack initiation resistance estimated from the 2.5D model is nearly equal to that estimated from the 2D model. However, the 2D model considerably underestimates the steady state crack growth resistance. In case of the microstructure with 100% TG, the 2D model underestimates the crack initiation resistance. In addition, the 2D model also underestimates the steady state crack growth resistance. The fact that the 2D model underestimates the fracture resistance can be attributed to the assumption of restricted slip in a single slip system. Figure 7.7 shows the fracture toughness values in terms of J_i, J_{IC}, K_i, and K_{IC} of five microstructures with 0%, 30%, 50%, 70%, and 100% of TG obtained from the 2.5D model and the 2D model. The effect of the fraction of TG on the crack initiation resistance follows similar trend in case of both the 2.5D and 2D model. The steady state fracture toughness values follow similar trend until the microstructure contains 100% of textured grains. In that case, the 2.5D model estimates a reduced fracture toughness compared to the microstructure with 70% textured grains.

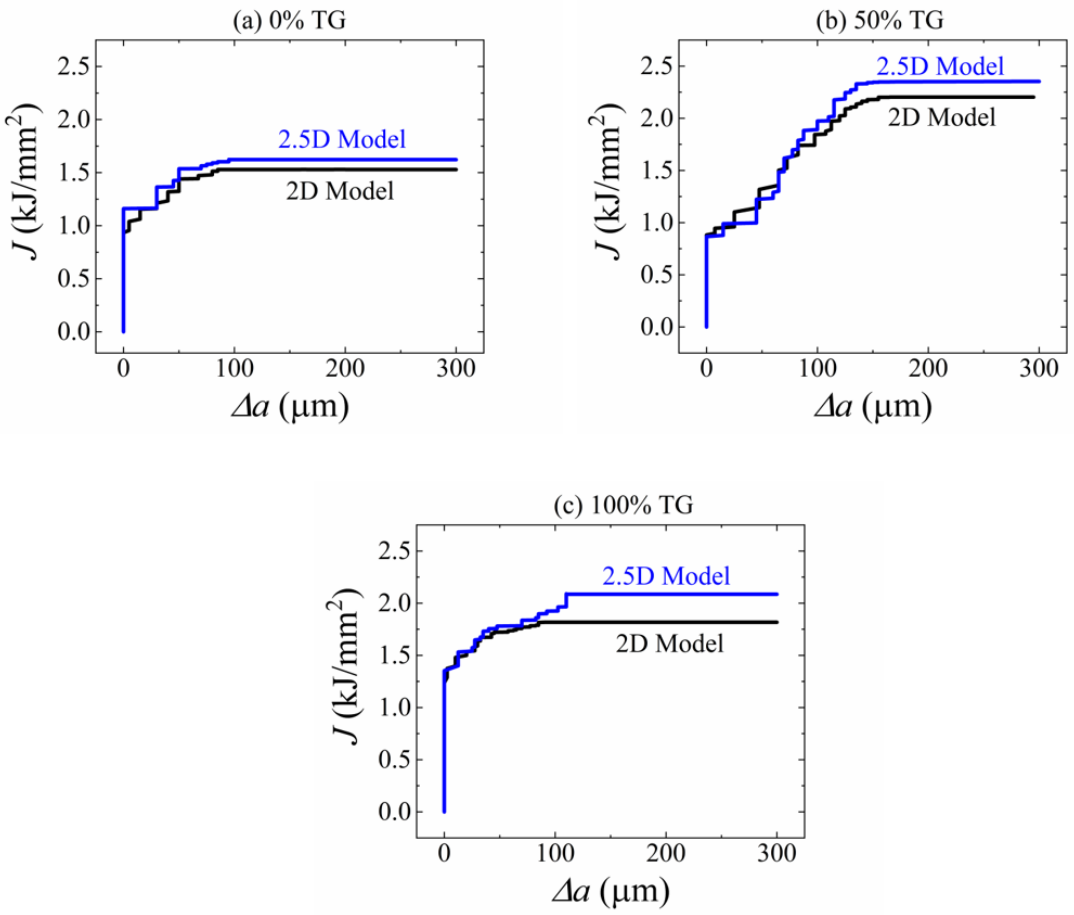

Figure 7.8: Crack growth resistance curves obtained from 2.5D and 2D models for microstructures with (a) 0%, (b) 50%, and (c) 100% textured grains (TG).

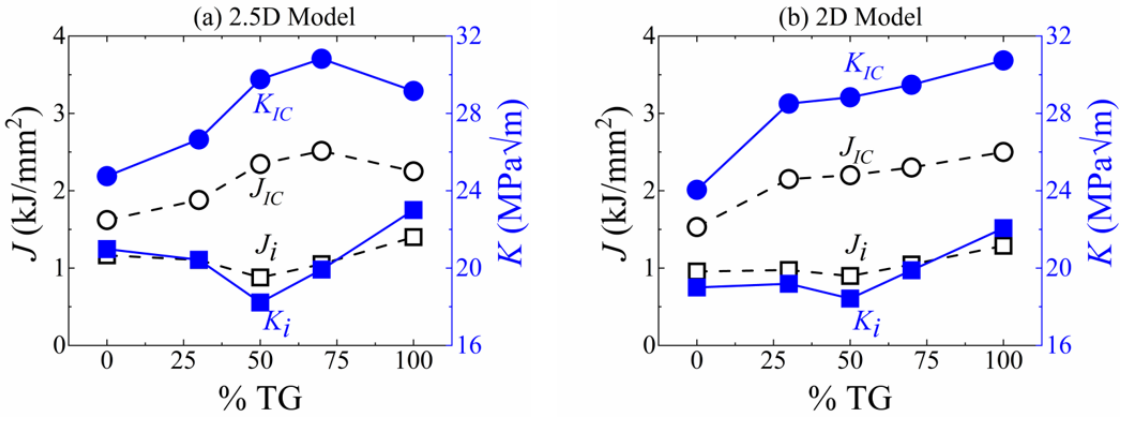

Figure 7.9: Variation of fracture toughness values measured in terms of J_i, J_{IC}, K_i, K_{IC} with fraction of textured grains in a microstructure using (a) 2.5D and (b) 2D models.

7.3.2 Crack propagation mechanisms

In order to understand the discrepancies in the results obtained from the 2.5D and 2D model, crack propagation paths are compared in Figure 7.8. The crack paths shown in three microstructures with 0%, 50%, and 100% TG obtained from the 2.5D model are quite similar to that obtained from the 2D model. In case of the microstructure with all randomly oriented grains, crack primarily grows along the grain boundaries. In case of the microstructure with 50% TG, both intergranular and transgranular mechanisms operate. Transgranular fracture dominates over intergranular crack propagation in case of the microstructure with 100% TG. The trends are reflected in the Figure 7.9. The crack path tortuosity monotonically decreases as the fraction of TG increases in the microstructure. The 2.5D and 2D models match well with each other in estimating the fracture mechanisms as functions of microstructure attributes.

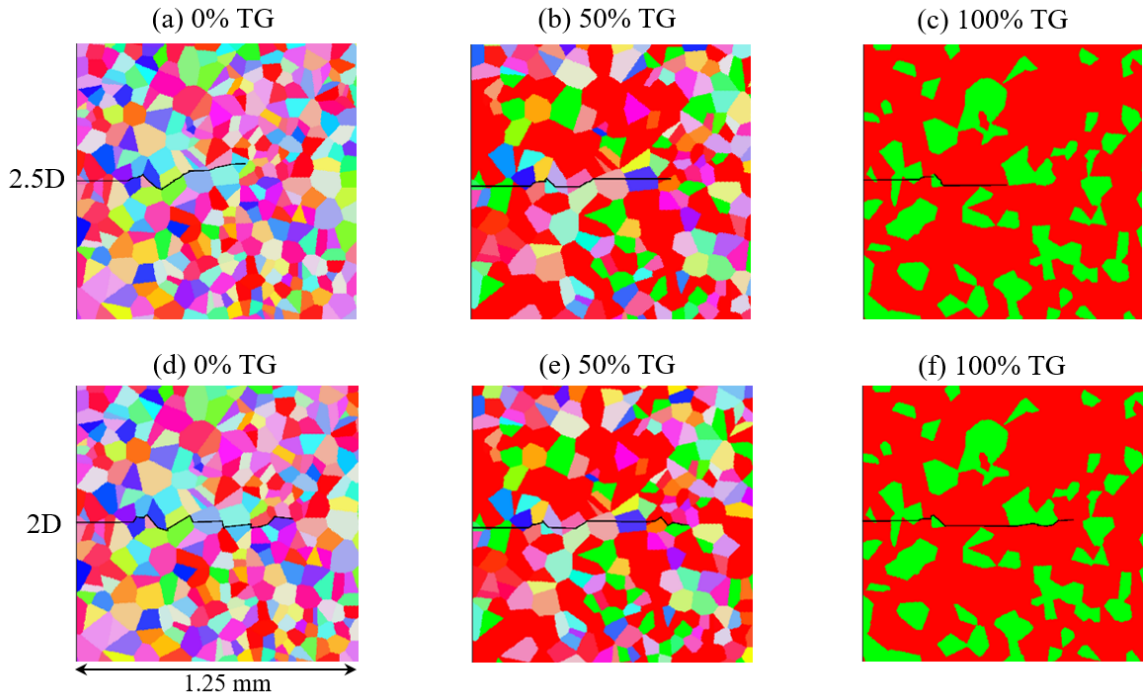

Figure 7.10: (a) – (c) crack paths in microstructures with 0%, 50%, and 100% textured grains estimated using 2.5D model; (d) – (f) crack paths obtained from the 2D model in the same microstructures.

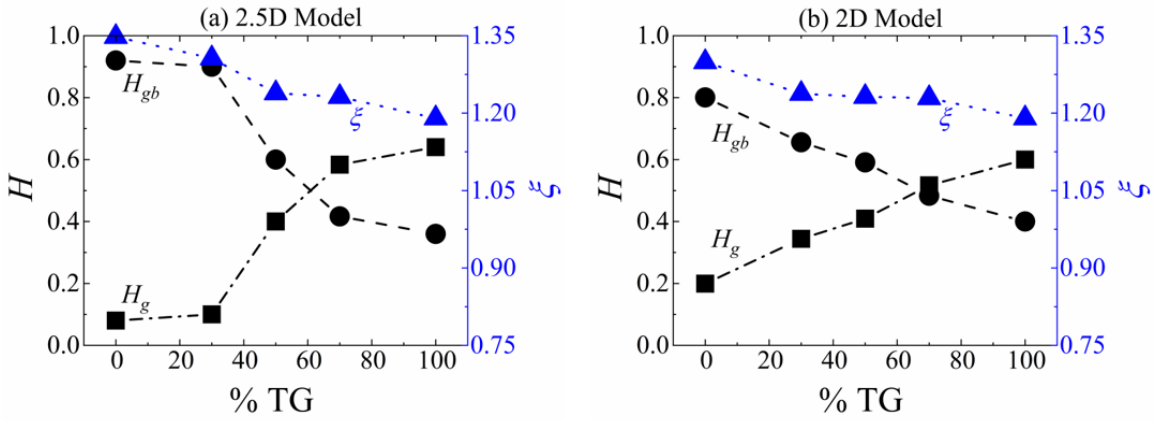

Figure 7.11: Crack path ratios and crack path tortuosity as a function of the fraction of textured grains estimated using (a) 2.5D model and (b) 2D model.

7.3.3 Plastic dissipation at the crack tip

Since the crack path estimated by the 2.5D model is similar to that estimated by the 2D model, the contribution of surface energy remains the same in both cases. This means that as expected, the 2D model underestimates the contribution of plastic dissipation. However, that does not explain why the 2D model overestimated the fracture toughness of the microstructure containing 100% TG. In order to reconcile the conflict, plastic strain associated with the crack tip is shown in the Figure 7.10. The figure shows that there is significant amount of plastic strain at the grain boundaries. This is an outcome of the 3D crystal plasticity formulation where multiple slip is activated, and plastic strain accumulates at the grain boundaries due to the incompatibility of slip system in the contacting grains. This results in finite amount of plastic dissipation associated with the intergranular cracking which is absent in the 2D model. In case of the 2D model, plastic dissipation is associated only with transgranular cracking. As a result, more transgranular

cracking leads to higher contribution of plastic dissipation that is finally manifested by an overall increases in the fracture toughness. The toughening mechanism of intergranular cracking is only due to the crack path tortuosity. Since no plastic dissipation is associated with the intergranular fracture, toughening effect of a tortuous crack path can never compensate the reduction in fracture toughness due to grain boundary cracking and match upto the toughening effect of transgranular fracture. However, in the 2.5D model, since intergranular fracture is also associated with a certain degree of plastic dissipation, the toughening effect of intergranular fracture is now two-fold, (1) due to crack path tortuosity, and (2) due to plastic dissipation. In case of the microstructure with 100% TG, intergranular crack path is nearly absent. Now, the microstructure with 70% TG manifests the highest value of fracture toughness. This is attributed to the co-play of intergranular and transgranular fracture mechanisms, both contributing to the toughening of the microstructure.

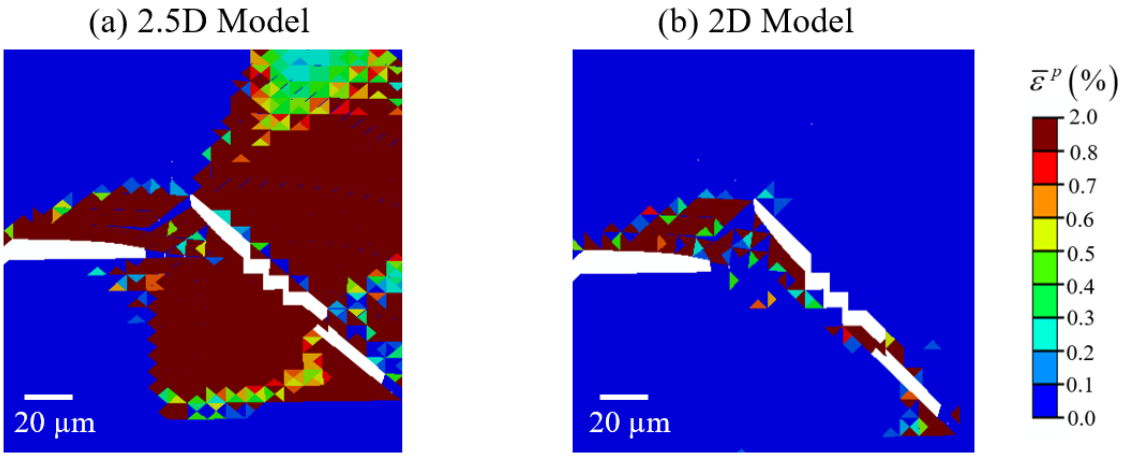

Figure 7.12: Plastic strain associated with intergranular cracking as evaluated by the (a) 2.5D model and (b) 2D model in the same instantiation of microstructure with 100% textured grains.

7.4 Summary

The 2.5D and 2D models yield similar results in terms of the crack propagation mechanisms and the crack initiation resistance. However, the 2D model tends to underestimate the contribution of plastic dissipation to fracture owing to the single slip assumption. The 2.5D model uses a 3D crystal plasticity formulation that allows simultaneous activation of multiple slip systems in the microstructure with columnar grains. This model reveals that plastic dissipation is not only associated with transgranular fracture, but also, plastic dissipation can be caused by intergranular fracture. This explains why the microstructure with 100% textured grains exhibit a lower fracture toughness compared to that with a microstructure with 70% textured grains and 30% of grains randomly oriented. This critical revelation says that an optimum proportion of intergranular and transgranular fracture needs to be achieved for maximized fracture resistance. Also, this section shows that in order to develop mathematical functions to model the trends between fracture and microstructure attributes, 2.5D models should be employed.

8 SUMMARY AND CONCLUSIONS

The entire work presented in this thesis addresses the primary concerns about structure property relations in terms of fracture behavior and microstructure attributes. The complete work can be classified into three basic segments. The first part describes the 2D computational framework and its capabilities. The second part uses this framework to study the effects of microstructure attributes on fracture toughness and fracture micromechanisms. The last part describes efficacy of the 2D framework and compares it with a 2.5D framework.

In this chapter, section 8.1 discusses the specific contributions of this work. Section 8.2 outlines the future scope of this work.

8.1 Significance of Contribution

As mentioned in the introduction, microstructure-sensitive modeling of fracture in polycrystalline ductile materials is still rare in the field of materials science. The understanding of overall fracture response as a function of the polycrystalline microstructure attributes is not completely comprehensible yet. In order to explore the fracture response as a function of microstructure, first a 2D multiscale computational framework is developed. The model uses a CT specimen under displacement controlled mode-I loading. A computationally generated microstructure enters the computational

framework around the crack tip of the CT specimen. Owing to the cohesive finite element method adopted in the microstructure region, crack path is explicitly resolved within the grains and along the grain boundaries. Fracture toughness is calculated in terms of the J-integral along a crack-tip contour through the homogenized section of the specimen. Owing to the CFEM framework the contributions of surface energy release rate and plastic dissipation are explicitly identified. Thus, the framework allows us to explicitly model the crack path, estimate the overall fracture toughness, and also capture competitions between intergranular and transgranular crack propagation, and also between plasticity and crack growth.

The model is then applied to bcc Mo. The material model parameters are calibrated to match the properties of Mo reported in the literature. The interfacial law is formulated to incorporate the misorientation angle dependent grain boundary behavior as observed in experiments. The overall computational scheme worked well in evaluating fracture behavior of Mo both in terms of the fracture toughness and the fracture mechanisms.

The effect of misorientation-sensitive grain boundary behavior on fracture is then characterized by systematically varying the grain boundary strength profiles in sets of randomly oriented grain structures. The overall fracture toughness decreases as the grain boundary fracture strength profiles become more skewed. The microstructure with a coarser grain size exhibits higher resistance to fracture owing to the availability of longer mean free path for transgranular fracture. Transgranular fracture is always associated with significant plastic dissipation for Mo with comparatively lower grain yield strength. Hence

transgranular fracture causes higher toughening effect in ductile metals. Even though intergranular fracture has the potential of toughening through crack path tortuosity, a trade off exists. Crack path tortuosity due to intergranular cracking cannot compensate for the loss of toughness owing to crack propagation through low energy brittle grain boundary sites.

Statistically equivalent multiple microstructure sample sets are used to characterize the stochasticity in fracture toughness values. The stochasticity increases with the increasing skewness in the grain boundary strength profiles. The fracture toughness and fracture micro-mechanisms obtained with different sets of microstructures facilitates development of mathematical relations that best describes the trends between fracture toughness and microstructure attributes. The mathematical expressions appreciate the multiscale nature of the problem and capture the competitive effects of surface energy, plastic dissipation; and transgranular, intergranular fracture. With more validation using realistic experiments these relations could be potentially used as material design tools.

In order to explore the effects of crystallographic texture, the 2D framework is extended to incorporate a 2D crystal plasticity formulation for modelling the anisotropic deformation of grains. Again, multiple statistically equivalent polycrystalline microstructure sets are generated with varying fractions of grains with a preferred orientation. Two primary bcc texture components are used in this study. The results enumerate that the overall fracture resistance increases as the microstructure contains more textured grains compared to a complete random grain structure. The amount of textured

grains modifies the grain size distribution, grain boundary misorientation distribution, and the density of favorably oriented primary slip systems. Therefore, by systematically varying the fraction of textured grains, the evolution of fracture toughness as functions of grain size distribution, weaker grain boundary density, and primary slip system density are established.

The fracture toughness increases with increasing skewness in the grain size distribution which is consistent with our earlier finding. Fracture toughness also increases as the density of weaker grain boundaries decreases and the density of favorably oriented primary slip systems increases. Reduction is weaker grain boundary density results in dominant transgranular crack propagation which in turn causes higher plastic dissipation. Higher density of favorably oriented slip systems also leads to higher degree of plastic dissipation and thus the overall fracture toughness increases. These trends are then quantified using mathematical equations. A microstructure descriptor is devised that incorporates the texture information in terms of grain size distribution, weaker grain boundary density, and primary slip system density. With proper validation of the computational results this microstructure descriptor can be potentially used for materials design purposes.

Finally, in order to understand the efficacy of 2D computations in modeling essentially 3D system, the capability of the model is extended to a 2.5D formulation. This computational framework uses 2D geometries with the assumption of generalized plane strain. The 2D microstructures in this framework essentially represents 3D microstructures

with columnar grains. A full 3D crystal plasticity model and 3D interfacial laws are adopted. The 3D crystal plasticity model allows activation of multiple slip systems and thus gets rid of the artificial hardening of grains in the 2D model imposed by restricted slip in a single slip system. This results in an important deviation from the 2D model. In the 2.5D model, intergranular fracture also causes plastic dissipation near the grain boundaries. As a result, intergranular fracture also acts as an effective toughening mechanism. Hence, the proportion of intergranular and transgranular fracture needs to be optimized for best material performance. The 2.5D and the 2D model yield similar trends in crack initiation resistance and fracture mechanisms as a function of the fraction of textured grains. Even though the entire work is based on bcc Mo, it yields important insights that can be further explored to develop materials design tools for any material in future.

8.2 Future scope of work

In addition to providing important insights, this work also identifies multitudes of possibilities of further research both in computational and experimental gamut of work. First and foremost a full 3D model should be developed. 3D microstructures should be generated by systematically varying the microstructure attributes. The results of the 3D models should be compared with the 2D, and 2.5D models so that a more computationally efficient modeling scheme can be identified to perform this kind of numerical exercises.

Series of experimentally obtained microstructures should be tested in order to validate the computational models with real experimental datasets. Obtaining

microstructures with systematically varying microstructure attributes is a challenge. The 3D printing techniques could be used to achieve that.

Once the more computationally efficient model is identified, and validated with significant volume of experimental datasets, the myriads of numerical experiments should be carried out with statistically equivalent microstructure sample sets. Further analyses of the results would facilitate develop mathematical models as it is done here. The mathematical models thus developed can be reliably used as materials design tools. The theory of machine learning can also find its application in this part of the work.

The above-mentioned exercises could be repeated for different materials systems. As the material changes, the crystal plasticity models would also have to be developed and modified accordingly. This opens up another gamut of future research. Also, the crystal plasticity models can be developed to directly account for dislocation density, void volume or void fraction etc..

Thus, the significance of this work not only lies in the ingenuity of the models developed or the valuable insights that they generate, but also in the fact that it has the potential to open up new directions for future study. The relevance remains in its potential to be used for any material systems in order to tailor microstructure for better performance.

REFERENCES

[1] A. Griffith, "The phenomenon of rupture and flow in solids. Phil, Trans, Roy. Soc. A221," 1920.

[2] K. Wieghardt, "Über das spalten und zerreißen elastischer körper," *Z. Mathematik und Physik,* vol. 55, no. 2, pp. 60-103, 1907.

[3] E. Orowan, "Fracture and strength of solids," *Reports on progress in physics,* vol. 12, no. 1, p. 185, 1949.

[4] G. Irwin, "Fracturing of metals," *ASM, Cleveland,* vol. 147, pp. 19-9, 1948.

[5] G. Irwin, "Fracture dynamics, Fracturing of Metals. American Society of Metals," ed: Cleveland, 1948.

[6] H. M. Westergaard, "Bearing pressures and cracks," *Trans AIME, J. Appl. Mech.,* vol. 6, pp. 49-53, 1939.

[7] M. Brossman and J. Kies, "Energy release rates during fracturing of perforated plates," Ship Structure Committee1955.

[8] J. Kies and H. Smith, "Toughness testing of hot-stretched acrylics," *Aircraft Industries Association and Air Development Command, Dayton OH,* 1955.

[9] G. R. Irwin, "Analysis of stresses and strains near the end of a crack transversing a plate," *Trans. ASME, Ser. E, J. Appl. Mech.,* vol. 24, pp. 361-364, 1957.

[10] D. S. Dugdale, "Yielding of steel sheets containing slits," *Journal of the Mechanics and Physics of Solids,* vol. 8, no. 2, pp. 100-104, 1960.

[11] G. I. Barenblatt, "The mathematical theory of equilibrium cracks in brittle fracture," in *Advances in applied mechanics*, vol. 7: Elsevier, 1962, pp. 55-129.

[12] A. A. Wells, "Unstable crack propagation in metals: cleavage and fast fracture," in *Proceedings of the crack propagation symposium*, 1961, vol. 1, no. 84.

[13] J. Hutchinson, "Plastic stress and strain fields at a crack tip," *Journal of the Mechanics and Physics of Solids,* vol. 16, no. 5, pp. 337-342, 1968.

[14] J. Hutchinson, "Singular behaviour at the end of a tensile crack in a hardening material," *Journal of the Mechanics and Physics of Solids,* vol. 16, no. 1, pp. 13-31, 1968.

[15] J. Rice and G. F. Rosengren, "Plane strain deformation near a crack tip in a power-law hardening material," *Journal of the Mechanics and Physics of Solids,* vol. 16, no. 1, pp. 1-12, 1968.

[16] J. R. Rice, "A path independent integral and the approximate analysis of strain concentration by notches and cracks," 1968.

[17] J. R. Rice, "Mathematical analysis in the mechanics of fracture," *Fracture: an advanced treatise,* vol. 2, pp. 191-311, 1968.

[18] G. B. Olson, "Computational Design of Hierarchically Structured Materials," *Science,* vol. 277, no. 5330, pp. 1237-1242, 1997.

[19] D. L. McDowell and G. B. Olson, "Concurrent design of hierarchical materials and structures," in *Scientific Modeling and Simulations*: Springer, 2008, pp. 207-240.

[20] D. T. Fullwood, S. R. Niezgoda, B. L. Adams, and S. R. Kalidindi, "Microstructure sensitive design for performance optimization," *Progress in Materials Science,* vol. 55, no. 6, pp. 477-562, 2010/08/01/ 2010.

[21] R. Liu, A. Kumar, Z. Chen, A. Agrawal, V. Sundararaghavan, and A. Choudhary, "A predictive machine learning approach for microstructure optimization and materials design," *Scientific Reports,* Article vol. 5, p. 11551, 06/23/online 2015.

[22] Y. Li and M. Zhou, "Prediction of fracture toughness of ceramic composites as function of microstructure: I. Numerical simulations," *Journal of the Mechanics and Physics of Solids,* vol. 61, no. 2, pp. 472-488, 2013/02/01/ 2013.

[23] Y. Li and M. Zhou, "Prediction of fracturess toughness of ceramic composites as function of microstructure: II. analytical model," *Journal of the Mechanics and Physics of Solids,* vol. 61, no. 2, pp. 489-503, 2013/02/01/ 2013.

[24] M. Hossain, C.-J. Hsueh, B. Bourdin, and K. Bhattacharya, "Effective toughness of heterogeneous media," *Journal of the Mechanics and Physics of Solids,* vol. 71, pp. 15-32, 2014.

[25] M. Ebrahimi, D. Balint, A. Sutton, and D. Dini, "A discrete crack dynamics model of toughening in brittle polycrystalline material by crack deflection," *Engineering Fracture Mechanics,* 2019.

[26] C. Prakash, H. Lee, M. Alucozai, and V. Tomar, "An analysis of the influence of grain boundary strength on microstructure dependent fracture in polycrystalline tungsten," *International Journal of Fracture,* vol. 199, no. 1, pp. 1-20, 2016.

[27] H. Chen, Y. Jiao, and Y. Liu, "Investigating the microstructural effect on elastic and fracture behavior of polycrystals using a nonlocal lattice particle model," *Materials Science and Engineering: A,* vol. 631, pp. 173-180, 2015/04/17/ 2015.

[28] Y. Li, D. McDowell, and M. Zhou, "A multiscale framework for predicting fracture toughness of polycrystalline metals," *Materials Performance and Characterization,* vol. 3, no. 3, pp. 157-172, 2014.

[29] A. Srivastava, S. Osovski, and A. Needleman, "Engineering the crack path by controlling the microstructure," *Journal of the Mechanics and Physics of Solids,* vol. 100, pp. 1-20, 2017.

[30] Y. Li and M. Zhou, "Effect of Competing Mechanisms on Fracture Toughness of Metals with Ductile Grain Structures," *Engineering Fracture Mechanics,* 2018.

[31] S. Osovski, A. Needleman, and A. Srivastava, "Intergranular fracture prediction and microstructure design," *International Journal of Fracture,* pp. 1-14, 2019.

[32] R. J. Asaro, "Micromechanics of Crystals and Polycrystals," in *Advances in Applied Mechanics*, vol. 23, J. W. Hutchinson and T. Y. Wu, Eds.: Elsevier, 1983, pp. 1-115.

[33] D. Peirce, R. J. Asaro, and A. Needleman, "Material rate dependence and localized deformation in crystalline solids," *Acta Metallurgica,* vol. 31, no. 12, pp. 1951-1976, 1983/12/01/ 1983.

[34] R. J. Asaro and A. Needleman, "Flow localization in strain hardening crystalline solids," *Scripta Metallurgica,* vol. 18, no. 5, pp. 429-435, 1984/05/01/ 1984.

[35] H. Deve and R. Asaro, "The development of plastic failure modes in crystalline materials: shear bands in FCC polycrystals," *Metallurgical Transactions A,* vol. 20, no. 4, pp. 579-593, 1989.

[36] P. E. McHugh, A. G. Varias, R. J. Asaro, and C. F. Shih, "Computational modeling of microstructures," *Future Generation Computer Systems,* vol. 5, no. 2, pp. 295-318, 1989/09/01/ 1989.

[37] T. L. Sham and A. Needleman, "Effects of triaxial stressing on creep cavitation of grain boundaries," *Acta Metallurgica,* vol. 31, no. 6, pp. 919-926, 1983/06/01/ 1983.

[38] T. Christman, A. Needleman, S. Nutt, and S. Suresh, "On microstructural evolution and micromechanical modelling of deformation of a whisker-reinforced metal-matrix composite," *Materials Science and Engineering: A,* vol. 107, pp. 49-61, 1989/01/01/ 1989.

[39] A. Needleman, "Micromechanical modelling of interfacial decohesion," *Ultramicroscopy,* vol. 40, no. 3, pp. 203-214, 1992.

[40] G. L. Povirk, S. R. Nutt, and A. Needleman, "Analysis of creep in thermally cycled Al/SiC composites," *Scripta Metallurgica et Materialia,* vol. 26, no. 3, pp. 461-466, 1992/02/01/ 1992.

[41] A. Needleman, "Size effects in the analysis of ductility under dynamic loading conditions," *ASME APPLIED MECHANICS DIVISION-PUBLICATIONS-AMD,* vol. 180, pp. 55-55, 1993.

[42] X.-P. Xu and A. Needleman, "Numerical simulations of fast crack growth in brittle solids," *Journal of the Mechanics and Physics of Solids,* vol. 42, no. 9, pp. 1397-1434, 1994.

[43] X.-P. Xu and A. Needleman, "Numerical simulations of dynamic crack growth along an interface," *International Journal of Fracture,* journal article vol. 74, no. 4, pp. 289-324, December 01 1996.

[44] V. Tvergaard and A. Needleman, "Three dimensional microstructural effects on plane strain ductile crack growth," *International journal of solids and structures,* vol. 43, no. 20, pp. 6165-6179, 2006.

[45] Y. Liu, X. Zheng, S. Osovski, and A. Srivastava, "On the micromechanism of inclusion driven ductile fracture and its implications on fracture toughness," *Journal of the Mechanics and Physics of Solids,* vol. 130, pp. 21-34, 2019.

[46] A. Srivastava, L. Ponson, S. Osovski, E. Bouchaud, V. Tvergaard, and A. Needleman, "Effect of inclusion density on ductile fracture toughness and roughness," *Journal of the Mechanics and Physics of Solids,* vol. 63, pp. 62-79, 2014.

[47] A. L. Gurson, "Continuum Theory of Ductile Rupture by Void Nucleation and Growth: Part I—Yield Criteria and Flow Rules for Porous Ductile Media," *Journal of Engineering Materials and Technology,* vol. 99, no. 1, pp. 2-15, 1977.

[48] T. Pardoen and J. Hutchinson, "An extended model for void growth and coalescence," *Journal of the Mechanics and Physics of Solids,* vol. 48, no. 12, pp. 2467-2512, 2000.

[49] X. Guo, K. Chang, L. Chen, and M. Zhou, "Determination of fracture toughness of AZ31 Mg alloy using the cohesive finite element method," *Engineering Fracture Mechanics,* vol. 96, pp. 401-415, 2012.

[50] S. Osovski, A. Srivastava, J. Williams, and A. Needleman, "Grain boundary crack growth in metastable titanium β alloys," *Acta Materialia,* vol. 82, pp. 167-178, 2015.

[51] A. Molkeri, A. Srivastava, S. Osovski, and A. Needleman, "Influence of Grain Size Distribution on Ductile Intergranular Crack Growth Resistance," *Journal of Applied Mechanics,* pp. 1-11, 2019.

[52] A. Musienko, A. Tatschl, K. Schmidegg, O. Kolednik, R. Pippan, and G. Cailletaud, "Three-dimensional finite element simulation of a polycrystalline copper specimen," *Acta materialia,* vol. 55, no. 12, pp. 4121-4136, 2007.

[53] M. A. Zikry and M. Kao, "Large-scale crystal plasticity computations of microstructural failure modes," *Computing Systems in Engineering,* vol. 6, no. 3, pp. 225-240, 1995/06/01/ 1995.

[54] M. A. Zikry and M. Kao, "Inelastic microstructural failure mechanisms in crystalline materials with high angle grain boundaries," *Journal of the Mechanics and Physics of Solids,* vol. 44, no. 11, pp. 1765-1798, 1996/11/01/ 1996.

[55] M. A. Zikry and T. Kameda, "Inelastic three dimensional high strain-rate dislocation density based analysis of grain-boundary effects and failure modes in ordered intermetallics," *Mechanics of Materials,* vol. 28, no. 1, pp. 93-102, 1998/07/01/ 1998.

[56] M. Zikry, "Failure modes in cubic crystalline materials," *ASME-PUBLICATIONS-AD,* vol. 36, pp. 199-199, 1992.

[57] K. Sreeramulu, P. Sharma, R. Narasimhan, and R. K. Mishra, "Numerical simulations of crack tip fields in polycrystalline plastic solids," *Engineering Fracture Mechanics,* vol. 77, no. 8, pp. 1253-1274, 2010/05/01/ 2010.

[58] N. Kowalski, L. Delannay, P. Yan, and J.-F. Remacle, "Finite element modeling of periodic polycrystalline aggregates with intergranular cracks," *International Journal of Solids and Structures,* vol. 90, pp. 60-68, 2016/07/01/ 2016.

[59] D. Wilson, Z. Zheng, and F. P. E. Dunne, "A microstructure-sensitive driving force for crack growth," *Journal of the Mechanics and Physics of Solids,* vol. 121, pp. 147-174, 2018/12/01/ 2018.

[60] I. Simonovski and L. Cizelj, "Cohesive zone modeling of intergranular cracking in polycrystalline aggregates," *Nuclear Engineering and Design,* vol. 283, pp. 139-147, 2015/03/01/ 2015.

[61] J. D. Clayton and J. Knap, "Phase field modeling and simulation of coupled fracture and twinning in single crystals and polycrystals," *Computer Methods in Applied Mechanics and Engineering,* vol. 312, pp. 447-467, 2016/12/01/ 2016.

[62] D. M. Bond and M. A. Zikry, "Differentiating between intergranular and transgranular fracture in polycrystalline aggregates," *Journal of Materials Science,* vol. 53, no. 8, pp. 5786-5798, 2018/04/01 2018.

[63] L. Lim and T. Watanabe, "Grain boundary character distribution controlled toughness of polycrystals—A two-dimensional model," *Scripta Metallurgica,* vol. 23, no. 4, pp. 489-494, 1989.

[64] L. Lim and T. Watanabe, "Fracture toughness and brittle-ductile transition controlled by grain boundary character distribution (GBCD) in polycrystals," *Acta metallurgica et materialia,* vol. 38, no. 12, pp. 2507-2516, 1990.

[65] T. Watanabe, "Grain boundary design and control for high temperature materials," *Materials Science and Engineering: A,* vol. 166, no. 1-2, pp. 11-28, 1993.

[66] T. Watanabe, "The impact of grain boundary character distribution on fracture in polycrystals," *Materials Science and Engineering: A,* vol. 176, no. 1-2, pp. 39-49, 1994.

[67] T. Watanabe and S. Tsurekawa, "The control of brittleness and development of desirable mechanical properties in polycrystalline systems by grain boundary engineering," *Acta materialia,* vol. 47, no. 15-16, pp. 4171-4185, 1999.

[68] S. Kobayashi, T. Inomata, H. Kobayashi, S. Tsurekawa, and T. Watanabe, "Effects of grain boundary-and triple junction-character on intergranular fatigue crack nucleation in polycrystalline aluminum," *Journal of Materials Science,* vol. 43, no. 11, pp. 3792-3799, 2008.

[69] T. Watanabe, "Grain boundary engineering: historical perspective and future prospects," *Journal of materials science,* vol. 46, no. 12, pp. 4095-4115, 2011.

[70] H. Kokawa, T. Watanabe, and S. Karashima, "Structural changes during sliding of aluminium grain boundaries with different initial structures," *Scripta metallurgica,* vol. 17, no. 10, pp. 1155-1159, 1983.

[71] I. Bantounas, D. Dye, and T. C. Lindley, "The effect of grain orientation on fracture morphology during high-cycle fatigue of Ti–6Al–4V," *Acta materialia,* vol. 57, no. 12, pp. 3584-3595, 2009.

[72] I. Bantounas, D. Dye, and T. C. Lindley, "The role of microtexture on the faceted fracture morphology in Ti–6Al–4V subjected to high-cycle fatigue," *Acta materialia,* vol. 58, no. 11, pp. 3908-3918, 2010.

[73] M. A. Arafin and J. A. Szpunar, "Modeling of grain boundary character reconstruction and predicting intergranular fracture susceptibility of textured and random polycrystalline materials," *Computational Materials Science,* vol. 50, no. 2, pp. 656-665, 2010/12/01/ 2010.

[74] D. Bachurin, "Influence of grain boundary misorientation on intergranular fracture of nanocrystalline palladium," *International Journal of Fracture,* vol. 214, no. 1, pp. 69-78, 2018.

[75] G. Nolze and R. Hielscher, "IPF coloring of crystal orientation data," *Preprint Technische Universität Chemnitz,* 2016.

[76] D. Sturm, M. Heilmaier, J. H. Schneibel, P. Jéhanno, B. Skrotzki, and H. Saage, "The influence of silicon on the strength and fracture toughness of molybdenum," *Materials Science and Engineering: A,* vol. 463, no. 1-2, pp. 107-114, 2007.

[77] P. Welch and G. Davies, "Texture and cleavage in molybdenum," *Texture, Stress, and Microstructure,* vol. 6, no. 1, pp. 21-37, 1983.

[78] C.-G. Oertel *et al.*, "Influence of cross rolling and heat treatment on texture and forming properties of molybdenum sheets," *International Journal of Refractory Metals and Hard Materials,* vol. 28, no. 6, pp. 722-727, 2010.

[79] C. Chen, S. Wang, Y. Jia, M. Wang, Z. Li, and Z. Wang, "The orientation dependence of hot deformation behaviors of Mo with elongated grains," *International Journal of Refractory Metals and Hard Materials,* vol. 41, pp. 603-608, 2013.

[80] C. Chen, S. Wang, Y. Jia, M. Wang, Z. Li, and Z. Wang, "The effect of texture and microstructure on the properties of Mo bars," *Materials Science and Engineering: A,* vol. 601, pp. 131-138, 2014.

[81] S. Primig, H. Clemens, W. Knabl, A. Lorich, and R. Stickler, "Orientation dependent recovery and recrystallization behavior of hot-rolled molybdenum," *International Journal of Refractory Metals and Hard Materials,* vol. 48, pp. 179-186, 2015.

[82] M. Lobanov, S. Danilov, V. Pastukhov, S. Averin, Y. Khrunyk, and A. Popov, "The crystallographic relationship of molybdenum textures after hot rolling and recrystallization," *Materials & Design,* vol. 109, pp. 251-255, 2016.

[83] X.-P. Xu and A. Needleman, "Numerical simulations of dynamic interfacial crack growth allowing for crack growth away from the bond line," *International Journal of Fracture,* vol. 74, no. 3, pp. 253-275, 1996.

[84] V. Tomar, J. Zhai, and M. Zhou, "Bounds for element size in a variable stiffness cohesive finite element model," *International journal for numerical methods in engineering,* vol. 61, no. 11, pp. 1894-1920, 2004.

[85] J. Zhai, V. Tomar, and M. Zhou, "Micromechanical simulation of dynamic fracture using the cohesive finite element method," *Journal of engineering materials and technology,* vol. 126, no. 2, pp. 179-191, 2004.

[86] A. Standard, "Standard test method for measurement of fracture toughness," *ASTM, E1820-01,* pp. 1-46, 2001.

[87] P. Sisodia and M. Verma, "Polycrystalline elastic moduli of some hexagonal and tetragonal materials," *physica status solidi (a),* vol. 122, no. 2, pp. 525-534, 1990.

[88] F. H. Featherston and J. Neighbours, "Elastic constants of tantalum, tungsten, and molybdenum," *Physical Review,* vol. 130, no. 4, p. 1324, 1963.

[89] M. Kuna and D. Sun, "Three-dimensional cell model analyses of void growth in ductile materials," *International Journal of Fracture,* vol. 81, no. 3, pp. 235-258, 1996.

[90] G. I. Taylor, "Plastic strain in metals.," (in English), *Journal of the Institute of Metals,* vol. 62, pp. 307-324, 1938.

[91] R. Hill and J. R. Rice, "Constitutive analysis of elastic-plastic crystals at arbitrary strain," *Journal of the Mechanics and Physics of Solids,* vol. 20, no. 6, pp. 401-413, 1972.

[92] R. J. Asaro and J. R. Rice, "Strain Localization in Ductile Single-Crystals," (in English), *Journal of the Mechanics and Physics of Solids,* vol. 25, no. 5, pp. 309-338, 1977.

[93] D. Peirce, R. J. Asaro, and A. Needleman, "An Analysis of Nonuniform and Localized Deformation in Ductile Single-Crystals," (in English), *Acta Metallurgica,* vol. 30, no. 6, pp. 1087-1119, 1982.

[94] R. D. McGinty and D. L. McDowell, "Application of multiscale crystal plasticity models to forming limit diagrams," (in English), *Journal of Engineering Materials and Technology-Transactions of the Asme,* vol. 126, no. 3, pp. 285-291, Jul 2004.

[95] C. P. Przybyla and D. L. McDowell, "Simulated microstructure-sensitive extreme value probabilities for high cycle fatigue of duplex Ti-6Al-4V," (in English), *International Journal of Plasticity,* vol. 27, no. 12, pp. 1871-1895, Dec 2011.

[96] J.-Y. Kim and J. R. Greer, "Size-dependent mechanical properties of molybdenum nanopillars," *Applied Physics Letters,* vol. 93, no. 10, p. 101916, 2008.

[97] R. Gröger and V. Vitek, "Temperature and strain rate dependent flow criterion for bcc transition metals based on atomistic analysis of dislocation glide," *International Journal of Materials Research,* vol. 100, no. 3, pp. 315-321, 2009.

[98] J.-Y. Kim, D. Jang, and J. R. Greer, "Tensile and compressive behavior of tungsten, molybdenum, tantalum and niobium at the nanoscale," *Acta Materialia,* vol. 58, no. 7, pp. 2355-2363, 2010.

[99] J.-Y. Kim, D. Jang, and J. R. Greer, "Crystallographic orientation and size dependence of tension–compression asymmetry in molybdenum nano-pillars," *International Journal of Plasticity,* vol. 28, no. 1, pp. 46-52, 2012.

[100] J. R. Rice, "A path independent integral and the approximate analysis of strain concentration by notches and cracks," *Journal of applied mechanics,* vol. 35, no. 2, pp. 379-386, 1968.

[101] J. Rice, P. Paris, and J. Merkle, "Some further results of J-integral analysis and estimates," in *Progress in flaw growth and fracture toughness testing*: ASTM International, 1973.

[102] A. Ahadi and Q. Sun, "Grain size dependence of fracture toughness and crack-growth resistance of superelastic NiTi," *Scripta Materialia,* vol. 113, pp. 171-175, 2016/03/01/ 2016.

[103] Z. Fan, "The grain size dependence of ductile fracture toughness of polycrystalline metals and alloys," *Materials Science and Engineering: A,* vol. 191, no. 1, pp. 73-83, 1995/02/01/ 1995.

[104] M. De Campos, L. R. Lopes, P. Magina, F. L. Tavares, C. Kunioshi, and H. Goldenstein, "Texture and microtexture studies in different types of cast irons," *Materials Science and Engineering: A,* vol. 398, no. 1-2, pp. 164-170, 2005.